ISTANBUL TECHNICAL UNIVERSITY ★ GRADUATE SCHOOL

EXPERIMENTAL STUDY ON INTERACTION OF UNSTEADY FLOW WITH BRIDGE PIERS WITH DIFFERENT CROSS SECTIONS

Ph.D. THESIS

Mehrnoush KOHANDEL GARGARI

Department of Civil Engineering

Hydraulics and Water Resources Engineering Programme

SEPTEMBER 2021

ISTANBUL TECHNICAL UNIVERSITY ★ GRADUATE SCHOOL

EXPERIMENTAL STUDY ON INTERACTION OF UNSTEADY FLOW WITH BRIDGE PIERS WITH DIFFERENT CROSS SECTIONS

Ph.D. THESIS

Mehrnoush KOHANDEL GARGARI

(501152502)

Department of Civil Engineering

Hydraulics and Water Resources Engineering Programme

Thesis Advisor: Assoc. Prof. Dr. Veysel Sadan Ozgur KIRCA

SEPTEMBER 2021

İSTANBUL TEKNİK ÜNİVERSİTESİ ★ LİSANSÜSTÜ EĞİTİM ENSTİTÜSÜ

FARKLI ENKESİT ŞEKLİNE SAHİP KÖPRÜ AYAKLARININ DEĞİŞKEN AKIM KOŞULLARIYLA ETKİLEŞİMLERİNİN İNCELENMESİ

DOKTORA TEZİ

Mehrnoush KOHANDEL GARGARI
(501152502)

İnşaat Mühendisliği Anabilim Dalı

Hidrolik ve Su Kaynakları Mühendisliği Programı

Tez Danışmanı: Doç. Dr. Veysel Şadan Özgür KIRCA

EYLÜL 2021

Mehrnoush KOHANDEL GARGARI, a Ph.D. student of İTU Graduate School student ID 501152502, successfully defended the thesis entitled "EXPERIMENTAL STUDY ON INTERACTION OF UNSTEADY FLOW WITH BRIDGE PIERS WITH DIFFERENT CROSS SECTIONS", which she prepared after fulfilling the requirements specified in the associated legislations, before the jury whose signatures are below.

Thesis Advisor :	**Assoc. Prof. Dr. Veysel Şadan Özgür KIRCA** Istanbul Technical University	.....
Jury Members :	**Assoc. Prof. Dr. Oral YAĞCI** Istanbul Technical University	.....
	Assoc. Prof. Dr. Ahmet Ozan ÇELİK Eskisehir Technical University	.....
	Prof. Dr. Serdar BEJİ Istanbul Technical University	.....
	Asst. Prof. Dr. Cihan ŞAHİN Yıldız Technical University	.....

Date of Submission : 19 August 2021
Date of Defense : 16 September 2021

To my family,

FOREWORD

This research project was carried out at Istanbul Technical University's Hydraulic Laboratory under the supervision of Assoc.Prof. V. Özgür KIRCA. I'd like to express my appreciation for his constant support throughout the experiments and thesis writing. He always gave of his time and energy whenever I had a problem, and he was always available and willing to help.

I would also like to acknowledge the help I got from Assoc.Prof. Oral YAĞCI during the project. His unconditional help and practical suggestions cannot be overestimated.

I'd also like to thank my friends Umut Dolaman and Eryilmaz Erdog for their collaboration, as we worked together and shared the project's difficulties.

Last but not least I would like to express my profound gratitude to my family, I am very lucky for owning their unfailing support and continuous encouragement during my life and my study years. This accomplishment would not have been finished without them.

I also appreciate the contribution of the Scientific and Technological Research Council of Turkey (TUBITAK) for providing fellowship during my Ph.D. and financial support of this thesis under project 117M969 under the coordination of Assoc.Prof.V.Ş. Özgür KIRCA and Assoc.Prof. Oral YAĞCI.

SEPTEMBER 2021 Mehrnoush KOHANDEL GARGARI

(Civil Engineer)

TABLE OF CONTENTS

Page

ABBREVIATIONS

LES	**:** Large eddy simulation
SPH	**:** Smoothed-particles hydrodynamics
URANS	**:** Unsteady Reynolds Averaged Navier-Stokes
PIV	**:** Particle Image Velocimetry
ADV	**:** Acoustic Doppler Velocimeter
WL1, WL2	**:** water level probes in the upstream and downstream the pile
K	**:** Turbulent Kinetic energy

SYMBOLS

$\mathbf{A}$	: wetted cross section area
$\mathbf{L}$	: Length of cylinder
$\mathbf{D}$	: Cylinder Diameter
$\mathbf{Re}$	: Reynolds number
$\boldsymbol{\nu}$	: Kinematic viscosity
$\mathbf{t}$	: Time
$\mathbf{u(t), v(t), z(t):}$	Time dependent Reynolds averaged velocities in x, y and z directions
$\mathbf{St}$.	: Strouhal number
$\mathbf{f_v}$	: Shedding frequency of the vortices
$\mathbf{g}$	: Gravity acceleration
$\mathbf{h}$	: Water depth
ρ	: Density
$\mathbf{S_f}$	: Energy grade line slope
$\boldsymbol{\beta}$	: Correction factor related to the cross-sectional time averaged velocity
$\boldsymbol{\Gamma, \Lambda, \Upsilon}$	: Unsteadiness coefficient
$\boldsymbol{\Delta D}$	: Difference between base-flow and maximum depth
$\boldsymbol{\Delta T}$	: Total time duration of the hydrograph
$\boldsymbol{\Delta Q}$	: Difference of maximum and minimum discharge
$\mathbf{u_b^*}$	: Friction velocity of the base-flow
$\boldsymbol{\delta}$	: Boundary layer thickness
$\mathbf{KC_u}$	: Keulegan-Carpenter number
$\mathbf{S}$	: Steady flow
$\mathbf{U}$	: Unsteady flow
$\mathbf{V_{max}}$, $\mathbf{V_{min}}$	: Maximum and minimum velocities of the hydrograph
$\mathbf{Q_{max}}$, $\mathbf{Q_{min}}$	: Maximum and minimum discharge of the hydrograph
$\mathbf{u', v', w'}$	: Fluctuating velocities components
$\mathbf{J}$	: Hydraulic gradient
$\mathbf{z}$	: Distance from the bed
$\mathbf{u_{rms}}$	: Turbulent quantities

$\mathbf{U_f}$: shear velocity

$\boldsymbol{\kappa}$: Van-Karman constant

$\boldsymbol{\tau_b}$: Bed shear stress

$\mathbf{y^+}$: Normalised depth

LIST OF TABLES

Page

LIST OF FIGURES

Page

EXPERIMENTAL STUDY ON INTERACTION OF UNSTEADY FLOW WITH BRIDGE PIERS WITH DIFFERENT CROSS SECTIONS

SUMMARY

The problem of interaction between a vertical cylindrical structure (such as a bridge pier or pile) and a gradually varying unsteady flow is addressed in this study. In practice not only circular cylinders, but also various hydraulically streamlined cross-sections are used in bridge piers. The flow structure around these obstacles are significantly altered which leads changes in bed shear stress and amount/geometry of scour that takes place around the bridge pier. In this thesis, the flow-pile interactions under the unsteady flow are investigated, and as such, the similarities and differences in comparison to the case of steady flow are determined. The spatial variations of Reynolds averaged velocity and turbulence characteristics around the cylindrical structures are determined as a useful tool to help us understand how the flow patterns in the wake of the cylinders reacts with change in the cross-sections both in unsteady and steady flows.

Although many studies in the literature have dealt with the flow around similar structures, most of these studies are limited to circular cross-sections. Furthermore, due to the complex nature of unsteady flows, there is a gap in the literature regarding studying the effects of local and convective acceleration in the case of gradually-varied unsteady flows. The current experimental study will concentrate on the flow alterations in the wake of cylindrical structures with different cross-sections in the presence of unsteady flow (i.e. during the passage of a hydrograph) in help to fulfil the aforementioned knowledge gap in the literature. Therefore, in this thesis, an experimental study was conducted comprising rigid bed experiments in a 30m long and 1m wide recirculating flume equipped with a variable discharge pump. Circular cylinders with 9 cm diameter (D=9 cm) are used, and elongated cylinders with aspect ratios of L/D=2, 3 and 4 are also investigated.

To understand the influence of accelerating and decelerating flow conditions, three unsteady cases with different unsteadiness degrees were tested as well as a reference steady flow case. The spatial and temporal variations of Reynolds-averaged velocity and turbulence characteristics around the pile, as well as undisturbed flow, were analysed. Findings show that there are distinct differences between the tested gradually-varied unsteady flow cases and the reference steady flow case.

Three-dimensional velocity measurements were conducted via an Acoustic Doppler velocimeter (ADV) at more than 200 locations for each of the test conditions. Moreover, water level and hydraulics slope values were recorded by use of resistant-type water level sensors. The data were analyzed to obtain spatial and temporal variation of Reynolds-averaged velocities and turbulence characteristics (fluctuating components, Reynolds stresses, turbulent kinetic energy) under steady and unsteady flow case in a comparative manner.

Findings show that there are distinct differences between steady and unsteady flow conditions around bridge piers. Considering circular bridge piers, the wake turbulence was observed to get significantly higher during the rising stage of the hydrograph compared to the falling stage, whereas the turbulence due to lateral flow contraction exhibits an inverse behavior. The near bed flow around the bridge pier was seen to react the changing pressure gradient much quicker compared to the main flow region, where the reaction was much delayed, causing a longer recirculation region during the falling stage of the hydrograph. It is concluded that the flow structures foreseen for steady flow becomes noticeably altered in the case of unsteady flow, and these alterations are suggested to be considered in the engineering practices.

The Reynolds-averaged velocity vs. Turbulence kinetic Energy plots of undisturbed flow indicated a hysteresis effect, such that larger turbulence is generated during the falling stage of the flow compared to the rising stage. This hysteresis was considerably reduced in the pile wake, and even reversed hysteresis was seen at certain cases. The spatial variation of Reynolds-averaged velocity and turbulence in the peak instant of unsteady flow was qualitatively similar to that of steady flow, but quantitatively, turbulence, flow contraction, and velocity deficit in the near-wake region were smaller in the case of unsteady flow. Contrarily, the unsteady flow generated remarkably higher turbulence levels at further downstream in the pile wake. It is concluded that in the case of unsteady flow the pile behaves as if it has a more streamlined shape. The results were also interpreted from structure-bed interactions perspective, explaining the differences between the pile scour induced by steady and unsteady flow conditions.

FARKLI ENKESİT ŞEKLİNE SAHİP KÖPRÜ AYAKLARININ DEĞİŞKEN AKIM KOŞULLARIYLA ETKİLEŞİMLERİNİN İNCELENMESİ

ÖZET

Silindirik yapılar etrafındaki akımlar, hidromekanik disiplininde belki de son 100 yılda en çok araştırılan ve çalışılan konulardan biri olmuştur. Özellikle açık deniz endüstrisinin gelişmeye başladığı 1960'lardan sonra konu ile ilgili bilimsel çalışmalar artmış, 1980'lerden bu yana çok önemli gelişmeler elde edilmiştir. Silindir tabana dik olarak yerleştirilirse (örneğin bir kazık veya köprü ayağı gibi), taban yakınlarında akım özellikleri üç boyutlu olarak değişecektir. Taban yakınında silindirin membaında akım ayrılacak ve silindirin hemen önündeki kabarmadan ötürü oluşan batma akımı (down flow) ve ters basınç gradyanı etkisiyle bu ayrılmış bölgede at nalı çevrisi (horseshoe vortex) adı verilen kuvvetli çevriler oluşacaktır. At nalı çevrisi gelişerek silindirin etrafından mansap bölgesine iletilmektedir. Silindirin yan tarafında büzüşen akım çizgileri (flow contraction) ile hız artmaktadır. Bir yandan da art çevrileri (lee-wake vortices) oluşmaya devam edecek ve mansap tarafında silindirden kopan çeviriler ile Von Karman çeviri caddesi oluşacaktır. Yakın zamanda yürütülen sayısal ve deneysel modelleme çalışmalarında, bu karmaşık akım yapıları daha iyi anlaşılmış ve çok daha net görselleştirilebilmiştir. Bu akım yapıları silindir etrafındaki oyulma mekanizmasından da sorumludur. Akımın permanan olmadığı durumlarda, silindirik yapının etrafındaki akımla etkileşimi permanan akıma göre farklı gelişmektedir. Literatürdeki bazı deneysel bulgulara göre hızlanmakta veya yavaşlamakta olan bir akım altında (permanan olmayan akımlarda) silindirin etrafında ikincil akımların oluşacağı belirlenmiştir. Bu ikincil akımlar özellikle salınımlı akım (oscillatory flow) durumu için çokça çalışılmıştır. Zira salınımlı akım durumu dalga etkisi altındaki silindirik bir yapı için önem arz etmektedir. Literatürde kazıkların etrafındaki akımla ilgili çalışmalar temel olarak üç tip akıma odaklanmıştır: 1) Permanan akım, 2) salınımlı akım (dalga altında akımlar), ve 3) bu ikisinin birleşimi. Silindirlerin tedrici değişken akımlar ile etkileşimlerini inceleyen çalışmalar permanan akım ve dalga durumuna nispetle daha enderdir. Bu çalışmaların önemli bir kısmı, depremler sırasında oluşan tsunami dalgaları ile ilgilidir. Tsunami dalgaları belli ölçülerde akarsu taşkın hidrografı tipinde tedrici değişken akımlara benzeseler de, önemli farklılıkları da bulunmaktadır. Bunların yanında silindirlerle etkileşimde olan gel-git akımları ve nehirlerde oluşan hidrograflar (tedrici değişen akımlar) özellikle hidrodinamik bakış açısından, önceki üç akış koşulu kadar fazla ilgi görmemiştir. Değişken akımlar incelenirken, permanan ve üniform akım kabulleri (her ne kadar pratik mühendislik uygulamalarında başvurulsa da) geçerli olmayacağı için klasik açık kanal akımı denklemleri de doğru sonuçlar verememektedir. Bu geçerli olmama durumu akarsudaki hidrolik parametrelere bağlı olarak gerçekleşen tüm fiziksel süreçleri (örneğin katı madde taşınımı, morfolojik değişimler, yapılar üzerindeki akım kuvvetleri ve türbülanslı dispersiyon, vb.) etkileyecektir. Literatürde kazık ve köprü ayağı gibi silindirik yapılar etrafında deniz ve akarsulardaki akımın incelendiği

çalışmaların büyük bir çoğunluğu permanan akım koşulları altında gerçekleştirilmiş, permanan olmayan akımlar söz konusu olduğunda ise esas olarak ani değişken akımlar (özellikle salınımlı akım ve dalga etkisi) üzerinde durulmuştur. Bir akarsu hidrografının geçişi esnasında rastlanacağı türden tedrici değişken bir akım koşulunda akarsuya yerleştirilen bir köprü ayağı etrafındaki akımın, permanan akım koşulları ile karşılaştırmalı olarak incelendiği bir çalışma literatürde bulunmamaktadır.

Bu doktora tez çalışması ile, tabana dik olarak yerleştirilmiş silindirik bir yapının (örneğin bir kazık veya köprü ayağı), bir hidrografın geçişi esnasındaki tedrici değişken akım ile etkileşimi problemi deneysel olarak incelenmiştir. Dairesel enkesitli köprü ayaklarının yanı sıra, enkesit şeklinin etkisinin daha iyi görebilmek için uzunluğunun genişliğine oranı sırasıyla L/D=2, 3 ve 4 olan uzatılmış dairesel (oblong) enkesitli köprü ayakları da incelenmiştir. Daha önce silindirik yapıların akım ile etkileşimi konusunda birçok çalışma yapılmış olmasına rağmen, literatürde daha ziyade dairesel kesitler üzerinde durulmakta; ayrıca yukarıda belirtildiği gibi tedrici değişken akım durumu ile ilgili ciddi bir bilgi boşluğu bulunmaktadır. Bu çalışma ile literatürdeki bu boşluğun bir nebze doldurulması amaçlanmaktadır. Detayları tez içerisinde açıklandığı üzere fiziksel modelleme yönteminin kullanıldığı bu çalışma kapsamında, ele alınan her bir enkesit tipindeki köprü ayağının etrafındaki akım yapısının nitelik ve niceliksel özellikleri, detaylı hız ölçümleri ile alansal ve zamansal olarak çalışılmıştır.

Çalışma kapsamında İ.T.Ü. İnşaat Fakültesi Hidrolik Laboratuvarı'ndaki 30 m x 1 m x 1 m boyutlarındaki değişken akım kanalında bir deney düzeneği oluşturulmuş, bu düzenek ile bir permanan (kararlı) akım ve üç farklı hidrografın geçişi sırasındaki (tedrici değişken) köprü ayakları etrafındaki akım incelenmiştir. Ayrıca kanala köprü ayakları yerleştirilmeden önceki koşul (bozulmamış akım) ile de deneyler gerçekleştirilmiştir. Her bir deneyde yapılar etrafındaki akım hızı akustik Doppler hızölçer (ADV) yardımıyla 200'den fazla noktada üç boyutlu olarak ölçülmüş, ek olarak direnç tipi seviyeölçerler ile su seviyesi ve hidrolik eğim de kaydedilmiştir. Veriler analiz edilerek Reynolds ortalama akım hızları ve türbülans karakteristikleri (çalkantı bileşenleri, Reynolds gerilmeleri, türbülans kinetik enerjisi, enerji spektrumu) zamansal ve alansal olarak elde edilmiş, permanan akım ve değişken akım şartları karşılaştırmalı olarak incelenmiştir.

Çalışmada elde edilen bulgular analiz edilerek, hem dairesel enkesitli köprü ayakları ile uzatılmış daire (oblong) enkesitli köprü ayakları karşılaştırmalı olarak incelenmiş, hem de üç adet farklı değişkenlik derecesine sahip hidrografın geçişi sırasındaki tedrici değişken akım koşulu ayrı ayrı ele alınarak köprü ayakları etrafındaki akım permanan (zamanla değişmeyen) akım koşulu ile mukayeseli biçimde araştırılmıştır. Diğer taraftan hareketli taban çalışılmamış, yapı etrafında akım kaynaklı oyulma ve birikme gibi "hareketli taban prosesleri" proje kapsamı dışında tutulmuş olsa da, çalışmadan elde edilen sonuçlar değişken akımlar altında köprü ayağı etrafında oluşacak oyulmanın permanan akım durumundaki oyulma ile karşılaştırılması açısından yorumlanmıştır.

Bulgular incelendiğinde, köprü ayağı etrafında permanan ve değişken akım koşulları arasında çok belirgin farklar bulunduğu anlaşılmaktadır. Dairesel enkesitli köprü ayakları özelinde, art iz bölgesindeki türbülans hidrografın yükselme eğrisi esnasında çekilme eğrisine göre bariz biçimde artmakta, ancak köprü ayağının iki tarafında yanal akım büzülmesi dolayısı ile ortaya çıkan türbülans çekilme bölgesinde bir miktar daha yüksek gerçekleşmektedir. Taban yakınında köprü ayağı etrafındaki akım değişen

basınç gradyanına çok daha çabuk tepki verirken akımın üst bölgelerinde daha geç tepki vermekte, bunun sonucu resirkülasyon bölgesi (akım hızının negatif olduğu bölge) çekilme eğrisi esnasında uzamaktadır. Elde edilen sonuçlar değişken akım koşulları altında kararlı akım için öngörülen akım yapılarının farklılaştığını işaret etmektedir. Mühendislik uygulamalarında bu farklılıkların göz önünde bulundurulması önerilmektedir.

1. INTRODUCTION

1.1 Description and Significance of the Subject

Research on flow around marine and hydraulic structures has a long-established tradition in fluid mechanics studies. One of the main topics for this subject is studying the flow around bridge piers or generally supporting piles. Previous research on the reasons for the failure of the bridges indicate that the most frequent causes of bridge failure in the United States of America were not due to design and construction fault, but due to floods and also collisions caused by scour (Wardhana & Hadipriono, 2003). With this regard, understanding flow-seabed/riverbed-structure interaction is of utmost importance for the coastal and hydraulic engineering community and it has received much attention from researchers in the past.

Flow pattern in the neighborhood of a structure drastically changes when confronted with an obstruction (e.g. a vertical cylinder such as a pile or bridge pier), generating a significant force on this cylinder while the cylinder exerts the same amount of resistance on the flow. Other changes of the flow field that occur due to the presence of the cylinder are contraction of the streamlines at the sides, (towards the main channel), and also generation of down-flow at the immediate upstream of the cylinder. The horseshoe vortices occurring at the bottom of the structure develop as the consequence of these flow features and are the main agent of the local scour, (decrease in the bed level as the consequence of the erosion created by the flow), around the abutments or generally piles (Kw An & Melville, 1994).The formation of lee-wake vortices and generation of turbulence are observed behind the obstacle. These changes usually result in higher sediment transport capacity in the vicinity of the structure, the excessive amount of which can reduce the stability of pile-supported marine structures and eventually lead to failure of them. Figure 1.1 illustrates the flow structure around a vertically mounted pile.

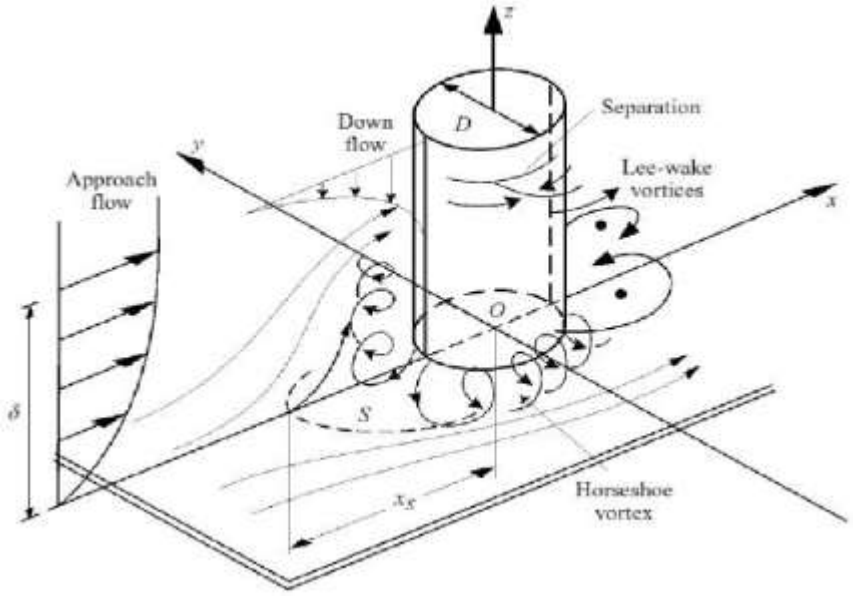

Figure 1.1 : Visualization of flow structure around Bridge pier (Baykal et al., 2015).

The cross section and type of the structure involved in such local scour can vary from simple structures like plain pipelines or piles or it may be a complex structure such as a group of piles, subsea template, and a protection structure with horizontal or vertical members or an offshore platform (Fredsoe & Sumer, 2002).

Given its relevance to a wide range of problems, flow around piles and pile-like structures have been a major topic in coastal and hydraulic engineering. The research efforts in this area, so far, are limited with three types of flow conditions around the pile: (1) steady flow, (2) oscillatory flow, (3) and a combination of both. Gradually varying unsteady flow cases, such as tidal flow or riverine hydrographs, interacting with vertical piles have not received as much attention as the enlisted flow conditions, particularly from hydrodynamics point of view since practitioners generally tend to approach this kind of flows with steady flow approximation. However, experience show that gradually varying unsteady flow cases, such as tidal flow or flood hydrographs, may sometimes cause different scour geometries compared to equilibrium scour depth, which is commonly estimated using peak-flow conditions for engineering design of bridge piers (Lai et al., 2009; Whitehouse et al., 2011). Therefore, it is important to further study and understand the effects of unsteady flow case on flow structure around piles.

1.2 Motivation and Purpose of the Study

The presence of a vertical obstacle, such as a pile, in the flow domain will change the flow pattern drastically. As mentioned above, the local scour, which occurs around the cylinder placed in the flow, is one of the most important consequences of the flow-structure interaction, and it is considered as common reason of collapse in most bridges. Accordingly, the interaction of flow with the structure is a major topic that has been investigated in the last 50 years. However, the vast majority of these studies are based on piles with circular cross sections, and only few of them have focused have focused on piles with different cross sections that are used in practice, like more streamlined cross sections (elliptical, elongated circle, chamfered rectangular, etc.).

On the other hand, unsteady flow is a phenomenon that recurrently happens in streams and open channel flows in nature. In addition, the flow regimes of the rivers are radically changing as a result of stronger downpours in shorter durations due to climate change and shorter concentration times in watersheds due to the change in land use characteristics and industrialization/urbanization. All of these radical changes cause the concentration time and mean flow to decrease, but the peaks of extreme events increase, leading to a more and more "variable" (unsteady/non-uniform) river flow characteristics. Figure 1.2 shows a schematic diagram representing the change in river flows.

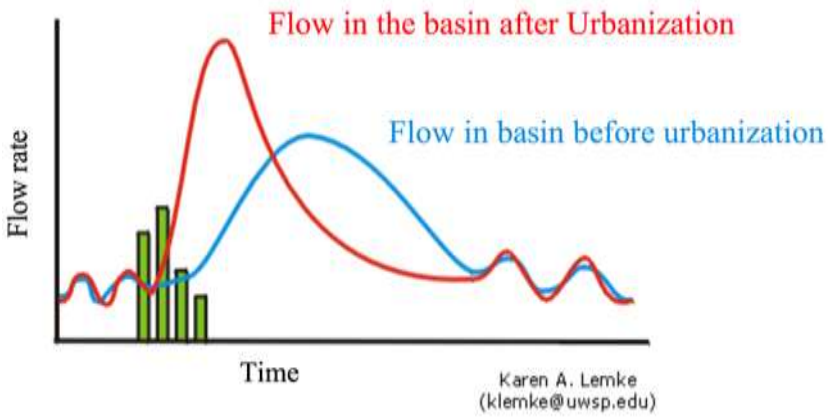

Figure 1.2 : The effects of Urbanization on the flow in basin.

While analyzing these variable flows, classical open channel flow equations are likely to give inaccurate results (although these equations may be used a lot by the designers)

since the “steady and uniform flow assumption” may no longer hold. In previous studies examining the flow around cylindrical structures such as piles and bridge piers, the scope was mostly limited to steady flow conditions, and in the case of unsteady flows the focus was on rapidly varying flows (specifically oscillating flows or waves) (Sumer et al., 1997). To the authors knowledge, there is no study in the literature that focuses on the interaction of gradually varying flow (like the passage of a hydrograph) with the piles placed on the riverbed. Therefore, there are key questions and notions about this subject that have not yet discussed in the literature.

In this thesis study, the unsolved question about the interaction between a vertical cylindrical structure (i.e. a pile) and the unsteady flow will be dealt. Besides the circular cross sections, the flow field around piles with different cross sections including elongated and more streamlined piles are also studied. The findings shall lead to a comprehensive understanding of the effects of unsteady flow on bridge piers with different cross sections used in practice. In order to properly address these questions, experiments were carried out in this investigation.

Another promising line of this research would be to determine the similarities and differences of unsteady flow case compared to the case of steady flow. This will allow us to assess the validity of design methods involving steady flow assumption, and so, help us to figure out what changes/improvements should be made in these methods.

The overall goal of this work is to study and compare the flow structure around a vertical pile in the case of unsteady flows (with different unsteadiness degrees), and compare it with steady flow case. To obtain the desired results the flow and turbulence characteristics (Reynolds normal and shear stresses, turbulent kinetic energy and turbulence production, turbulence macro scale, etc.) are studied.

1.3 Scope of the Study

The current study focuses on the interaction of a vertically installed cylinder (such as a bridge pier or pile) with gradually-varied unsteady flow. For this analysis, it is also of interest to investigate cylinders with different cross sections in order to better observe the effect of cross-sectional shape on the flow. To do so, three different cross sections with length-to-width ratios of L/D=2, 3 and 4 are studied (L is the length of

the cylinder and D is the diameter), and the results are evaluated in comparison with the reference case of circular pile. In the current investigation, physical modeling method is used, by which the flow characteristics are studied in detail by measuring velocity and water level parameters, and calculating the turbulence characteristics of the flow downstream of the cylinder. In order to obtain the flow pattern with precise measurements around each case of the cylinder with a different cross-section, the quantitative and qualitative characteristics of the flow will be analyzed.

Previous studies relied mostly on the local scour around the structure, and no research focused specifically on the flow and variations of flow parameters around the structure, under unsteady flow. Furthermore, almost all the studies in the literature focused on the flow around cylinders with circular cross sections. Therefore, the current study has an essential unique aspect in this area. The results of this study will be useful not only academically but also for the practitioners. This thesis documents several different contributions made to the field of flow structure interaction under unsteady flows and it is believed that the findings obtained from this study will shed light on the future projects regarding the local scour phenomena around cylinders under unsteady flow cases.

2. BACKGROUND

2.1 Fundamentals of Unsteady Flow

Most of the previous studies concerned with steady flows, in which temporal variations did not play a role in changes in flow characteristics, that is, time-independent flow characteristics. Many of the practical applications and types of flows created in open channels do not have the above-mentioned features, and effect of time cannot be eliminated when solving time-related problems. Including the time variation in unsteady flows renders the analysis of the unsteady flow problems much more complex and difficult. Unsteady flow is the flow which properties like depth and/or discharge at a given section changes with respect to time (Chaudhry, 2007); while these changes can be due to natural factors, planned events or accidental events, and can range from water surface fluctuations to oscillating waves and floods resulting in large catastrophes like dam breaks and bridge failures. Some of the most important applications of studying these types of flows is the analysis of the effects of gradually or rapidly varying flows which can have important effects on life of important structures like dams and bridges. In unsteady flows the flow properties change by time, such changes can be triggered by natural processes or events or planned actions. Surges in power canals or tunnels produced by opening or stopping turbines, flood waves in streams or rivers or drainage channels due to rain-storm and/or snow melt or produced by failure of dams, dykes, levees or other control structures, earthquake-induced waves (tsunamis) etc. A schematic description of unsteady flow is presented in Figure 2.1.

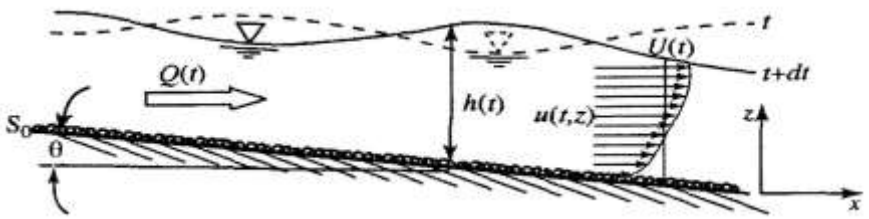

Figure 2.1 : Schematic of Unsteady open channel flow (Qu, 2002).

2.2 Flow Around Cylindrical Structures

2.2.1 Flow regimes around the cylinder

As mentioned before, flow faces drastic changes when encountered an obstacle, such as a vertical cylindrical pile placed on a bed. In current section, we will discuss the regimes of the flow around a circular cylinder and briefly explain the flow changes in the regions around the cylinder. Herein the main flow features around cylindrical structures involve vertically deflected flow (down-flow) in front of the cylinder, a horseshoe vortex system upstream of the cylinder, flow separation beside the cylinder and forming and shedding of the vortices in the wake of the cylinder. (Fredsoe & Sumer, 2002).

Cylinder Reynolds number (Re) illustrates the regimes of the flow around the pile, which is a non-dimensional quantity depending on the cylinder diameter:

$$\mathrm{Re} = \frac{DU}{\nu} \tag{2.1}$$

In this equation, D is the diameter of the cylinder and U is the velocity of the flow, and ν is the kinematic viscosity. The flow regimes around the cylinder alter by increasing Reynolds number. Flow regions around the cylinder are shown in Figure 2.2.

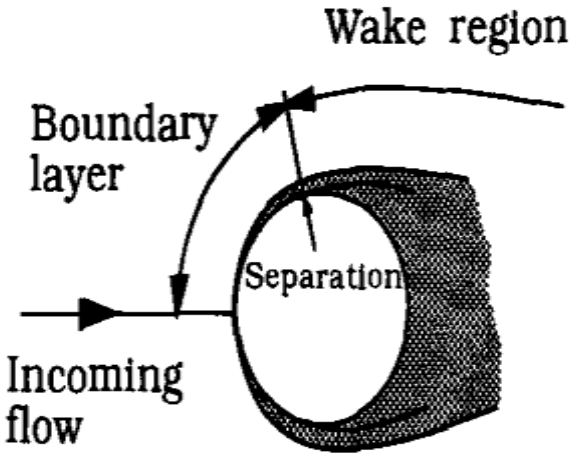

Figure 2.2 : Sketch of flow regions around the cylinder (Sumer, 2006).

Figure 2.3 describes how the flow changes with variations in Re. It is evident from the figure that separation does not occur for very small values of Re. For the separation to occur, Reynolds number should at least be equal to 5. (Figure 2.3a). Figure 2.3b shows

two symmetric stable vortices beginning to form at the range of 5 < Re < 40. As the Reynolds number increases, the wake becomes more unstable leading to the shedding of the vortices in a certain frequency (vortex shedding), subsequently, a street of vortices can be observed at the wake of the cylinder, further increase in Reynolds number will cause the transition of the laminar vortex street (40 < Re < 200) to turbulence. The region of transition moves towards the cylinder as the Re increases in the range of 200 < Re < 300 (Bloor, 1964). According to Bloor (1964) any vortices that form at Re=400 are turbulent. When Reynolds number stands between 300 < Re < 3×10^5, the boundary layer remains laminar (the wake is fully turbulent since Re > 300), and the flow regime in this range is called subcritical regime. There is a narrow range for the Reynolds number in which the boundary layer at the separation point and only in one side of the cylinder becomes turbulent, this regime is called the critical flow regime. The next flow regime according to the range of Reynolds number is called supercritical flow regime ($3 \times 10^5 < Re < 1.5 \times 10^6$) in which the boundary layer separation is turbulent in both sides but the boundary layer itself is not yet turbulent (the region of transition to turbulence is placed somewhere between stagnation and separation points). The upper transition flow regime occurs when $1.5 \times 10^6 < Re < 4.5 \times 10^6$, in which the boundary layer is completely turbulent in one side and half laminar half turbulent in the other side. Finally, when $Re > 4.5 \times 10^6$ the flow regime is called transcritical flow regime in which the boundary layer around the cylinder is turbulent everywhere. The preceding terminology for flow regimes is mostly obtained from Roshko (1961) and Schewe (1983) works.

a) 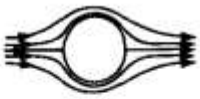	No separation. Creeping flow	Re < 5
b) 	A fixed pair of symmetric vortices	5 < Re < 40
c) 	Laminar vortex street	40 < Re < 200
d) 	Transition to turbulence in the wake	200 < Re < 300
e) 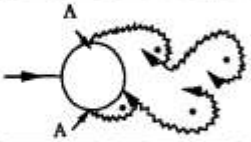	Wake completely turbulent. A:Laminar boundary layer separation	300 < Re < 3×10^5 Subcritical
f) 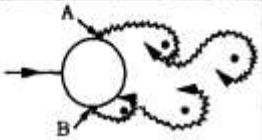	A:Laminar boundary layer separation B:Turbulent boundary layer separation;but boundary layer laminar	3×10^5 < Re < 3.5×10^5 Critical (Lower transition)
g) 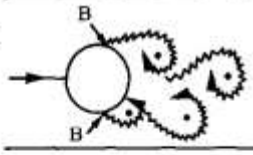	B: Turbulent boundary layer separation;the boundary layer partly laminar partly turbulent	3.5×10^5 < Re < 1.5×10^6 Supercritical
h) 	C: Boundary layer completely turbulent at one side	1.5×10^6 < Re < 4×10^6 Upper transition
i) 	C: Boundary layer completely turbulent at two sides	4×10^6 < Re Transcritical

Figure 2.3 : Flow regimes around the cylinder by increasing the Re number (Sumer, 2006).

2.2.2 Flow features around the cylinder

2.2.2.1 Down-flow

When the flow is blocked or affected by an obstacle (like a cylinder or a pile), with the deceleration in the flow velocity there will be an increase in the pressure while the velocity profile will preserve its logarithmic shape. Due to the pressure distribution, the flow toward the pile is strongly deflected in the vertical direction resulting in two vertical jets starting from the stagnation point. The upper-jet, so called up-flow, is directed to the water surface whereas the lower jet, the down-flow, is towards the bed. The upper-flow produces a flow circulation close to the water surface and the down-flow results in the initial vortex (Figure 2.4).

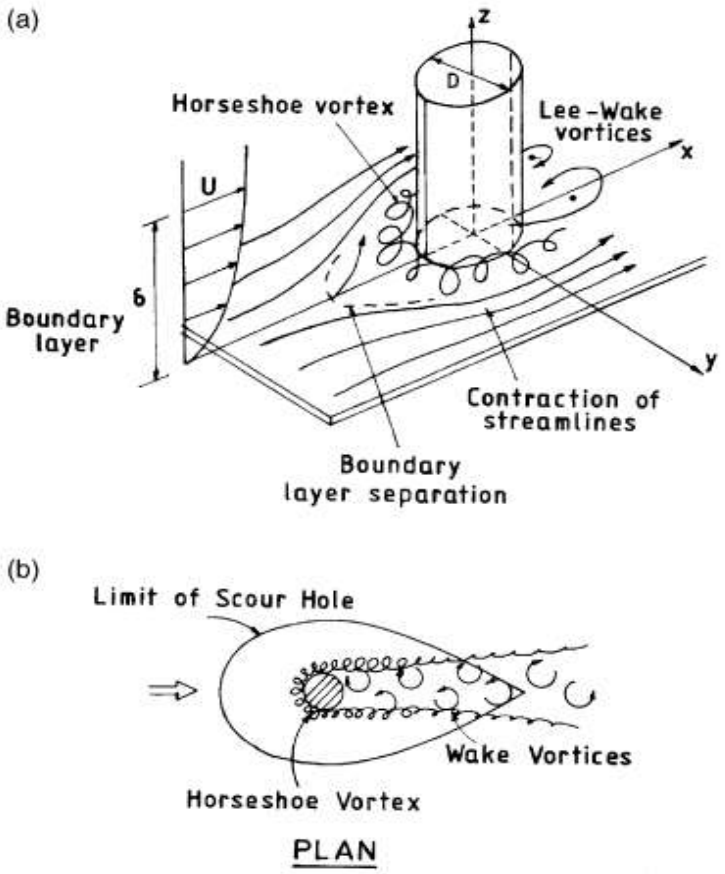

Figure 2.4 : Schematic illustration of Flow pattern around the cylinder (Stevens et al., 1991).

2.2.2.2 Horseshoe Vortex

Horseshoe vortex is a phenomenon that occurs in front of the pile on the bed due to the adverse pressure gradients and down-flow introduced by the presence of the obstruction. In this situation, the incoming boundary layer, which were straight in absence of the cylinder, is separated to overcome the pressure gradient. The separated streamlines roll up leading to formation of vortices (Gazi & Afzal, 2020). These vortices are called horseshoe vortices due to their resemblance to horseshoes. In Figure 2.4b the horseshoe vortices are shown. These vortices are important features in hydrodynamics, which directly influence the depth of the scour around the obstacle and amount of the sediment taken from the bed. Studies show that the strength and dimension of the horseshoe vortices depend on the cylinder Reynolds number (Dargahi, 1989), and the water depth-to-pile diameter ratio (Baker, 1979). The horseshoe vortices enhance the magnitude of bed shear stress, and the intensity of the turbulence. The increased intensity of the flow carries the sediment particles toward the downstream section from the vicinity of the pile, and leads to formation of the scour hole around the pile (Gazi & Afzal, 2020).

2.2.2.3 Vortex Shedding

Another important feature of the flow when the flow faces an obstacle is the vortex shedding phenomenon which refers to the vortices that occur and consequently start to shed due to the boundary layer separation in the adverse pressure gradient. According to the Figure 2.3, these vortices are common to all the flow regimes with $Re > 40$ (Sumer, 2006). The pair of vortices that are in opposite directions, form in the wake. These vortices are usually unstable for small Re. As the Re increases one of the vortices (A, in figure 2.5) gets larger than the other and draws the other one to the wake and this leads to the shedding of the vortex A, and vortex B starts growing and later shedding. The process of forming and shedding of the vortices continue to occur alternately between sides of the cylinder.

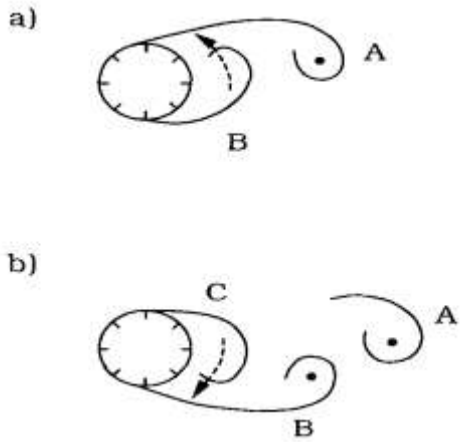

Figure 2.5 : a) Vortex A gets larger in strength and size and draws vortex B downstream b) Prior to shedding of vortex B, later on vortex C is formed and is drawn across the wake (Sumer, 2006).

The frequency of the vortex shedding can be determined by the Strouhal number, which depends on the diameter of the cylinder and flow velocity:

$$St=\frac{f_v D}{U} \tag{2.2}$$

f_v is the vortex shedding frequency, D is the diameter of the cylinder, and U is the flow velocity. Figure 2.6 shows how the normalized Strouhal number varies with the Reynolds number.

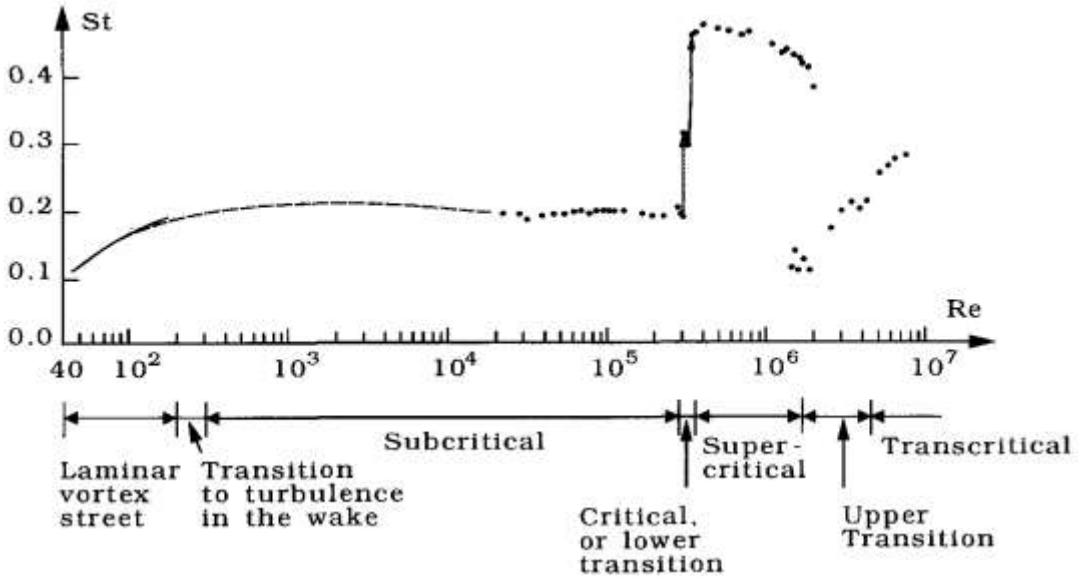

Figure 2.6 : Strouhal number for a smooth circular cylinder. Experimental data from: Solid curve: (Williamson, 1989), Dashed curve: (Roshko, 1961), Dots: (Schewe, 1983).

As explained previously in Figure 2.4 which illustrates the top view and plan view of the flow pattern around the cylinder, down-flow occurs just in front of the cylinder, in the surface of the water there is a small vortex (bow wave) due to adverse pressure gradient which is in the opposite direction of horseshoe vortices. The increase in the velocity in the side of the cylinder is apparent; vortices occurring and shedding in the wake of the hydrograph are also obvious.

2.2.3 Unsteady Flow around the Structures

As described earlier, steady state flow refers to the condition where properties such as depth and velocity of flow does not change with time, otherwise the flow is considered unsteady. Governing equations of steady flows have one dimension less (time) than governing equations of unsteady flows, therefore time variations of all velocity components (acceleration terms) are zero. As a result, it is much easier to solve steady flow cases.

If any variables that define the flow, like velocity or flow depth changes with respect to time, the flow becomes unsteady.

As mentioned above, two parameters such as water depth and flow velocity or flow rate are sufficient to define the flow conditions in open channel flow cross sections, therefore two fundamental equations of open channel flows are enough to solve the flow conditions. Continuity and momentum equations will be briefly discussed here:

In steady flow case, the continuity equations in one-dimension are defined as following:

$$\rho A_1 V_1 = \rho A_2 V_2 \tag{2.2}$$

And the momentum equation is as below:

$$F = \rho Q (V_2 - V_1) \tag{2.3}$$

Governing equations that are used for analyzing unsteady flows are called the 1D Saint-Venant equations. These equations include continuity equation written as:

$$\frac{\partial \mathrm{A}}{\partial \mathrm{t}} + \frac{\partial \mathrm{Q}}{\partial \mathrm{x}} = 0 \tag{2.4}$$

And momentum equation which is written as:

$$\frac{\partial Q}{\partial t} + \frac{\partial}{\partial x}(\beta QV) + gA\frac{\partial y}{\partial x} + gAS_f - gAS_0 = 0 \quad (2.5)$$

$A = A(x,t)$, is the wetted cross-sectional area and $Q = Q(x,t)$ is the flow discharge. Both of these parameters are functions of time and distance in the main flow direction. $V(x,t)$ is the cross-sectional average velocity of the flow, $y(x,t)$ is the flow depth, S_0 is the longitudinal slope of the flume and the S_f is the energy gradeline slope (friction slope) derived from the Manning formula or any other flow resistance relation, g the gravitational acceleration, and β a correction factor related to the cross-sectional time-averaged velocity distribution. The assumptions used for obtaining the Saint-Venant equations are: a) hydrostatic pressure distributions, b) small average bed slope, c) flow is homogenous and incompressible d) streamline curvature is small, from these assumptions $\beta = 1$ and considering $V = Q/A$ the following equation will be obtained

$$\frac{1}{A}\frac{\partial Q}{\partial t} + \frac{1}{A}\frac{\partial}{\partial x}\frac{Q^2}{A} + g\frac{\partial y}{\partial x} + gS_f = 0 \quad (2.6)$$

3. LITERARTURE REVIEW

There have been numerous studies to investigate the flow structure in the case of unsteady, and to find the characteristics of the flow such as the velocity and shear stress variations across the depth in different hydrodynamic studies. As an example,Nezu and Nakagawa (1995) performed a detailed analysis of the structure of the unsteady flow on smooth wall. In their analysis, both the flow and turbulence characteristics of the unsteady flow were calculated. In their experimental analysis, they found that the log-law distribution of the velocity satisfies well in the rising and declining stages of the flow. They observed that the near-bed turbulence was stronger for the rising stage than for the falling one, but for the region near the water surface it was different. The findings of their analysis have shown that there is a big difference between the findings of the flow with varying free surface area and the case where the flow is in closed ducts. One of the important conclusions of their study was finding an anti-clockwise loop between velocity or turbulence and water level changes.Graf and Song (1995) used different methods to calculate the shear velocity in unsteady flow, which is notably important for finding friction factor and critical shear stress.

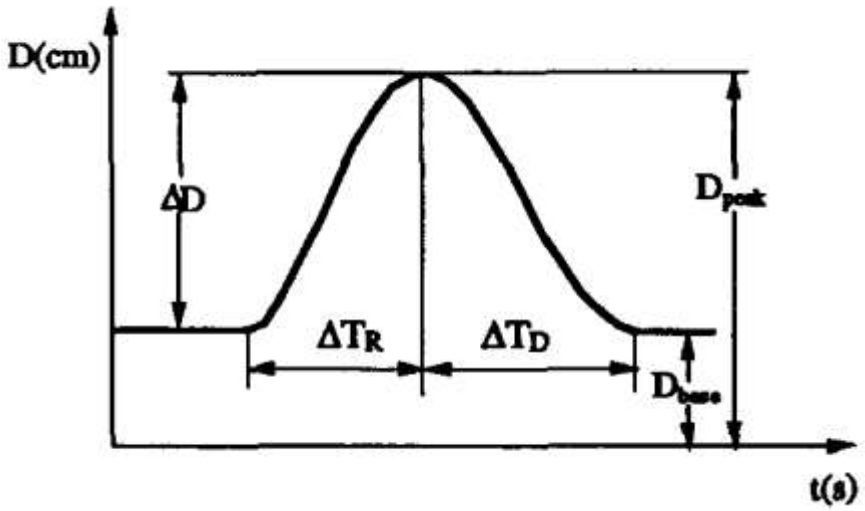

Figure 3.1 : Schematic Representation of hydrograph (Graf & Song, 1995).

In their experimental study, they concluded that friction velocity can be well predicted with three methods presented in their study and that friction velocity increases in the accelerating part of the flood but decreases in the decelerating part of the flood. They did another experimental study in 1996 and covered the characteristics of flow and turbulence in an unsteady open-channel flow with a rough bed. They tested different hydrographs with different unsteadiness coefficients characterized by $\boldsymbol{\Gamma} = \frac{\mathbf{1}}{\boldsymbol{u_b^*}} \frac{\boldsymbol{\Delta D}}{\boldsymbol{\Delta T}}$ as the unsteadiness parameter, where $\boldsymbol{u_b^*}$ is the friction variability of the base flow, $\boldsymbol{\Delta D}$ is the difference between the maximum and the base-flow depth and $\boldsymbol{\Delta T}$ the total lime duration of the hydrograph. They concluded that during the passage of the hydrograph the turbulence intensities were larger in the rising stage than in the falling stage of the hydrograph.

Afzalimehr and Anctil (1999) compared the bed shear stress results obtained by two methods namely parabolic law method and Saint Venant equation in a decelerating flow over a gravel bed. They obtained that for decelerating flows with constant bottom slopes and relative roughness at a specific cross section, as the discharge gets larger the shear velocity estimated by the parabolic method and Saint Venant method gets larger. They also found that the relative roughness might not be adequate to measure the flow resistance of the flow, because at a given cross section the shear velocity is seen to vary depending on the discharge while the relative roughness remains constant.

3.1 Studies of Flow Around Structures

The change in the structure of flow around bridge piers can jeopardize the stability of the bridge by applying excessive loads on the pier, and/or causing bed scour around it. Smith (1976) investigated the reason behind the failure of bridges by considering the failure of bridge data of different countries around the world from 1847 to 1975, and found that one of the key reasons behind the failure of bridges is scour. Bridge failure can cause high scale disaster and lead to loss of life and damage to properties. For this matter, design of a typical pile foundation in marine or riverine structures requires the consideration of not only the structural and geotechnical, but also the hydrodynamic and scour perspectives. With many practical applications in engineering, flow-seabed-structure interaction is now a mature field with many remarkable studies conducted in

the literature (Sumer et al., 1997); (Whitehouse, 1998); (Melville & Coleman, 2000); (Fredsoe & Sumer, 2002). However, there still stands a large prospect in the discipline with many unknowns yet to be studied (Sumer, 2014). A summary of studies involving flow-structure interaction is presented below.

3.1.1 Steady flow studies around structures

In the study of Rao et al. (2004), flow visualization with dye injections at the wake of a circular cylinder mounted on a channel bed with different bed roughness characteristics were undertaken in order to gain new insight into the complex fluid-structure interactions. Three different behaviors for the vortex shedding including periodic alternate Karman type, symmetric vortex shedding and irregular vortex shedding were observed in all the bed types and all the depths. The vortex shedding behavior changed intermittently from one to another but the dominant vortex shedding type was the irregular one. According to their study, with an increase in the ratio of dye injection depth to water depth, y/d, there was decrease in vertical oscillations of the shear layers, decrease in dye dispersion, increase in the width of the near-wake region and also increase in the vortex formation length. In rough beds an increase in the shear layer instability and oscillations were observed according to the smooth bed and upward dispersion of dye along the cylinder axis. They also observed that the horseshoe vortex interaction with Karman vortices evaded throughout the depth and that the non-uniform approach velocity, bed roughness and permeability appear to enhance the influence of horseshoe vortex throughout the channel depth and along the cylinder span.

Kirkil et al. (2005) used a well-resolved LES simulation of the flow past a circular bridge pier and their analysis provided a better understanding of the structure of the horseshoe vortex system near the base at the beginning of scour process. It was observed that the structure of the horseshoe vortex system varies considerably in time, though typically a larger relatively stable necklace like vortical structure is present around the upstream part of the cylinder and oscillates randomly. The global effect of the horseshoe Vortex system is found to increase the local bed shear stress, turbulent kinetic energy and near bed pressure fluctuation. In the case of movable beds, the effect is to scour bed material away from the horseshoe vortex region.

Zhao et al. (2009) used 3D numerical modeling to reproduce the flow visualizations of a flow passing through a circular cylinder at yaw angles in the range of 0-60 degrees. They used Petrov-Galerkin finite element method to solve 3D Navier-stokes equations in order to understand the effects of yaw angle on wake structures, vortex shedding frequency and hydrodynamic forces of the cylinder. Their model showed good results with the experimental results, they found out that the numerical results of Strouhal number agrees well with experimental data when the inclination angle (α) is less than $30°$ and are slightly smaller than experimental data for $\alpha > 30°$.

Flow around cylinders have also attracted attention of researchers of aerodynamics including study of Islam et al. (2013) which focused on trends of changes of separation for steady flow over a smooth circular cylinder and expressed the results in the forms of empirical equations and compared with the results of previously published literature. In addition, Kumar et al. (2018) experimentally studied the effects of the free stream turbulence on flow past a circular cylinder for Reynolds numbers varying from 32 to 15000. They measured the turbulence intensities at the wake of the cylinder for different diameters of the cylinder and for different Reynolds numbers. They observed that the shedding frequency was decreasing with an increase in diameter of the cylinder and reduction in free stream velocity. They also found out that the diameter of the cylinder plays a prevailing role in flow separation and wake transition for a given set of free-stream dominant frequencies.

3.1.2 Unsteady flow studies around structures

Honji and Taneda (1969) did one of the pioneering studies, which investigated the unsteady flow structures around the cylinder by using a flow visualization technique. The variations of the length of the vortices with time was measured with change in the Reynolds number. They observed and measured the vortices change in both impulsively started unsteady flow and for a uniformly varying acceleration with changes in the Reynolds number. They investigated the length of the vortices for different Reynolds numbers, and the occurrence of the small secondary vortices upstream of the main vortices.

In another study done by Kim and Sengupta (2005) they used the numerical SIMPLER method to solve the two-dimensional Navier-Stokes equations in order to study

unsteady viscous flow physics over an elliptic cylinder. They analyzed variations of drag and lift force with change in Reynolds number and elliptic cylinder thickness. Their results demonstrated that amplitudes of lift and drag force oscillations increase with increase in Reynolds number or cylinder thickness, although the amplitude of drag force is much less than that of lift force. The frequency of vortex shedding increases as either Reynolds number increases or length-to-width ratio of the cylinder increases. Furthermore, the rate of change of frequency along with the increase of Reynolds number becomes larger for large values of length-to-width ratio of the cylinder.

Rahman et al. (2007) investigated the flow field characteristics in an unsteady flow around a circular cylinder in laminar and turbulent flow, at Reynolds numbers of 100, 1000 and 3900, using a numerical model based on 2D finite volume method. From this study, they found that the two-dimensional finite volume method computes hydrodynamic forces and captures vortex shedding very well. They also observed that standard k-epsilon model computes drag coefficients accurately. Most of the results presented in their research are compared with experimental data and showed good agreement with other numerical results.

Stringer et al. (2014) used ANSYS and OpenFOAM to solve flow around circular cylinder for Reynolds number ranging from 40 to $1x10^6$. The resulting data is presented for lift and drag forces, Strouhal number, and boundary layer correlation. Despite closely matching case definitions, significant differences are found in the results between solvers; OpenFOAM displays high correlation with experimental data at low to sub-critical Reynolds number values, whereas ANSYS proves to be more effective in the sub-critical and critical regions. This variance demonstrates the sensitivity of the case to solver specific mathematical constraints and that for practical engineering a parameter study is essential. By removing many common variances associated with grid and transient components of URANS (Unsteady Reynolds Averaged Navier-Stokes) computations, the developed methodology can be used as a benchmark case for further codes solving cylindrical structures.

Some of the prior studies focused on unsteady flow effects on the bridge piers. Wei et al. (2015) used the SPH method to investigate the impact of tsunami bore on bridge

piers in their study, for further understanding of dynamic interaction between a tsunami bore and a bridge pier.

In another study (Mrokowska et al., 2015) focused on friction velocity estimations in unsteady flow by using one dimensional Saint-Venant equations, and also two-dimensional Reynolds equations. They also contacted experiments during which they collected water level and velocity data, and they compared different methods for estimating the shear velocity. A comparison of the results of the different formulas show that they performed equivalently accurate for the cases presented in this study.

3.1.3 Pile groups and other complex structures

Different combinations for the piers affect the flow and turbulence parameters and therefore for a better prediction of the scour depth the effects of these flow features on maximum scour depth should be considered in the studies. In the literature researchers used different combinations for the structures to understand its effect on the flow behavior.

Nicolle and Eames (2011) by using a numerical model studied the effect of a void fraction on two-dimensional flows past previous arrays of circular cylinders in their analysis of three different steady flow patterns.

B. Ataie-Ashtiani and A. Aslani-Kordkandi (2012) presented the experimental results of steady flow structure around two circular cylinders in side-by-side arrangement. They reported in their study that this arrangement for the cylinder changes the behavior of the horseshoe vortex and changes the flow field considerably in a way that the streamwise velocity (u) increases between the two piers, which changes the behavior of vertical and transverse deflections at this area in comparison with the outer sides of the piers. The maximum depth of scour was about 15% greater than single pier in addition the extension of scour hole at the upstream side of the piers was larger than that in single pier case. To compare and study the differences of the flow field around single and tandem piers in more detail an experimental study was done by Behzad Ataie-Ashtiani and Abolfazl Aslani-Kordkandi (2012). In their study, they covered and measured the flow and turbulence characteristics. The results show that the appearance of the pier in the downstream changes the flow structure largely especially in the near wake region.

Amini Baghbadorani et al. (2018) did another study to understand the development of scour hole around complex piers. In their study, they tested different models for the pier arrangements, and different durations for the experiments. Bu use of their experimental data and results of previously published studies, they reviewed the performance of predictive equations for maximum scour depth around complex piers and proposed a new equation, which performed better than previous equations.

3.2 Bed Processes Around Structures in Steady and Unsteady Flow

The flow around abutments like bridge piers has attracted researchers' attention due to its importance in the design of coastal and hydraulic structures. Due to the importance of local scour on the stability of structures, majority of previous researchers have applied experimental and numerical methods to study the near bed flow and morphological processes around piles.

One of the initial studies regarding the maximum scour depth around the abutments belongs to Sumer et al. (1992) in which conducted laboratory scour tests with piles subject to waves. In addition to scour studies they carried out bed shear stress measurements and also flow characteristics around the piles such as lee wake and horseshoe vortices around the piles which are demonstrated as two important elements in scour process. Also another important parameter that effects the

Kouchakzadeh and Townsend (1997) also did an experimental study to investigate the impact of lateral momentum transfer on local scour at piles terminating in the floodplain of a compound channel. They concluded the importance of discharge ratio, (the ratio of flow intercepted by abutment and flow related to a specific channel width at the pile end, Q_a/Q_w), Froude number, and critical Froude number (corresponding to the initiation of bed material movement), associated with the sediment size on local scour depth and proposed a relationship for predicting maximum local scour depth at bridge piles.

Graf and Istiarto (2002) investigated the three-dimensional flow field in the equilibrium scour hole around a pile, and experimentally analyzed the flow structures and vortex formation at the upstream and downstream of the cylinder.

Wu et al. (2004) proposed a 1D model, which simulates the non-equilibrium transport of non-uniform total load under unsteady flow, conditions by using a coupling procedure with a direct solution technique. In another study (Wu, 2004) established a depth-averaged two-dimensional numerical model for unsteady and nonuniform sediment transport in open channel. Four formulations were compared in the numerical model to select the most appropriate method for site-specific studies. The model adopted a semi-coupling procedure which the flow computation was decoupled from sediment calculation, but the three components of the sediment module (sediment transport, bed change, and bed material sorting) were solved in a coupled fashion. This semi-coupling procedure was seen to be very stable and computationally efficient. An empirical formula was proposed to consider the effects of the gravity on the sediment transport capacity, and the bed-load movement direction in channels with steep slopes. The model results were tested against several experimental and field cases, showing good agreement.

Chang et al. (2004) did an experimental study to investigate effect of both sediment size and unsteadiness of the flow on scour evolution around a circular pile. According to the data obtained from theirs experiments, a model simulating the scour depth in both steady and unsteady cases was proposed. The experimental results about scour evolution showed that in steady flow, the rate of scour was very high at the early stage of the scouring process, then it decreased quickly as the scour hole develops further. In addition, they found out that in unsteady flow the increase in the peak velocity (the maximum incident velocity value during the flow) had a higher influence on development of the scour in comparison to the time to the peak flow. In addition, their proposed model showed satisfactory performance in simulating the results for the scour evolution around the pile.

In an experimental study, Oliveto and Hager (2005)aimed to clarify the limitations of already proposed equations for scour depth based on laboratory experiments using a hydraulic approach.

Roulund et al. (2005) in a numerical and experimental investigation studied the flow and live bed scour around a circular pile exposed to a steady flow in cohesionless sediment. They studied the influence of three parameters on generation of horseshoe vortex; boundary layer thickness, Reynolds number, and the bed roughness. A 3D

flow code, EllipSys3D was employed to simulate the flow accompanying with a morphodynamic model used to simulate the actual live bed scour process around the pile. The numerical results showed that the size of the horseshoe vortex as well as the bed shear stress under the horseshoe vortex increased with increasing δ/D, in which δ is the boundary-layer thickness and D is the pile diameter. The influence of Reynolds number on the horseshoe vortex was also found to be significant, but they found out that bed roughness effect on horseshoe vortex was not very significant.

Unger and Hager (2006) performed an experimental model to investigate the internal flow characteristics of a circular cylinder. In their analysis, using particle image velocimetry (PIV) as a non-intrusive and instantaneous velocity measurement tool, they concentrated on a detailed temporal description of the horseshoe vortex and the down-flow characteristics of the circular bridge piers embedded in the sediments and tried to observe how these flow characteristics change over time.

In a field study, Ghorbani (2008) studied the scouring process in six bridges on three rivers, and found the effects of water depth and velocity, sediment characteristics, and bridge pier geometry on the scour depth. A field-based uncertainty analysis was conducted to provide a very rough estimate of the risk associated with scour. Statistical and physico-mathematical methods were used to present the results. The comparison of field data was made with some of the empirical equations. A statistical analysis was carried out to evaluate the statistical randomness and degree of uncertainty of parameters such as pile diameter, water depth and velocity on local scour depth. From this analysis, it was found that as the particle size of the sediment increased, the depth of the local scour decreased. A comparison of scour equations with field measurements revealed the equations with good agreement with field data.

Initiation of motion of bed sediment on gravel bed was investigated in an experimental study by Rasooliyanfar and Afzalimehr (2007). Flow type was steady decelerating and two different grain size for fixed-bed and mobile bed cases were used. The results showed that both the Parabolic Law Method (PLM) and the Reynolds stress method performed comparably well in calculation of the shear velocity. It was seen that the shear stress distribution was in a convex form over both fixed and mobile beds. Due to this method, the critical Shields parameter value for decelerating flow is less than the values stated in the literature.

Lai et al. (2009) analyzed characteristics of scour depth evolutions at piles for different hydrographs. They used data from different experimental studies, and proposed an empirical equation. They tested a Γ-shaped hydrograph representing the rising part of the hydrograph and they aimed to find its effect on maximum scour depth.

Whitehouse et al. (2011) studied the scour at offshore foundations (mostly gravity-based foundations), and compared the results of laboratory and field data with two available empirical equations for evaluating scour depth. They came up with some guidelines about scour management throughout the life cycle of the structures.

Tafarojnoruz et al. (2012) tested the effectiveness of some countermeasures against pile scour, and proposed some methods. They tested their methods on both steady and unsteady flows for piles with circular and rectangle cross sections. The results showed that the combined countermeasure had an efficiency of about 63% in decreasing scour depth for a single circular pile; however, higher efficiency (about 75%) was achieved for rectangular pile, and two in-line circular or rectangular pile applications.

Amini et al. (2012) experimentally investigated the clear water scour at pile groups under steady flows at threshold velocities. Based on the results of this analysis, a new method was proposed to predict the effect of pile group arrangement, pile spacing and submergence ratio on local scour depth. The proposed method was seen to make accurate estimates of the depth of the scour.

Mohamed et al. (2015) experimentally and numerically studied the effect of shape of bridge piers with different lengths of collars on the developments of local scour. Three-dimensional computational fluid dynamic models based on finite volume method to solve the Navier-Stokes equations were created by using SSIIM software. They concluded that the relative scour depth decreases as the relative radius (ratio of radius to width of the pier) of pier edge increases. The results of numerical models using SSIIM were found to be well correlated with the measured data for different experimental models.

Baykal et al. (2015) did a comprehensive three-dimensional hydro-morphodynamic model to investigate flow and scour around a vertical circular pile exposed to a steady current. Their model was also used to study the effects of the unsteady flow features on the scour around a vertical pile. In the numerical model, they studied the location

where vortex shedding occurred, and its frequency close to or away from the bed. The influence of unsteady flow structures and suspended sediment transport on the scour around the vertical pile was studied considering different scenarios in which the systematic features were turned on and off.

Yagci et al. (2017) experimentally studied and presented the clear-water scour and deposition patterns around hexagonal arrays of circular piles in steady flow conditions. The flow variations behind the piles were seen to depend on the solid volume fraction (area covered by piles to the total area of the structure) of the obstacles as well as on the angle of the attack of the incoming flow. The experiments were carried out under different array densities and orientations. The arrays with the higher solid volume fraction generated scour/deposition patterns similar to solid pile. So that according to their study the array of piles could generate 27% less scour volume and 22% less scour depth compared to its single solid pile counterpart. Therefore, their study presented an alternative pile configuration that induces less scour than a single large pile.

In an experimental study, Kitsikoudis et al. (2017) investigated the effect of downstream inclination of a pile on the scour pattern and near wake flow alteration around it. The experiments were carried out under steady flow conditions for three different inclination angles of the pile. The results were compared with the upright pile. The results showed that as the inclination increases the scouring decreases, and also the vertical mixing gets significantly enhanced behind the inclined cylinder while the lateral mixing gets weakened at the upper flow region. An upward flow was seen at the immediate downstream of the inclined pile close to the bed, which became stronger with the inclination angle. It was also observed that with an increase in the inclination angle, the pile became more streamlined, and consequently, the vortex shedding got suppressed.

In a recent study Guan et al. (2019) focused on the development of horseshoe vortex, which drives the scour mechanism around a pile. The formation and evolution of vortices observed in different scour stages and the flow and turbulence parameters measured in this study provided new insight into the flow-sediment interaction around piles.

4. METHODOLOGY

In this experimental analysis, the flow structure around piles with different cross-sections was examined. Moreover, in order to analyze the effect of flow type on the structure of flow around the piles, various flow cases including steady and unsteady flows (with different coefficients of unsteadiness), have been tested. The rectangular recirculating flume with a rigid bed was used in the experiments. Details of the experimental set-up, instrumentation, and procedures are presented in this chapter.

4.1 Experimental Setup

4.1.1 Flume

The experiments were conducted in the Hydraulics Laboratory of Istanbul Technical University. The utilized flume is 30 m long, 1 m wide, and 1.25 m deep with glass sidewalls and smooth concrete horizontal bed (roughness height k < 0.2 mm). A recirculating pump provides the flow in the flume. Figure 4.1 shows the flume used in this study.

Figure 4.1 : Flume and the recirculating pump used in the experiments.

At the inlet of the flume, a flow straightener honeycomb system was used to minimize the lateral velocity oscillations induced by the swirling motion of the water flow during the entry. Figure 4.2 represents the honeycomb system used in the flume.

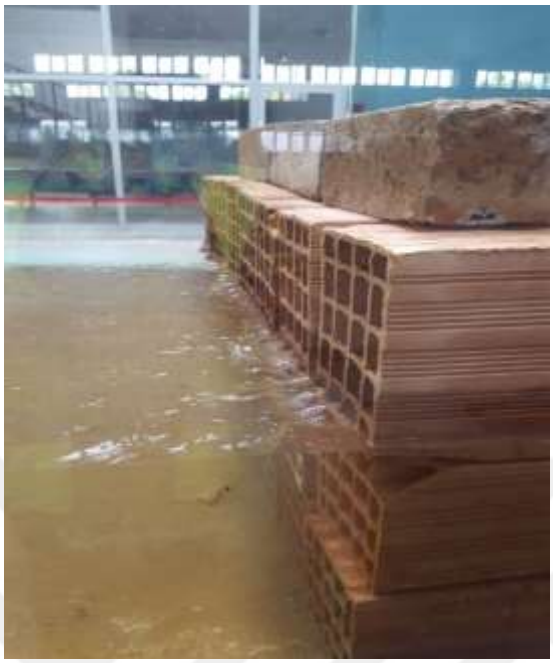

Figure 4.2 : Honeycomb structure at the flume inlet.

4.1.2 Instrumentation

4.1.2.1 Invertor control

As stated earlier, in the current experiments, the recirculating pump provides the necessary flow of water in the flume, and the Inverter Control adjusts the pump discharge. With this inverter, the discharge of the pump can be regulated as a predesigned function of time. The use of the Inverter Control makes it possible to generate both steady and unsteady types of flow. As such, unsteady flows with different times for rising and falling stages of the hydrographs can be generated. Therefore, in this study we produced unsteady flows with different unsteadiness degrees. Figure 4.3 presents the inverter used in the experiments.

Figure 4.3 : Control invertor used for flow adjustments**.**

4.1.2.2 Velocity measurements by ADV

Pointwise velocity measurements for studying the flow field in this study were performed by using an Acoustic Doppler Velocimeter (ADV). The ADV used in experiments was a Nortek Vectrino II, and it had a flexible probe with four receivers and one transmitter. The ADV was installed on a traverse system that makes it possible to move the instrument in all three alignments with high accuracy. The experiments were carried out with particle rich water, which facilitated satisfactory functioning of the ADV with high correlation (≥ 95%) and signal-to-noise ratio (≥ 30%) except a few measurement locations. Figure 4.4 displays the ADV used in the current study with an instant of installation in the flume.

Figure 4.4 : Acoustic Doppler Velocimeter used in this study (left), and its installation on the traverse system (right).

4.1.2.3 Water level measurements

In order to measure time series of water level at the upstream and downstream of the piles installed in the flume, two high-precision water level probes were used, and the hydraulic slope variation during the flow was obtained. The probes were placed at a distance of 2.5 m in the upstream and 2.5 m downstream of the pile, with a total distance of 5 meters from each other. (In no pile cases, water level measurements were also done, and ADV was installed in the middle of these probes.) The water level probes are connected to a linearizer flow monitor manufactured by HR Wallingford. These probes operate by measuring the electricity potential between two stainless steel wires submerged in water, and are simple, reliable instruments for measuring changing water levels in physical models. This potential is converted to an output voltage that is directly proportional to the immersed depth of the probe. To obtain and record the data, the flow monitor was connected to a PC via an NI DAQ data acquisition box. The analysis software, which gives the time varying voltage change by changing the water level, was capable of capturing even very small changes in the water level with high resolution. Figure 4.5 shows the probe and the wave monitor used in this study.

Figure 4.5 : Wave monitor and probes installed in the flume**.**

4.1.2.4 Cross sections used for the pile models

The experiments carried out in this study were done for two cases: (1) with no pile in the flume, and (2) with the pile installed. In experiments with piles, four different cross sections, including one circular and three elongated cross sections were used. In the circular cross-section, the pile diameter was chosen as $D = 9$ cm. For defining the dimensions of the cross sections used in the experiments, the L/D ratio is defined, in which L is the length of the cross section of the pile in the streamwise direction. For circular pile $L/D = 1$, for other cross sections this ratio is presented in Table 4.1.

Table 4.1 : Geometry of cross sections used in the experiments.

			
L/D=1 Circular	L/D=2 elongated	L/D=3 elongated	L/D=4 elongated

Figure 4.6 illustrates the configuration used in the circular pile model with ADV and positions of the water level probes.

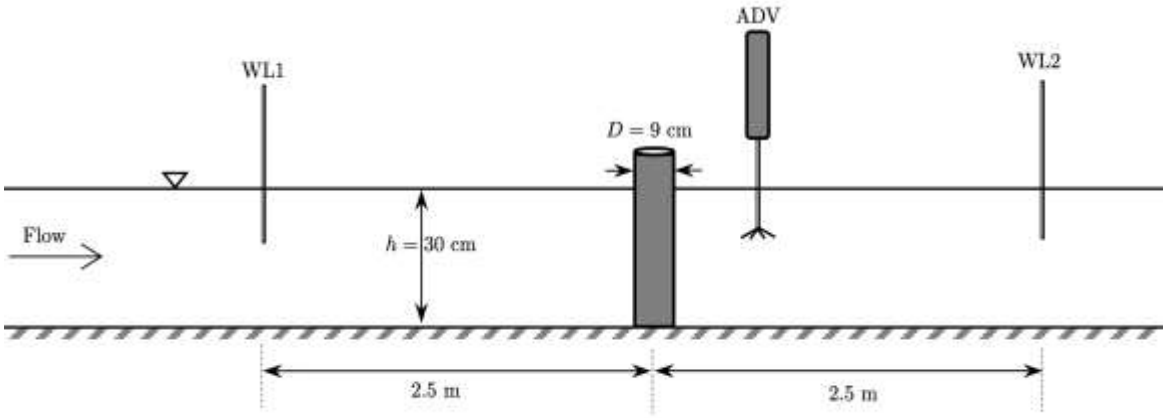

Figure 4.6 : The experimental setup in the flume- WL1 and WL2 are water level probes.

4.2 Experimental Procedure

The data in this study consists of pointwise velocity measurements, and water level measurements conducted at determined points downstream of the piles. The procedure to be followed is based on the studies that were done as preliminary tests. At this stage,

many tests were carried out, and final decisions about the measurement grids, flow types, and other relevant conditions about the experiments were decided.

The water budget in the flume was kept controlled during the experiments such that the water depth at the measurement section, in the mid-length of the flume, was maintained constant at $h = 30 \pm 0.5$ cm throughout all the experiments conducted with steady and unsteady flows. In this way, the influence of water depth variations and hysteresis stemming from the change in water depth is omitted, and only the effect of local and convective acceleration of the flow can be studied. Before each experiment water level probes were re-calibrated, and this new calibration coefficient was used to convert the voltage output of the probes to water depth. Figure 4.7 depicts an example calculation of calibration coefficients used for the water level measurements. As explained previously in Figure 4.6, there are two probes used in this study, one is installed in the upstream of the measurement section (pile location), and the other is placed in the downstream, with equal distances from the measurement section.

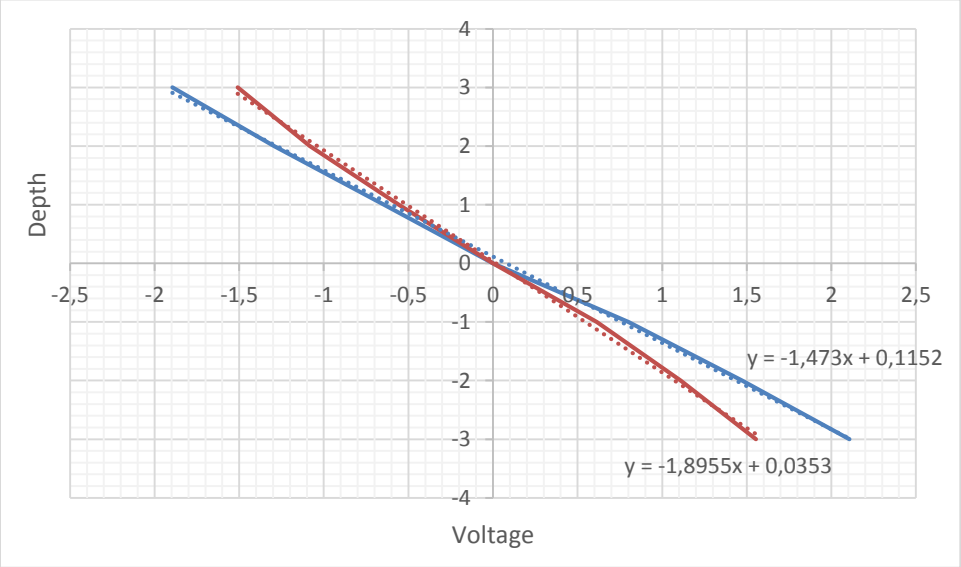

Figure 4.7 : Example calibration curves for calculation of water depth from the voltage output.

The instantaneous velocity measurements were done by using ADV (section 4.2.1). ADV measures the flow velocity in three steps: (1) ultrasonic (high frequency acoustic) signals are transmitted by the four beams of the instrument, (2) these signals are reflected back from the small particles in the water passing through the sampling volume of the instrument (roughly 5 cm away from the probe tip), and (3) the reflected

signal is received back and processed to read the Doppler shift in the signal. In order to improve the performance of the velocimeter, the water was circulated to ensure enough floating particles and higher accuracy of the measurements.

As stated above, the experiments consist of "with pile" and "no pile" cases. In both of these cases two flow types, steady and unsteady flows, are defined. The setup used for the velocity measurements was similar to that of Kitsikoudis et al. (2017). In the case of no pile experiments, the measurement points were established on the vertical line in the middle section of the flume, as shown in Figure 4.8. As seen, 20 points are used to obtain the velocity profile. The measurement points near the bed are denser, and they become sparser away from the bed. The same measurement grid was used for both steady and unsteady no pile cases.

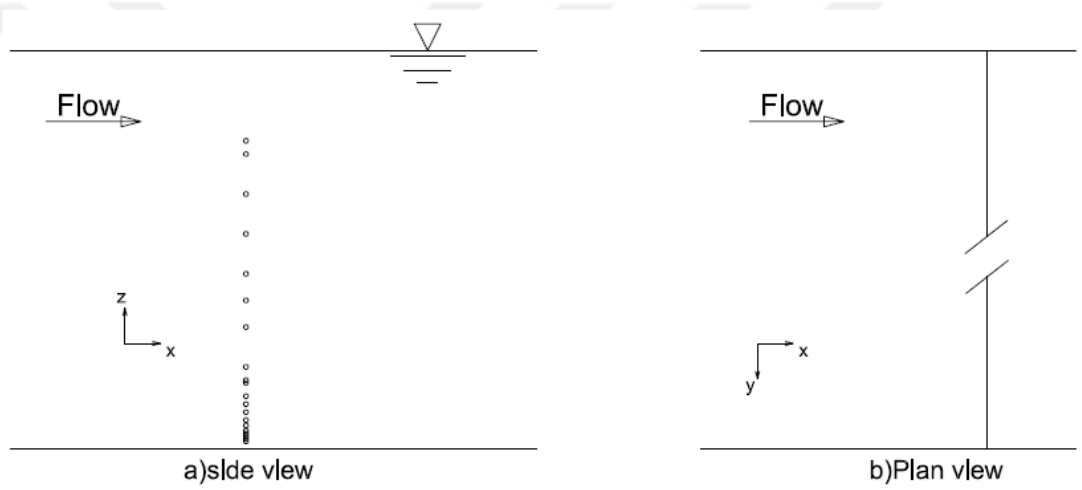

Figure 4.8 : Measurement points in no pile case.

For the experiments with the pile, pointwise velocity measurements were performed across two different planes: 1) The vertical (xz) plane along the centerline at the downstream of the pile and 2) the horizontal (xy) plane at a distance 16.5 cm ($z/h = 0.55$ or $z/D = 1.83$) from the flume bed. Velocity measurement grids over these planes are depicted in Figure 4.9. As shown in the figure, x represents the streamwise direction, y is the transverse, and z is the vertical direction of the depth. Close to the cylinder, the points are placed denser, and away from the pile the measurement points are sparser due to the relatively mild streamwise gradients of velocity and turbulence parameters. In addition, Figure 4.9b shows that measurement points are extended to the contraction region (the region at the side of the pile). In this region, the streamlines are contracted causing an increase in the flow velocity.

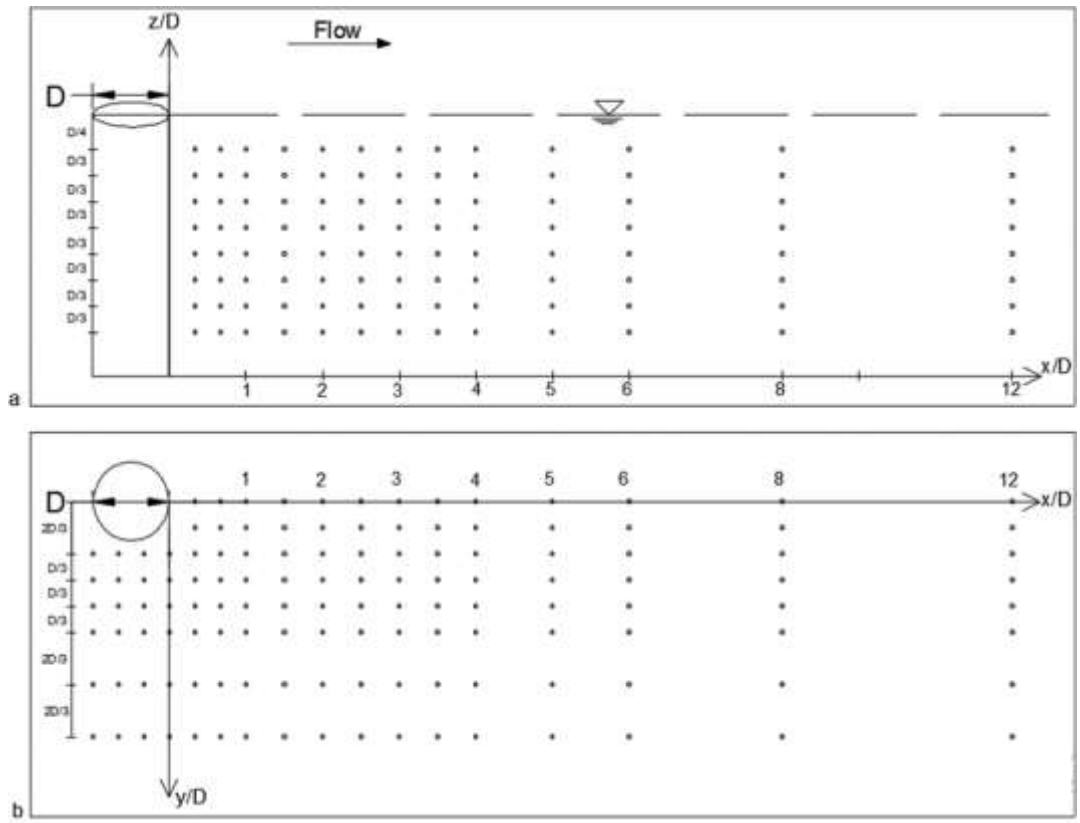

Figure 4.9 : Velocity measurement grids for experiments with pile, a) Grid on the Vertical plane (x-z) along the flume centerline b) Grid on the horizontal (x-y) plane at $z/h = 0.55$ or $z/D = 1.83$.

For elongated piles, there are more measurement points due to their longer cross sections. Table 4.2 represents the total number of measurement points for all the cross sections investigated in the study.

Table 4.2 : Geometry of cross sections and number of points in each case.

Experiment	No pile	L/D=1 Circular	L/D=2 elongated	L/D=3 elongated	L/D=4 elongated
Number of Measurement points	20	232	244	268	286

For the experiments in steady flow case, ADV was placed at each measurement point, and the velocity was measured for 90 seconds. For the unsteady flow cases each velocity measurements started from the base velocity (V_{min}), thereafter followed by the rising stage of the unsteady flow (accelerating) during which the discharge is linearly increased and the velocity reaches to its peak, (V_{max}). Then the peak discharge is kept steady for 20 seconds. Finally, velocity is decelerated back to its initial value.

The measurements were repeated for each point shown in Figure 4.8 and 4.9. Here $V\ (t)$ is cross sectionally averaged velocity:

$$V(t) = \frac{1}{h}\int_0^h \bar{u}(t,z)dz \tag{4.1}$$

where t is time, z distance from bed, and $\bar{u}(t,z)$ is Reynolds averaged streamwise velocity of the undisturbed flow (i.e. the no pile case). To investigate the effect of the unsteadiness on flow structure, three different unsteady flow cases with different unsteadiness degrees are examined. The entire duration of the flow is shown by Δt. Considering different experimental results in the preliminary tests, three different unsteady flow cases with different values for the base time of the hydrograph were chosen. In these hydrographs the minimum and peak discharges were kept constant for all the cases and the parameter that varied was the base time of the hydrograph (Δt). Subsequently the three different times used for the hydrographs are 90s, 120s and 150s. As such, including the steady flow case, which is considered a reference case, four types of flow are studied in this research.

In order to define the unsteadiness degree, an unsteadiness coefficient is defined. There are several non-dimensional parameters suggested in the literature that characterize the coefficient of unsteadiness (Bombar, 2016), within the framework of this analysis, equations 4.2 (Baykus, 2015) and 4.3 are used for the degree of unsteadiness.

$$\Lambda = \frac{\Delta q}{\Delta t}\frac{1}{V_{max}^2} \tag{4.2}$$

where $\Delta q = \Delta V.h$ is the difference of maximum and minimum discharge values, $\Delta V = V_{max} - V_{min}$, is the difference between maximum and minimum cross-sectional average velocity values, V_{max} and V_{min} are the maximum and minimum cross-sectional averaged velocity of the flow, respectively, and Δt is the total time duration of the flow. The Λ values for the flows in the study are presented in Table 4.3. The Λ parameter is a measure of the ratio of average acceleration terms to the inertia terms of the peak flow.

Another parameter for the unsteadiness coefficient can be defined by Equation 4.3.

$$\Upsilon = \sqrt{\frac{q_{max}-q_{min}}{\Delta t}}\frac{h}{\nu} = \sqrt{\frac{V_{max}-V_{min}}{\Delta t}}\frac{h^{3/2}}{\nu} \tag{4.3}$$

Here ν is the kinematic viscosity. The unsteadiness parameter Υ can be interpreted as the ratio of the acceleration term to the viscous forces. We can also treat this as the Reynolds number for unsteady flows (Gargari et al., 2021). This latter unsteadiness parameter utilizes the comparison of present investigation with those conducted for tsunami flow in the literature (for example Larsen et al. (2017)).

For unsteady flow experiments, a modified Keulegan-Carpenter number for unsteady flows, KC_u, is also used to express the variation of unsteadiness with respect to the pile diameter.

$$KC_u = \frac{V_{max} - V_{min}}{D} \Delta t \tag{4.4}$$

In these experiments, the KC_u values for the unsteady flows are 190, 250 and 300. Same as in the case of waves, as KC increases the flow around the pile tends to steady flow (Gargari et al., 2021).

Table 4.3 presents the characteristic parameters of flow cases adopted in the experiments. In this table, "S" indicates the steady flow, and "U" indicates the unsteady flow cases.

Table 4.3 : Flow properties used in the study.

Flow type	Steady (S)	Unsteady 1 U1	Unsteady 2 U2	Unsteady 3 U3
Δt(sec)	-	90	120	150
V_{max}	-	0.23	0.25	0.23
V_{min}		0.04	0.03	0.03
Λ	-	0.01	0.008	0.007
Υ	-	7.5×10^3	7×10^3	6×10^3

Figure 4.10 shows the time variation of cross-sectional average velocity (hydrograph) of the undisturbed flow in the three different unsteady flow cases that were studied in the experiments. As presented in the figures, it is observed that $V(t)$ does not increase monotonically, but it exhibits local maxima in the peak as well. The U1 and U2 hydrographs consist of dual peak and the U3 flow has a single-peak.

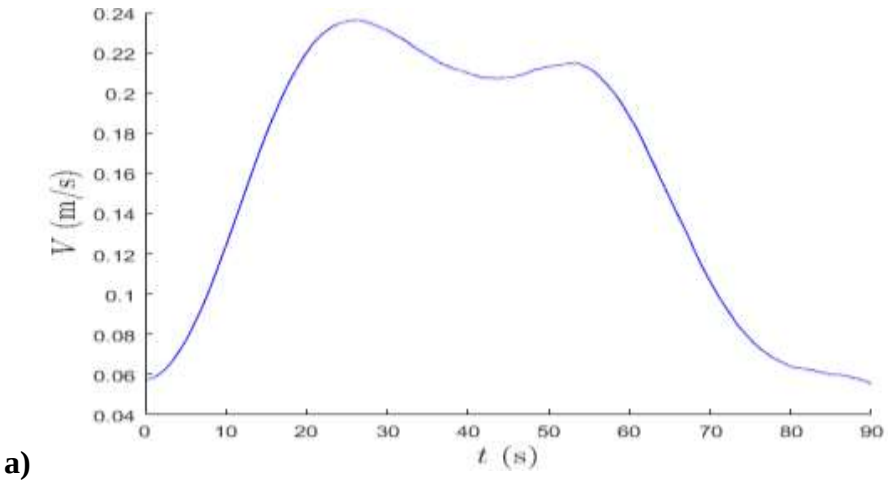

a)

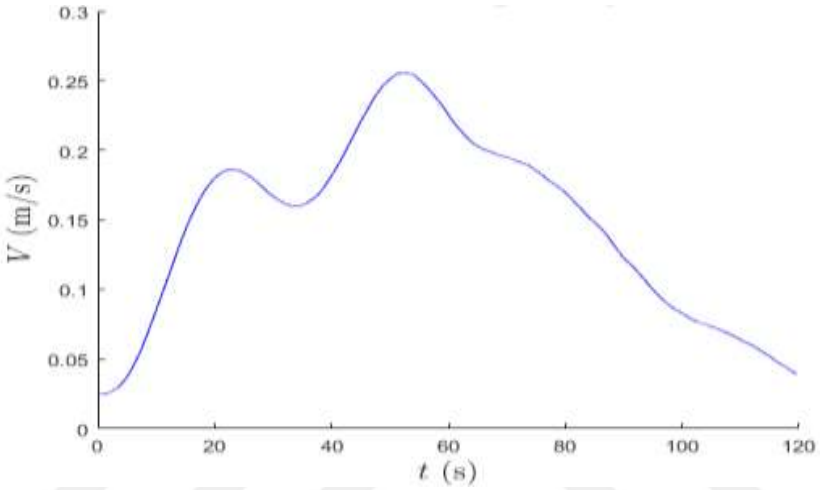

b)

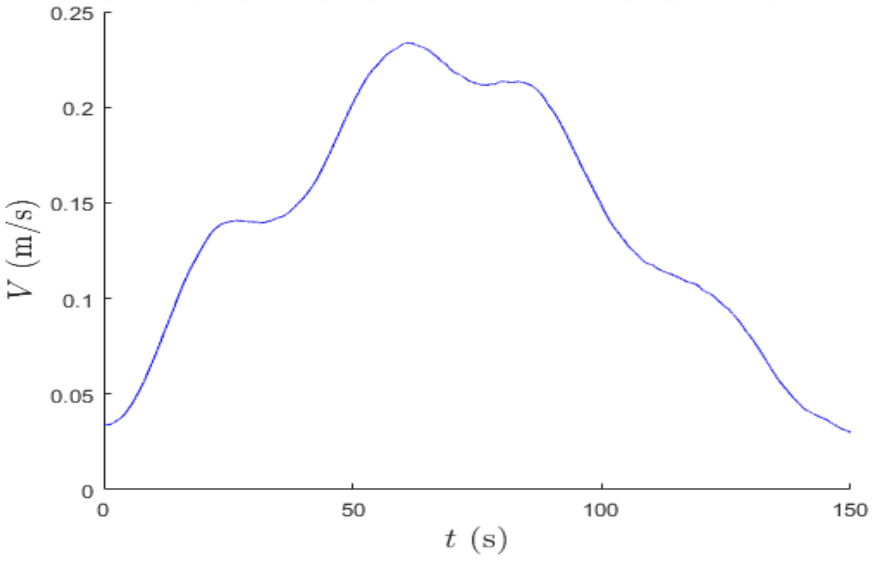

c)

Figure 4.10 : Cross-sectional averaged velocity as a function of time, V(t) in the three hydrographs used in the study. a) U1, b) U2, and c) U3.

4.3 Data Analysis Procedure

MATLAB is used in the synchronization, processing, evaluation and visualization of the test data in this study. As included in Table 4.2, approximately 200 to 300 tests are carried out in each set of experiments, and processing the raw data of these experiments one by one presents major difficulties. To tackle with this difficulty, codes (scripts) were written during the evaluation of the experimental data, which provided efficiency in repetitive processes, so that the data could be reliably analyzed within a whole.

4.3.1 Despiking raw data

As outlined above, the velocity data was measured and collected using ADV. According to the procedures that were taken in the preliminary tests, the first step done for analyzing the raw data is detecting and removing/replacing the spikes (data points of incorrect interpretations of the ultrasonic signals) among the data. For this purpose, the despiking process was applied using a subroutine, which excludes spikes and noise from Acoustic Doppler Velocimetry (ADV) data by phase-space method. This method was first presented by Goring and Nikora (2002), later modified by Wahl (2003) and further modification to this method was performed by Mori et al. (2007). In this way, the outliers are removed and a smoothed data set is attained.

4.3.2 Turbulence Decomposition Method

Once the raw data is obtained and despiked, decomposition of Reynolds averaged and fluctuated velocities is to be performed. Due to the time dependence nature of the unsteady flow, time averaging cannot be used for decomposition of turbulence from the instantaneous velocity time series. Furthermore, the ensemble averaging technique used for wave boundary layers ((Jensen et al., 1989) and (Sumer et al., 2010)) was not possible to apply to all the data within practical limits. Therefore, a convolution technique based on Savitzy-Golay type filter was used to decompose the instantaneous velocity signal into Reynolds averaged velocity and turbulence fluctuations. (Savitzky and Golay (1964) and Schafer (2011)).

In this method (called the S-G method), the least-square smoothing of the time series velocity data is applied over a window size of $N = 1 + 2M$ data. As such, the time-dependent Reynolds-average velocity signal can be obtained. For the sake of

convenience, the filter was chosen as 1st degree. A similar technique based on moving-average was previously applied by Williams et al. (2003) on field data measured via Acoustic Doppler Current Profilers (ADCP), who obtained satisfactory results. The sensitivity analysis showed that a window size of 10 s gave the best results, and that a window size between 7 s and 13 s did not significantly alter the output signal.

To verify and compare the S-G method with ensemble averaging method, a series of verification experiments was carried out. In these experiments, 40 consecutive hydrographs with identical flow characteristics were utilized. The results of Reynolds averaged and fluctuating components obtained by ensemble averaging were compared with those obtained by S-G method. As stated above, it is observed that Savitzy-Golay filter converges to the average for 7 to 13 seconds of time window and therefore it is decided to proceed with a window size of 10 secs (equivalent to N = 1001 data points sampled with a constant frequency of 100 Hz).

The procedure used for decomposing by S-G method is explained as following:

1) Apply 1st degree Savitsky-Golay filter on the instantaneous flow velocity components u, v, and w (along x, y, and z axes, respectively) over a window size of $N = 1 + 2M$ data, and obtain the time dependent Reynolds-averaged velocities u(t), v(t), and w(t),

2) Obtain the fluctuating velocities $u' = u - \bar{u}$, (likewise v' and w').

3) Calculate the time dependent Reynolds normal stresses $\overline{u'^2}(t), \overline{v'^2}(t)$, and $\overline{w'^2}(t)$ by taking the variance of fluctuating velocities over a window size of $N = 2M + 1$:

$$\overline{u'^2}(t) = \frac{1}{N}\int_{n=-M}^{M}(u'_n - \overline{u'})^2 \tag{4.5}$$

4) With the same approach, calculate the time dependent Reynolds shear stress $\overline{u'w'}(t)$:

$$\overline{u'w'}(t) = \frac{1}{N}\sum_{n=-M}^{M}(u'_n - u')(w'_n - \overline{w'}) \tag{4.6}$$

Figure 4.11 shows the results of decomposition technique applied for Unsteady (U3) case. In this figure, the upper pane is the cross-sectional averaged approach velocity (no-pile case for U3 flow case) the middle and lower panes are the raw and mean velocities, which were respectively recorded at a near-bed point and a point close to the surface.

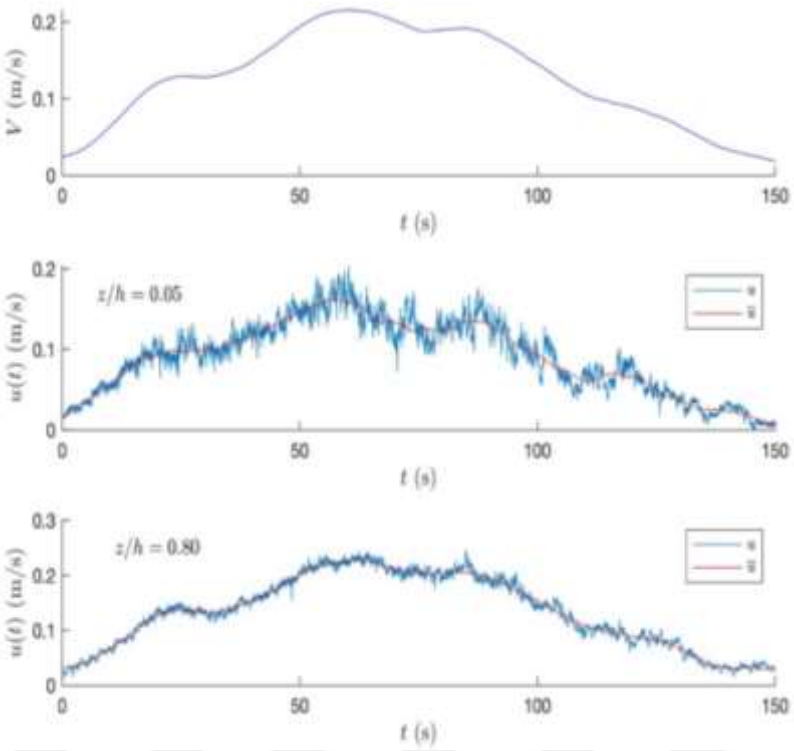

Figure 4.11 : An example application of Reynolds decomposition of instantaneous velocity recorded during U3, no-pile case. Upper pane: Cross sectional averaged velocity. Middle pane: Near-bed velocity. Lower pane: Near-surface velocity.

For the comparative synchronization (overlapping) of repetitive velocity test series, the time series of water surface slope were utilized as the reference signal, which were obtained from the water level measurements. In this method, a parameter named "keytime" is defined in the MATLAB code for each hydrograph, which shows the exact instant of the maximum time-averaged hydraulic gradient during the hydrograph. And then knowing the base time of the hydrograph, the start and end time of the hydrograph is defined with respect to the keytime (Figure 4.12). A consistency check was also performed for each of the synchronized velocity time series to see if there were any errors during synchronization.

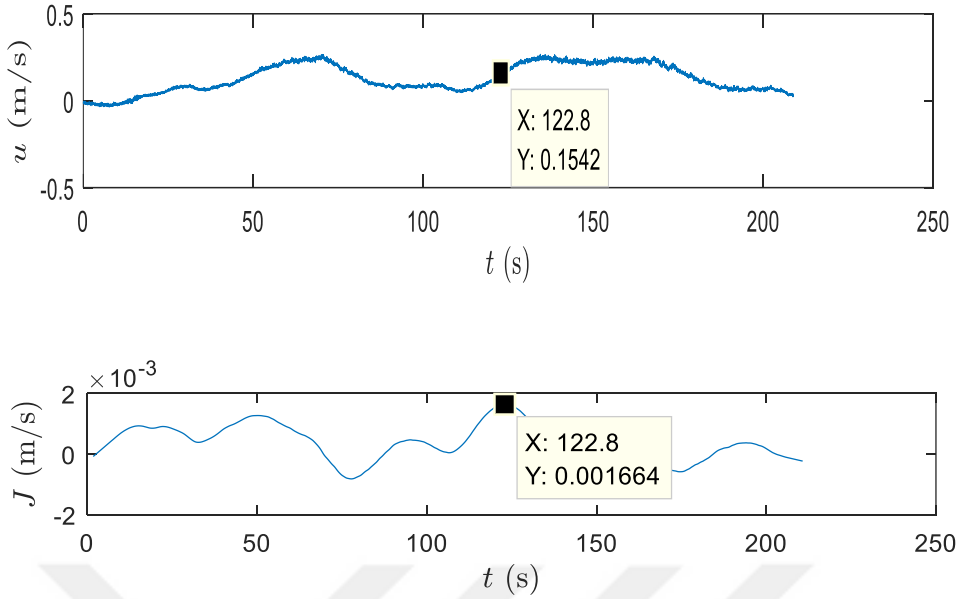

Figure 4.12 : Determining keytime on the hydraulic gradient and on the corresponding hydrograph.

5. DATA ANALYSIS AND RESULTS

5.1 Introduction

In this chapter, the steady and unsteady flow cases passed the circular and elongated piles are described, and the structure of flow downstream of the piles are analyzed. Before the test cases with piles, characteristics of the flow in the no-pile cases are also presented. In the following sections, the influence of pile cross-sectional shape on the flow structure in both steady and unsteady flow cases are demonstrated. Figure 5.1 summarizes different flow cases and pile types investigated in this study.

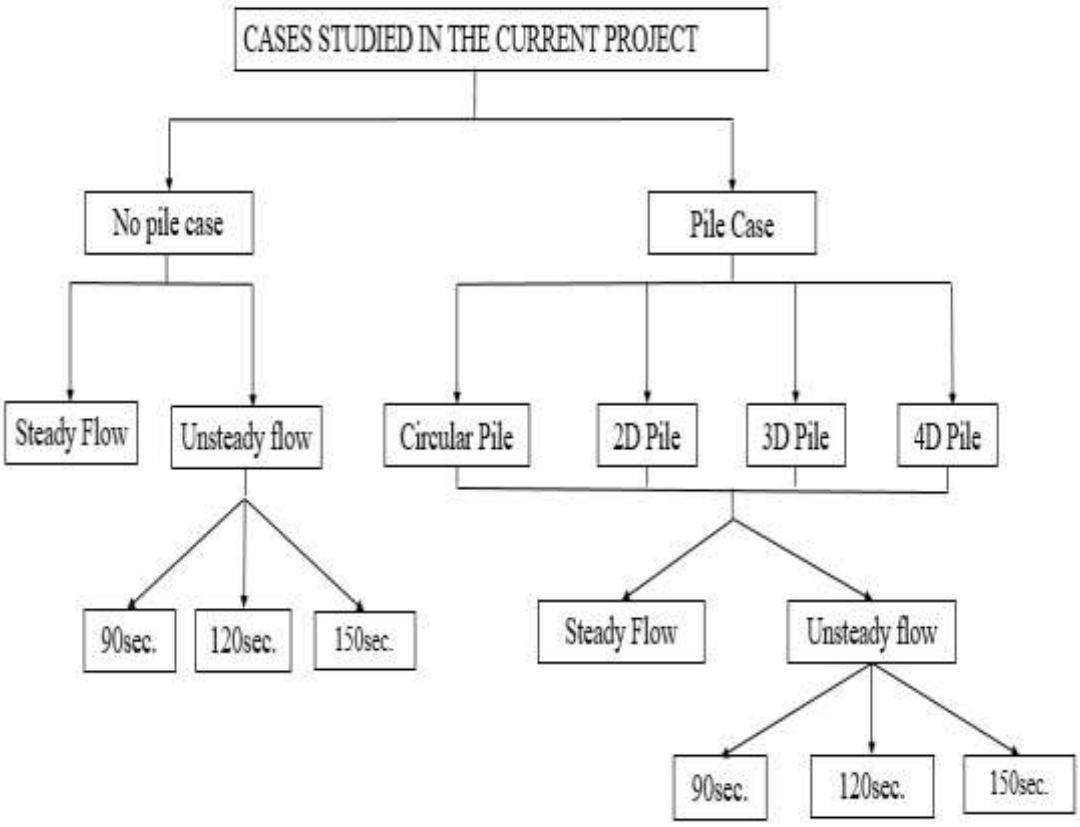

Figure 5.1 : Different cases studied in the scope of the current study.

5.2 Results of No-Pile Case in Steady and Unsteady Flow Conditions

5.2.1 No-pile steady flow case

This section presents the steady flow velocity profile, as well as the flow and turbulence characteristics of the flow obtained through the steady flow experiments without a pile.

To obtain velocity profile and other flow characteristics, the measurements were carried out according to the grid shown in Figure 5.1. As seen in this figure the measurement points are closer near the bed where there is a steep change in the velocity, but away from the bed the points get sparser. Twenty points were used to measure the flow and depict the velocity profile in the steady case, starting from the closest point to the bed ($z = 4.8$ cm) and ending at the closest point to the surface elevation, $z = 23$ cm (water depth being h = 30 cm). For steady flow, the sampling duration for each measurement was 90 seconds.

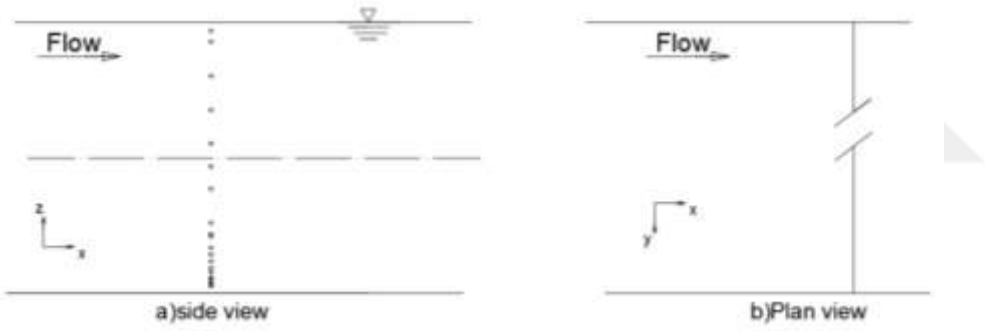

Figure 5.2 : The measurement points in steady flow a) side view, b) plan view.

Figure 5.3 depicts the mean velocity profile $\bar{u}(z)$ in steady flow case, where the vertical axis (z) denotes the distance above the boundary. Near the bed at the boundary due to no-slip condition, the velocity attains to zero as expected. At some distance above the bed, close to the surface, the velocity attains to a constant value, the so-called the free stream velocity. Between the bed and the free stream, the velocity varies over the vertical coordinate. For calculating the mean velocity, Equation 5.1 is used. Here $\bar{u}$ is the time-averaged velocity in different water depths.

$$\bar{u} = \frac{1}{T}\int_{t}^{t+T} u(t)dt \qquad (5.1)$$

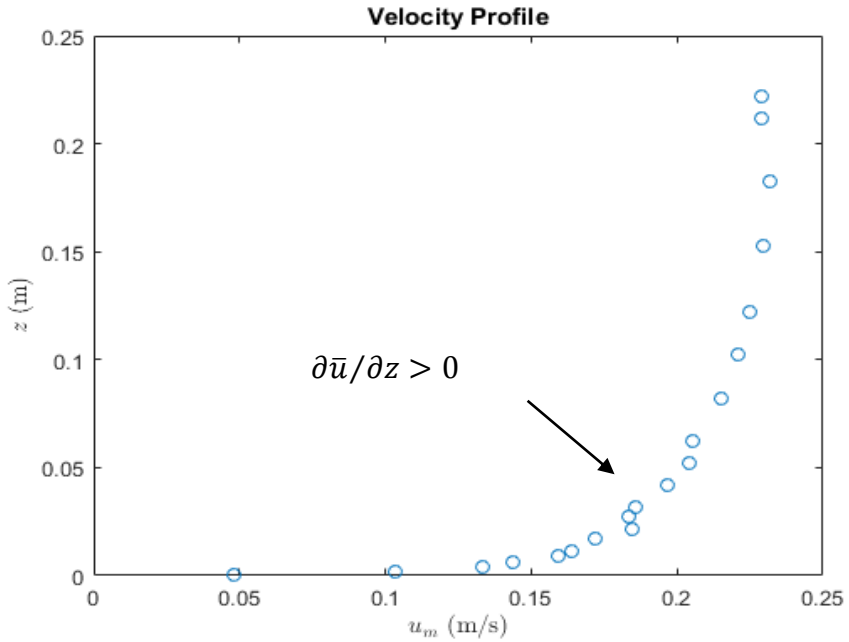

Figure 5.3: Velocity profile in no pile case steady flow.

For turbulent flow, the Reynolds decomposition for the longitudinal direction will be as equation 5.2:

$$u' = u(t) - \bar{u} \tag{5.2}$$

In which u' is fluctuating velocity in streamwise (x) direction. Similar definitions apply to lateral v' and vertical w' velocities as well. As the fluctuating velocity gets larger, the flow is more turbulent. Alternately, for defining the strength of the turbulent flow the following turbulent quantities are defined:

$$u_{rms} = \sqrt{\overline{u'^2}(t)}\,, \quad v_{rms} = \sqrt{\overline{v'^2}(t)}\,, \quad w_{rms} = \sqrt{\overline{w'^2}(t)} \tag{5.3}$$

u_{rms} is the standard deviation of random velocity fluctuations $u'(t)$. A larger u_{rms} indicates a higher-level turbulence. The variations of turbulence quantities with depth are presented in Figure 5.6.

Boundary layer turbulence is essentially an instability generated by the bed shear stress. The stronger the shear is, the stronger the turbulence will be. The shear in the boundary layer decreases moving away from the bed, $\partial(\partial\bar{u}/\partial y)/\partial y < 0$, and as a result the turbulence intensity decreases, as expected. Shear velocity is a parameter in velocity scale that represents shear stress, $U_f = \sqrt{\tau/\rho}$. In order to determine the shear

velocity different methods have been used in the literature. These methods are presented in Table 5.1.

Table 5.1 : Different methods for estimating friction velocity in the literature.

Method	Source
Clauser's Method(log-law) $\bar{u} = AU_* \, ln(z) + B$ $z/h < 0.2$	Bombar (2016), Afzalimehr and Anctil (1999), Graf and Song (1995), Song and Graf (1996)
Parabolic Law $\frac{U}{U_{max}} = -\frac{\lambda U_f}{U_{max}}\left(1 - \frac{z}{h}\right)^2 + 1$ $z/h < 0.2$	Bombar (2016), Afzalimehr and Anctil (1999)
Velocity defect law $\bar{u} - V = AU_f(ln\left(\frac{z}{h}\right) + 1$	Bombar (2016)
Momentum Method $U_f = \sqrt{gR_h \, S}$	Bombar (2016) Nezu et al. (1997)
Average Velocity Method $\frac{V}{U_f} = Aln\left(\frac{R_h}{ks}\right) + 6.25$	Bombar (2016)
St. Venant $U_f = \sqrt{gR(-\frac{\partial z}{\partial x} - \frac{1}{g}\frac{\partial V}{\partial t} - \frac{V}{g}\frac{\partial V}{\partial x} - \frac{\partial h}{\partial x})}$	Bombar (2016), Afzalimehr (1999)

Two different methods, which are commonly used in the literature, are applied in the current study:

The first method is the Clauser's method which is basically fitting a log-relation to the velocity profile (log-law) in the inner region. For this matter, the following calculations are done.

$$\bar{u}(z) = AU_f \log(z) + B \tag{5.4}$$

In this equation A is a universal constant, with a constant value of $A = 2.5$, independent of the wall category (smooth, rough, transition). Constant A is also written in the literature in the form of $A = 1/\kappa$, in which κ is called the Van-Karman constant, $\kappa = 0.4$. B is another constant with the value $B = 5.1$ for the hydraulically-smooth wall. By using the equation in the inner region (where $/h < (0.2 - 0.3)$) the shear velocity is obtained. Fitting the line for time averaged velocity points ($\bar{u}(z)$) and $ln(z)$ (figure 5.4), and finding the slope of the line gives us the shear velocity as $U_f =$ 0.0097 m/s.

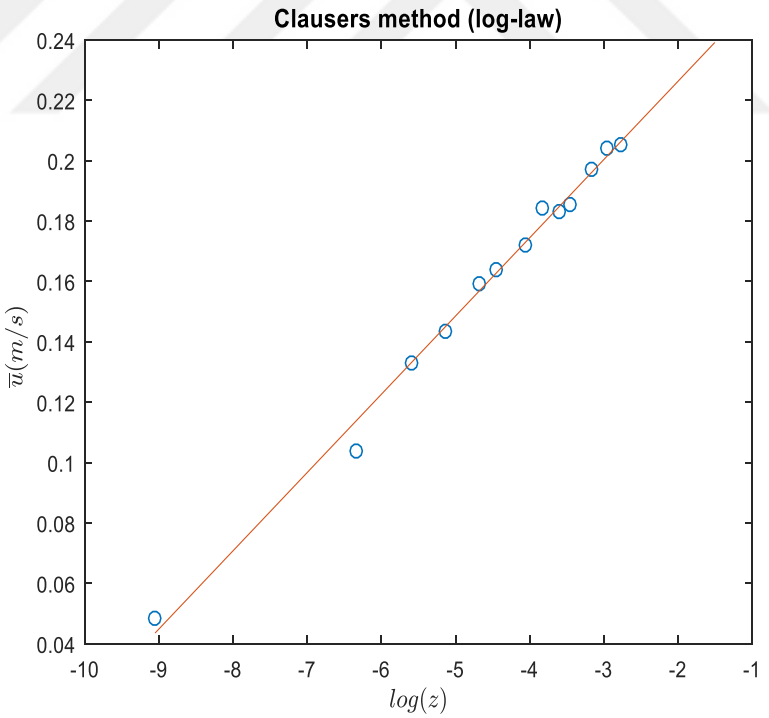

Figure 5.4 : Calculating shear velocity using the Clauser's method.

The second method used for estimation of the shear velocity was based on the calculation of Reynolds shear stress for different z values, and evaluating the profile. Equation 5.5 represents the relation of Reynolds stress obtained from the streamwise momentum equation.

$$-\rho u'w' + \rho\nu\frac{\partial u}{\partial z} = \rho u_f^2(1 - \frac{z}{h}) \tag{5.5}$$

In this method, the points close to the bed are used, in which the turbulent shear stress ($-\rho u'w'$) is very small, and we can ignore that. Besides z/h is very small close to the bed, meaning the that the shear stress can be taken almost equal to the bed shear stress value. Therefore, in this method, we calculate shear velocity by finding the velocity gradient ($\partial u/\partial z$) for points close to the bed. Here the second-order approximation is used for calculating the velocity gradient (Equation 5.6).

$$\frac{\partial u}{\partial z} = \frac{u_{n+1} - u_n}{z_{n+1} - z_n} \tag{5.6}$$

In this equation, n corresponds to the measuring point from the bed. By using $n = 2$ (the second point from the bed), the steady case shear velocity is obtained as $U_f = 0.0098$ m/s.

Comparing the results of shear velocity calculated by two methods (Equation 5.4 and 5.5), it is seen that both methods give very close results to each other.

We can use the shear velocity to calculate the bed shear stress by using equation 5.7.

$$\tau_b = \rho U_f^2 \tag{5.7}$$

Here τ_b, is the bed shear stress and is calculated as $\tau_b = 0.0965$ N/m^2. Total shear stress can be obtained from Equation 5.8. The variations of total shear stress with distance from the bed is depicted in Figure 5.5.

$$\tau = -\rho\overline{u'w'} + \mu\frac{\partial \bar{u}}{\partial z} \tag{5.8}$$

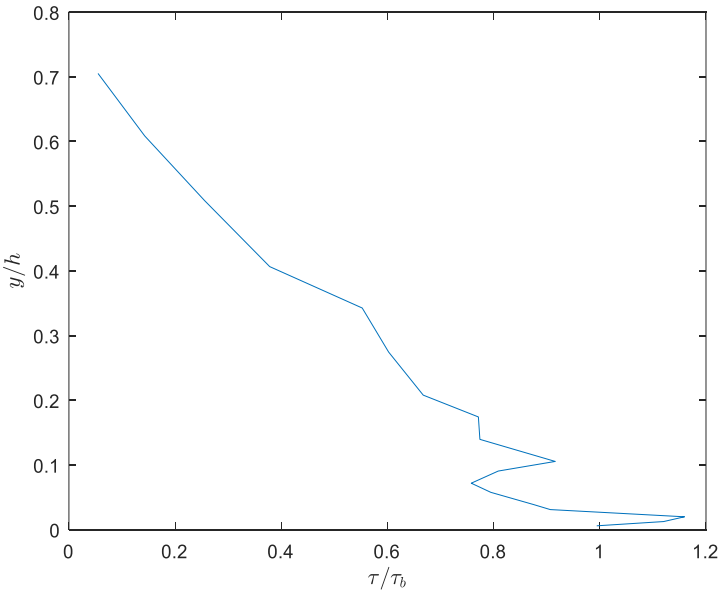

Figure 5.5 : Total shear stress variation with respect to distance from the bed in the no-pile case steady flow.

The turbulence intensity is one of the important characteristics of flow being defined in three dimensions in equation 5.3. Turbulence quantities are presented in a non-dimensional form by use of shear velocity and the variations of them with respect to distance to bed are depicted in Figure 5.6a. In these figures $y^+$is normalized depth called wall unit, and it is calculated as $y^+ = \frac{yU_f}{\nu}$. In which ν is kinematic viscosity and U_f is the shear velocity. The results in Figure 5.6 matches well with the results taken from Monin and ÎAglom (1971) presented in Sumer (2014).

Turbulence Kinetic Energy (K) is another parameter that determines turbulence strength (Equation 5.9).

$$k = \frac{1}{2}(\overline{u'^2} + \overline{v'^2} + \overline{w'^2}) \qquad (5.9)$$

The variations of normalized k (k/U_f^2) and normalized turbulent shear stress $(-\overline{u'w'}/U_f^2)$ with y^+ are presented in Figure 5.6b. The experimental results of turbulence quantities are in line with previous studies (see for example, Nezu and Nakagawa (1995).

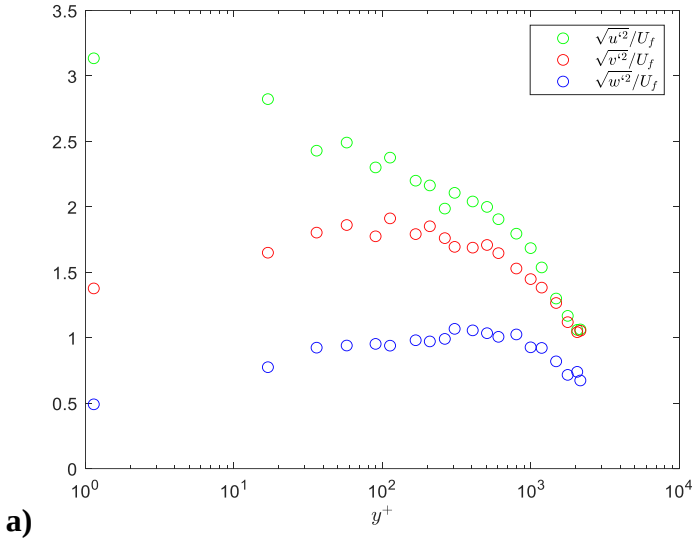

a)

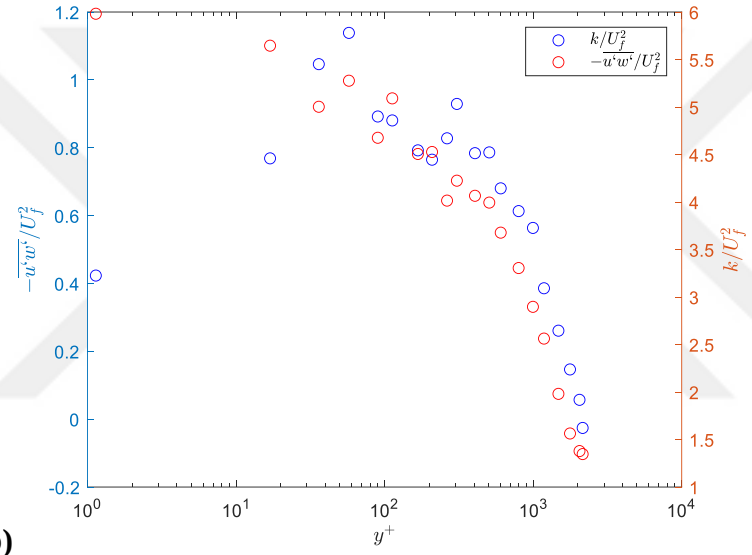

b)

Figure 5.6 : Dimensionless distributions of turbulence intensities with respect to water depth no-pile steady flow case. a) Normalized RMS values of velocity fluctuations, b) normalized k and turbulent shear stress.

5.2.2 No-pile unsteady flow case

Variations of flow characteristics in unsteady flows in the absence of a pile are presented in this section. As explained above, three different hydrographs with different unsteadiness degrees are used in the experiments. As seen in Table 4.3 the unsteadiness degree in the tests was in the range of $6 \times 10^3 < \Upsilon < 7.5 \times 10^3$. Other flow characteristics are also presented in this table. As seen in Table 4.3, the unsteady flow cases started with an initial velocity (V_{min}) then accelerated to a peak velocity (V_{max}), and then decelerated back to the initial velocity. The three unsteady flow cases

(labeled as U1, U2, and U3) have different durations for the hydrograph (Δt), by which their unsteadiness degree is controlled.

Figure 5.7 shows an example of the variations of different velocity values with time for the U3 flow case. In this figure second and third panes show examples of turbulence decomposition performed by S-G method on streamwise instantaneous velocity component $u(t)$ under the U3 flow condition at two different vertical measurement locations; close to the bed ($z/h = 0.05$), and close to water surface ($z/h = 0.1$).

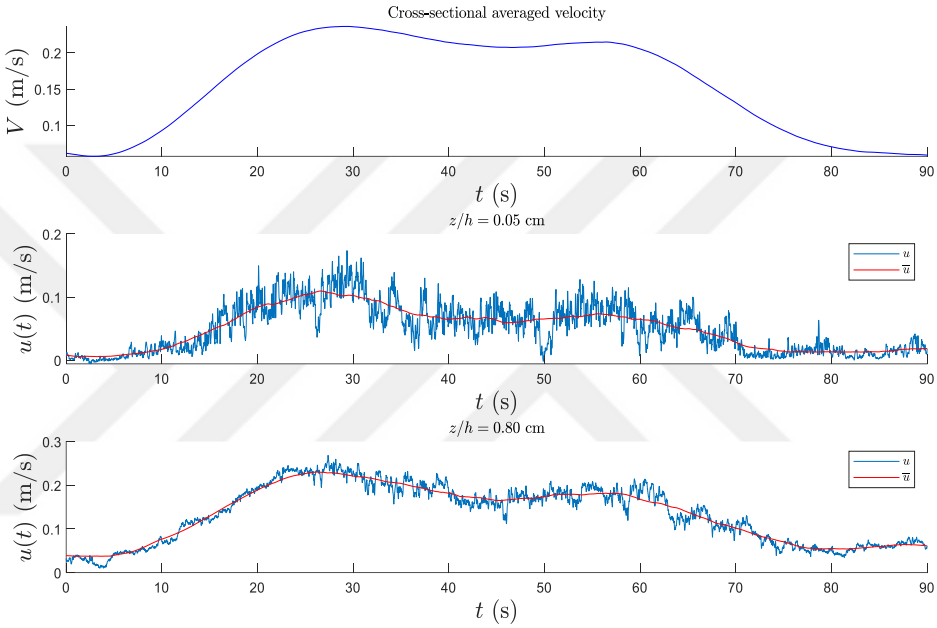

Figure 5.7 : Instantaneous velocity ($u(t)$) and Reynolds-averaged velocity ($\bar{u}(t)$) at two different vertical location form the bed, along with the cross-sectionally averaged velocity, V, for the U1 flow case.

From the instantaneous velocity profile data measured by the ADV instrument for twenty identical runs (for each hydrograph), cross-sectional averaged velocity is obtained as defined in Equation 5.10, and its variations with time for every three unsteady case (U1, U2, and U3) is presented in Figure 5.10.

$$V(t) = \frac{1}{h}\int_0^h \bar{u}(t,z)dz \tag{5.10}$$

Here t is time, z is distance from the bed, and $\bar{u}(t,z)$ is Reynolds-averaged streamwise velocity component.

Figure 5.8 shows the cross-sectional average velocity time series of the three tested unsteady flow cases, U1, U2, and U3. In this figure, it is shown that the hydrographs start from the approximately equal base flow velocity, and according to the arrangements defined for rising time for each unsteady flow case, they attain to their peak velocity values in different times (45 s, 60 s and 75 s). As seen in this figure, the transition from base flow to the peak is more gradual in the single-peaked U1 case, whereas in U2 and U3 cases the acceleration part of the hydrograph occurs with more disturbance and velocity changes non-linearly to the peak.

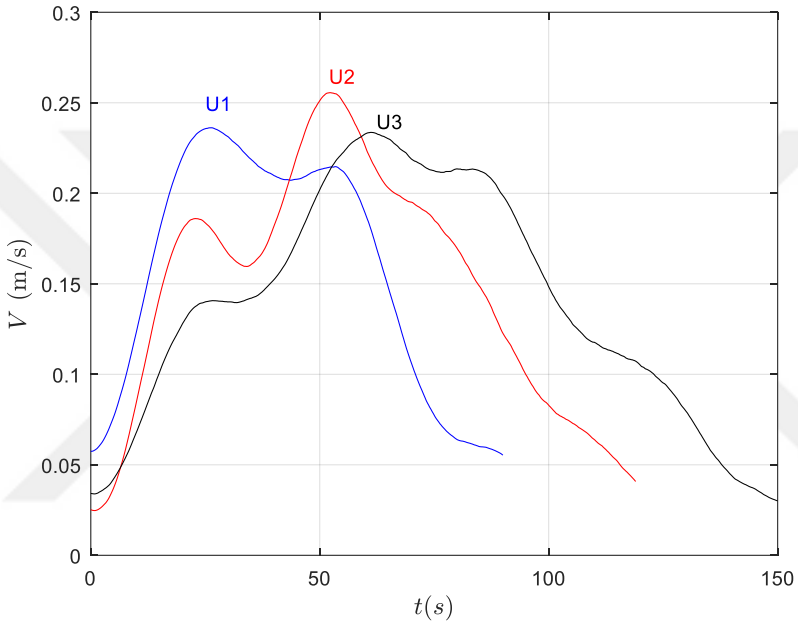

Figure 5.8 : Cross-sectional averaged velocity variations against time in U1, U2 and U3 flow cases used in the experiments.

Figures 5.9 to 5.11 present the profiles of $\bar{u}, \overline{u'w'}$ and k for different time instances for the U1, U2 and U3 flow conditions. These time instances, labelled successively with capital letters from A to G, are chosen such that the couples A-G and B-F correspond to the same cross-sectional average velocity values, namely $V = 0.1$ m/s and $V = 0.15$ m/s, respectively, whereas times C, D and E correspond to instants of local maxima. As mentioned above, among the three unsteady flow conditions, U2 has a significant bi-modal character.

The second pane in Figures 5.9-5.11 shows the mean velocity profile in the determined time instances. The logarithmic variation of the flow velocity close to the bed in these

figures is obvious. It is also clear that velocity ($\bar{u}$) increases until the peak is reached, and then decreases during the falling wing of the hydrograph. There are distinct differences between the acceleration and deceleration stages of the flow given that for the same cross-sectional average velocity, $\bar{u}$ and k, has higher values on the falling wing of the hydrograph comparted to the rising wing. Turbulence kinetic energy variations across the depth in different time instances are shown on the third pane in Figures 5.9-5.11. As seen, k is minimum close to the water surface (away from the bed), and it gets to its maximum close to the bed. During the acceleration part of the hydrograph, near-bed k increases as the flow reaches to its peak, such that in point C (peak point of the hydrograph) the turbulence kinetic energy close to the bed is the highest, while it decreases with the decelerating the flow. Here we can also see that k in falling wing of the hydrograph is higher than its counterpart at the rising wing of the hydrograph (i.e. A-G and B-F).

In U1 case, the boundary layer thickness at the peak instant, C, is around $\delta = 8$ cm, whereas this value becomes 10 cm in the U3 case. This is not surprising, given that unsteadiness is decreased, and the flow becomes better developed.

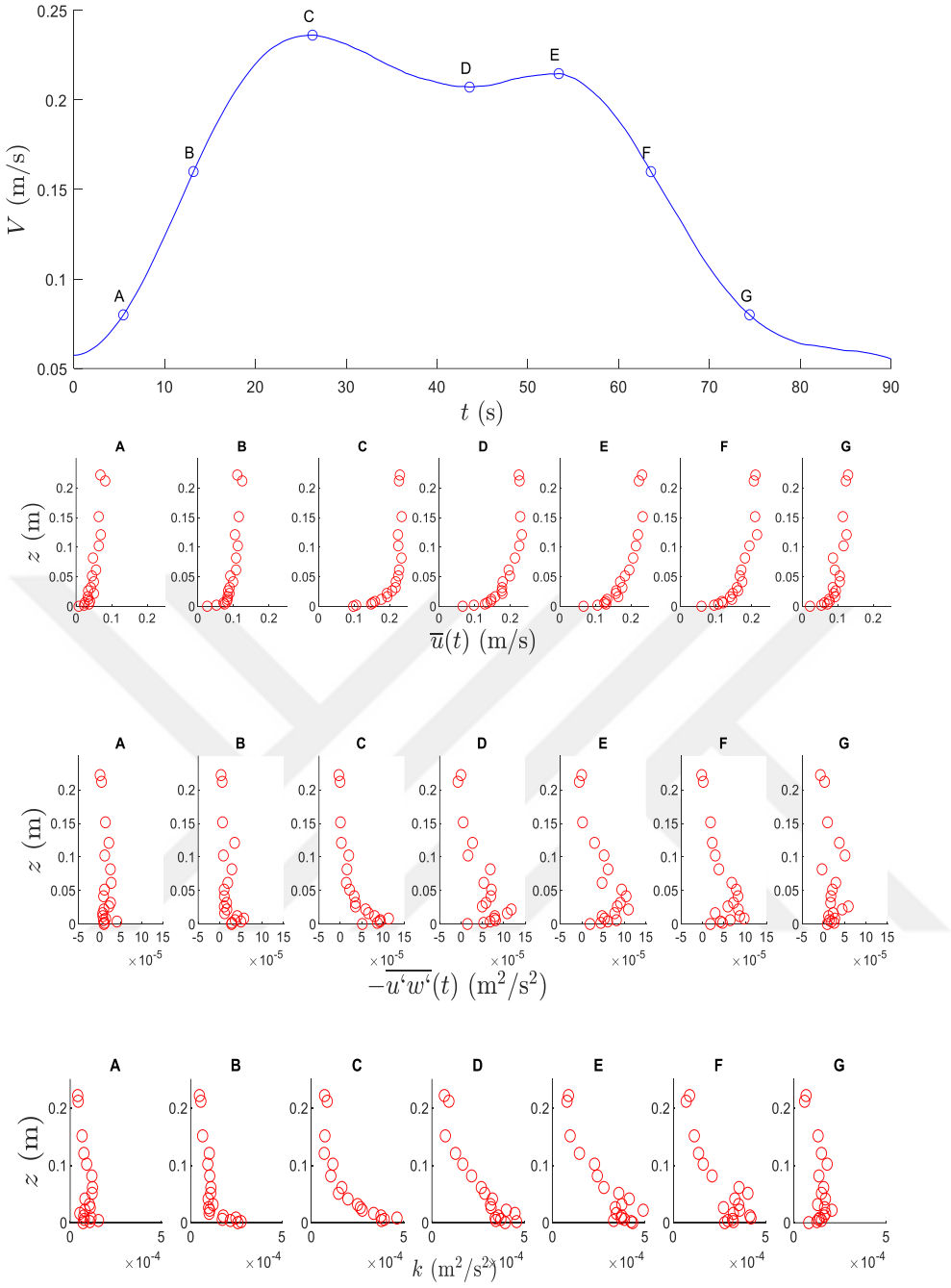

Figure 5.9 : Results of no-pile tests for U1 flow condition. Profiles $\bar{u}, \overline{u'w'}$ and k for different times labeled as A, B, C, D, E, F and G. Top panel shows the cross-sectional average velocity.

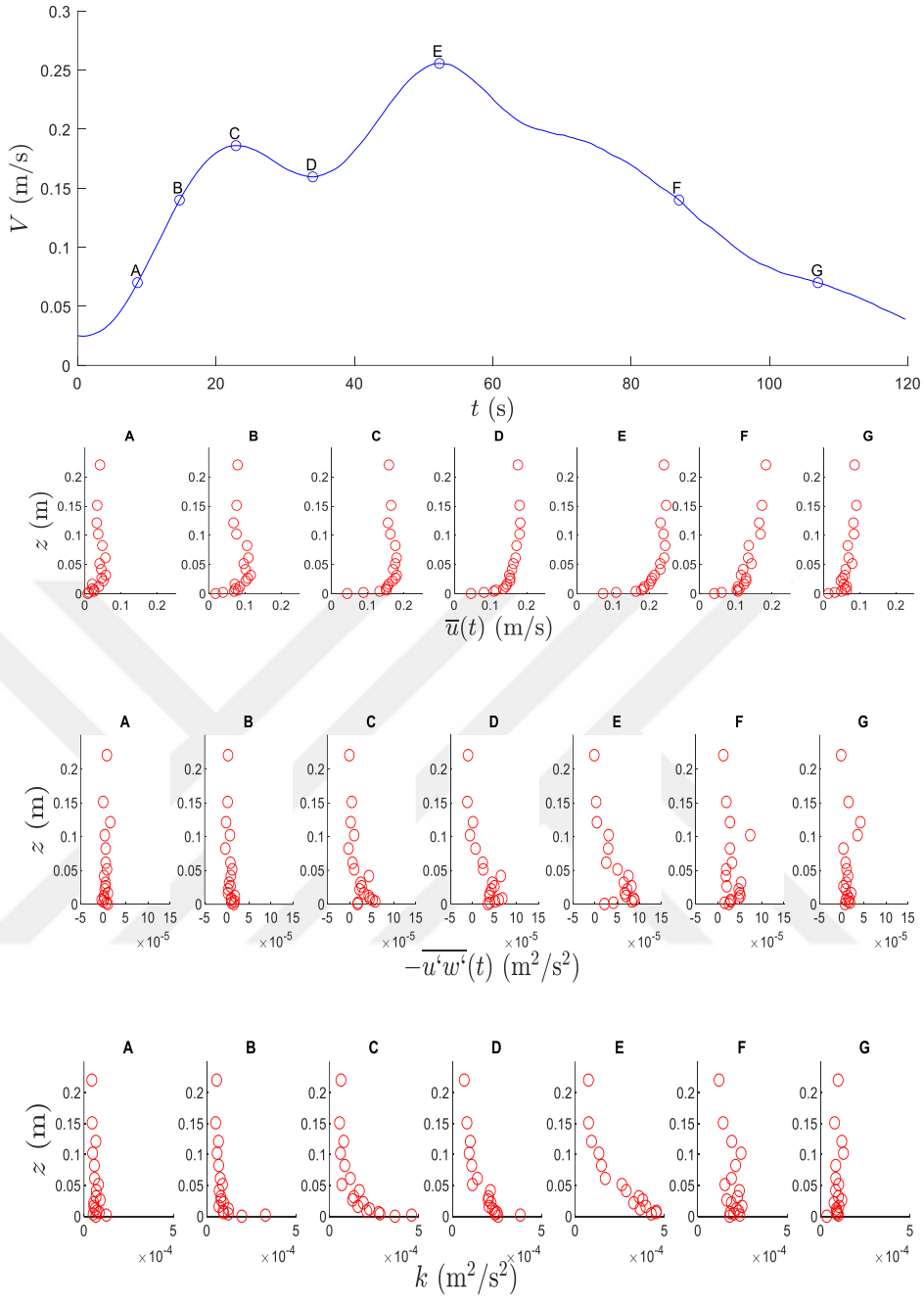

Figure 5.10 : Results of no-pile tests for U2 flow condition. Profiles $\bar{u}, \overline{u'w'}$ and k for different times labeled as A, B, C, D, E, F and G. Top panel shows the cross-sectional average velocity.

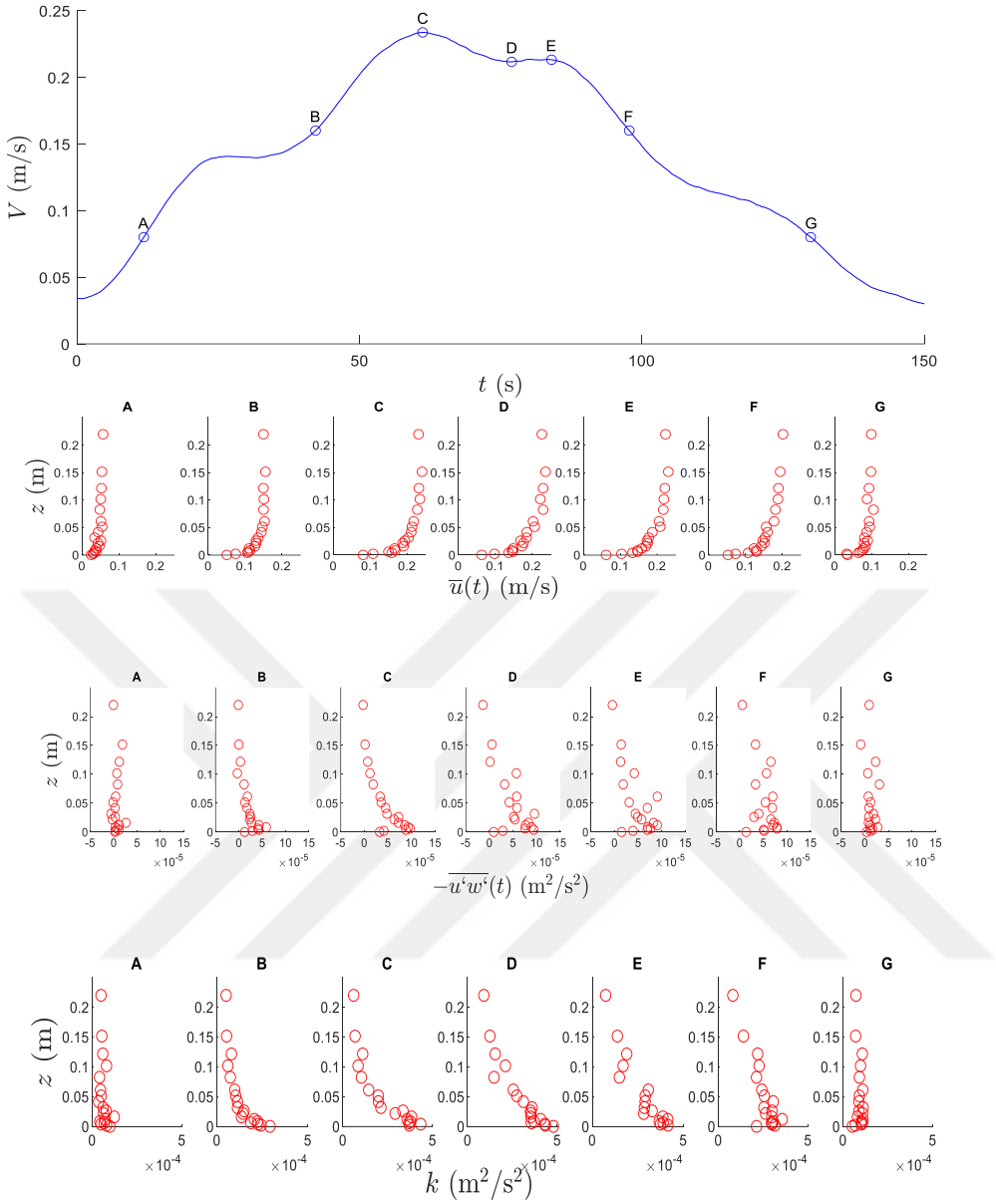

Figure 5.11 : Results of no-pile tests for U3 flow condition. Profiles $\bar{u}, \overline{u'w'}$ and k for different times labeled as A, B, C, D, E, F and G. Top panel shows the cross-sectional average velocity.

Figure 5.12 shows the shear velocity variations with depth averaged velocity, illustrating three different hysteresis loops formed during the accelerating and decelerating ranges of the three hydrographs tested (U1, U2 and U3). The figure shows that during the acceleration stage velocity increases up to $V_{max} = 0.22$ m/s, and then starts to decelerate, the area inside the loop formed by U1 is larger than the other two hydrographs. This loop gets smaller in U3 (as the unsteadiness decreases) but hydrograph U2 behaves differently, it has a smaller loop according to both U1 and U2.

It is clear from the figure that for the same velocity values, shear velocity is higher in the deceleration stage. The hydrograph with the highest unsteadiness (U1) has the highest maximum value for the shear velocity. Nevertheless, U2 behaves differently due to its distinct bi-modal character.

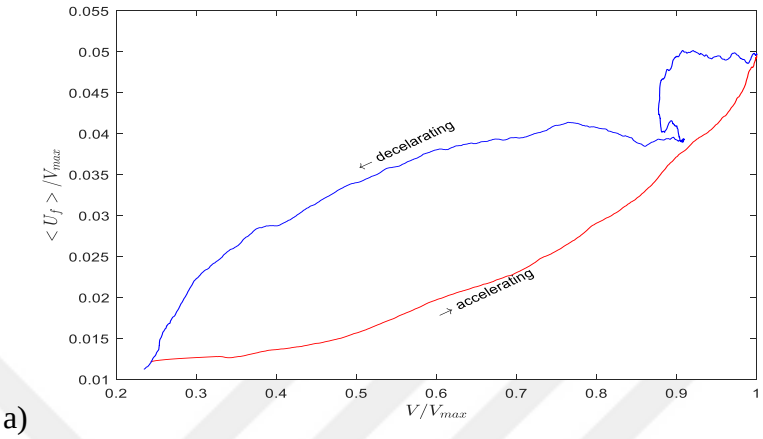

a)

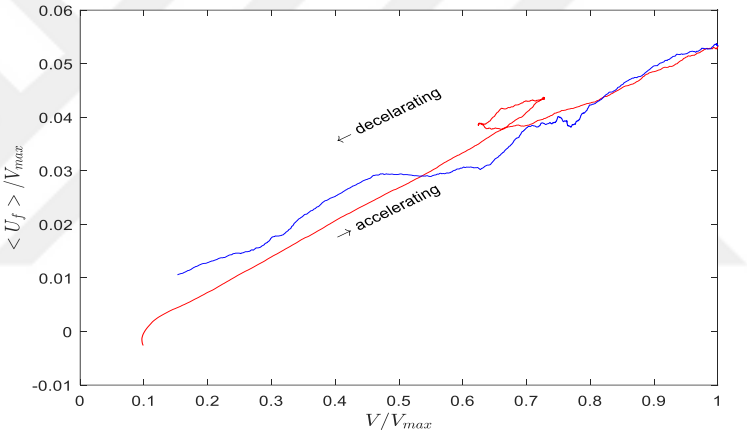

b)

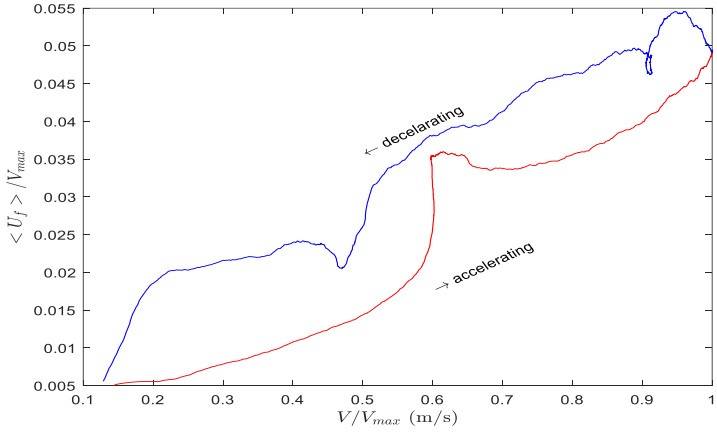

c)

Figure 5.12 : Variation of $< U_f > /V_{max}$ as function of V/V_{max} in no-pile tests. a) U1 case, and b) U2 case, c) U3 case. Red curves represent before the peak (accelerating wing) and blue curves represent after the peak (decelerating wing).

Figures 5.13 and 5.14 show the variation of turbulence quantities (k and $\sqrt{\overline{v'^2}}/V_{max}$) with respect to depth-average velocity (V). Figure 5.13 shows that k at instant F is almost three times larger than that in instant B, both instants having the same velocity. Comparing instants B and F in Figure 5.14, $\sqrt{\overline{v'^2}}$ at instant F is around 50% larger than that in instant B. This is a very significant feature of the tested unsteady flow conditions from flow-seabed-structure interaction point of view. It is also important to remember that in the current experiments the flow depth is kept constant. Thus, the source of hysteresis in turbulence is not the changing flow depth but it is the accelerating and decelerating flow. The bi-modal character of U2 flow case is also distinguishable from both Figures 5.13 and 5.14. Nevertheless, in U2 case depth-averaged turbulence quantities (both k and $\sqrt{\overline{v'^2}}/V_{max}$) keep increasing even after the first peak is reached, yielding a single major hysteresis loop, similar to the other two tested flow cases.

To wrap up, the counter-clockwise loops in figures 5.13 to 5.14 clearly show that there is a strong hysteresis between the incident velocity of flow and turbulence characteristics in the cases of unsteady flows. It is seen from the findings that the maximum depth-averaged lateral turbulence velocity (Figure 5.14) and turbulence kinetic energy (Figures 5.15) during the unsteady flow is attained much later than the peak instant of V. Results of streamwise and vertical fluctuating components ($\sqrt{\overline{u'^2}}$ and $\sqrt{\overline{w'^2}}$) which are qualitatively similar to the k and lateral fluctuating velocity plots shown in Figures 5.13 and 5.14.

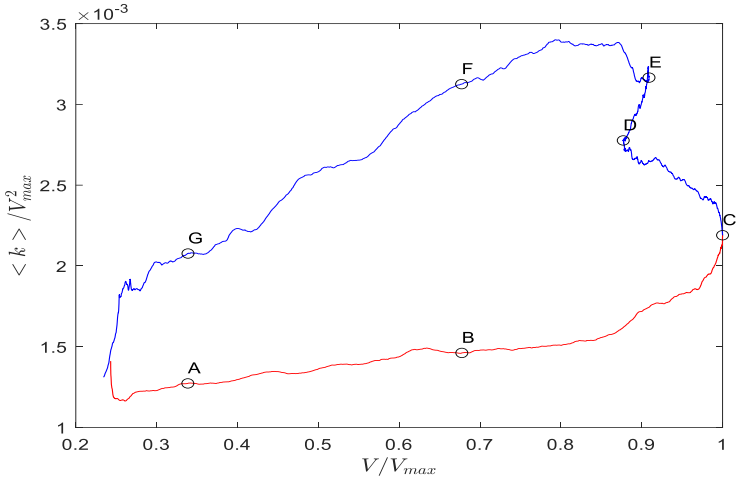

a)

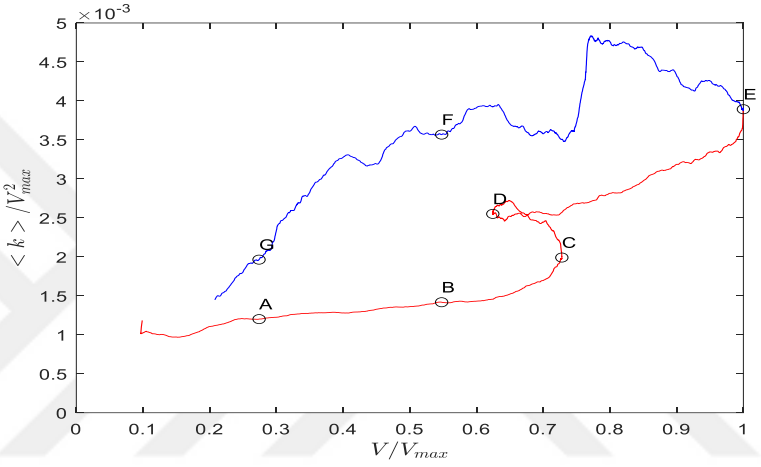

b)

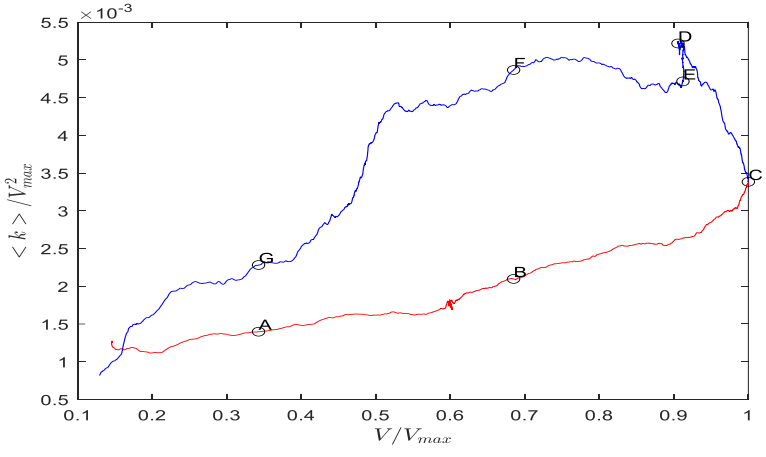

c)

Figure 5.13 : Variation of $< k > /V_{max}^2$ as function of V/V_{max} in no-pile tests. a) U1 case, and b) U2 case, c) U3 case. Red curves represent before the peak (accelerating wing) and blue curves represent after the peak (decelerating wing).

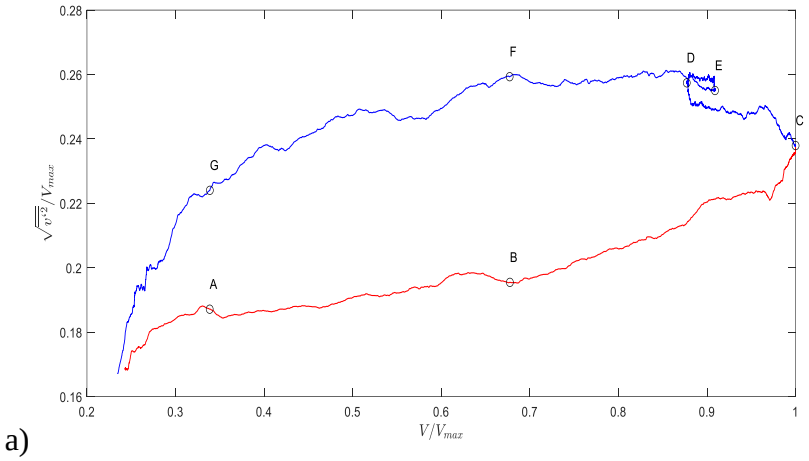

a)

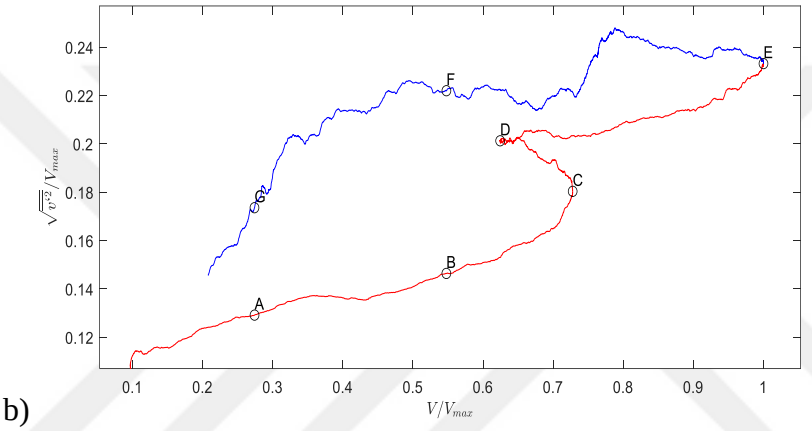

b)

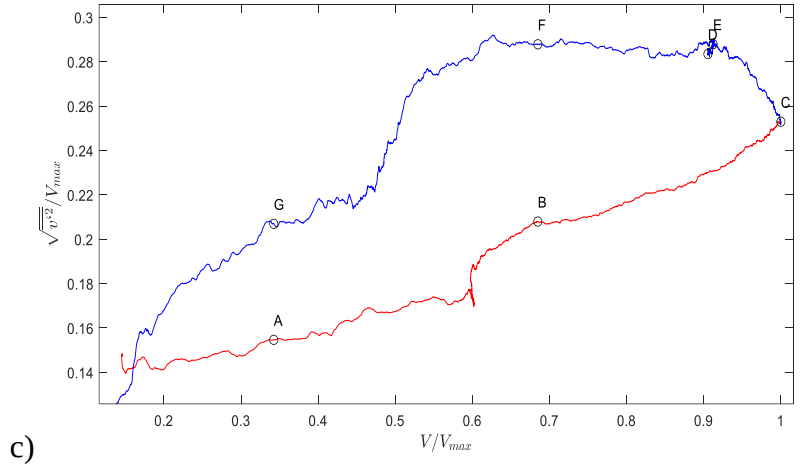

c)

Figure 5.14 : Variation of $< \sqrt{\overline{v'^2}} > / V_{max}$ as function of V/V_{max} in no-pile tests. a) U1 case, and b) U2 case, c) U3 case. Red curves represent before the peak (accelerating wing) and blue curves represent after the peak (decelerating wing).

5.3 Experimental Results for Circular Pile

In the experiments conducted with piles, the pile is placed in the middle of the flume, and instantaneous flow velocities across both vertical and horizontal planes are measured with ADV, as explained in chapter 4. Water levels are also measured using water level probes installed upstream and downstream of the pile (the pile is placed in the middle of the probes). This section presents the results of the flow pattern around the circular pile for both steady and unsteady cases.

5.3.1 Circular pile steady flow results

The results of steady flow (flow condition S) interacting with the pile model will be discussed here as a reference case. Figure 5.15 presents the Reynolds-averaged velocity vectors around the pile in steady flow together with the spatial variation of $\bar{u}$. The flow contours are presented in both horizontal $(x - y)$ and vertical $(x - z)$ planes. The flow features can clearly be seen in this figure: In the $(x - y)$ plane, in the region between the pile and the wall, the flow streamlines get contracted and the velocity reaches to its maximum value. In the immediate downstream of the pile, the velocity has zero or negative values ($\bar{u} \leq 0$), here is the region where the flow is recirculated and it is marked with red contour. In $(x - z)$ plane it is shown that the recirculation region is extended up to 2D. By moving further downwards, it is seen that the flow recovery in the pile wake, i.e. flow restoring its undisturbed state, starts earlier at the near-bed region compared to the upper regions of the flow, where the flow recovery takes a much longer distance. Furthermore, the extent of the recirculation region is considerably narrower at the near bed compared to that of the upper regions.

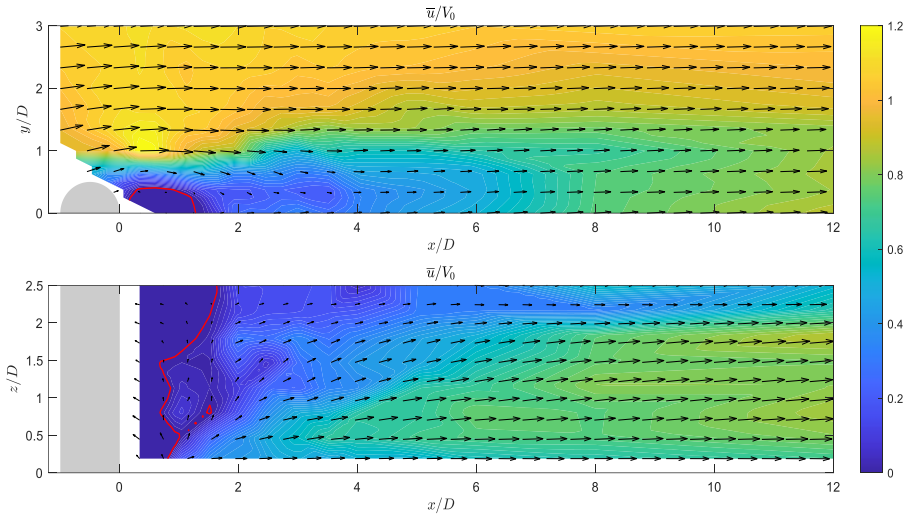

Figure 5.15 : Reynolds-averaged velocity vectors, and contour plot of $\bar{u}/V$ around the circular pile in steady flow case (case S), over the horizontal ($z/D = 1.83$) and vertical ($y/D = 0$) planes respectively. Grey area is the pile and red contour marks $\bar{u} = 0$.

The spatial distribution of lateral fluctuating velocity ($\sqrt{\overline{v'^2}}/V$) in the steady flow case is shown in Figure 5.16. The increased $\sqrt{\overline{v'^2}}$ at the immediate downstream of the pile is associated with the generation of lee-wake vortices (vortex shedding), and it is seen to have particularly large values within a distance of 4D at the wake of the pile. The K distributions at the downstream of the pile has a similar picture with that of $\sqrt{\overline{v'^2}}$ since the greatest contribution to pile-generated turbulence comes from this component. According to Figure 5.17 the increase of the k just behind the pile is clearly the same as that in Figure 5.16.

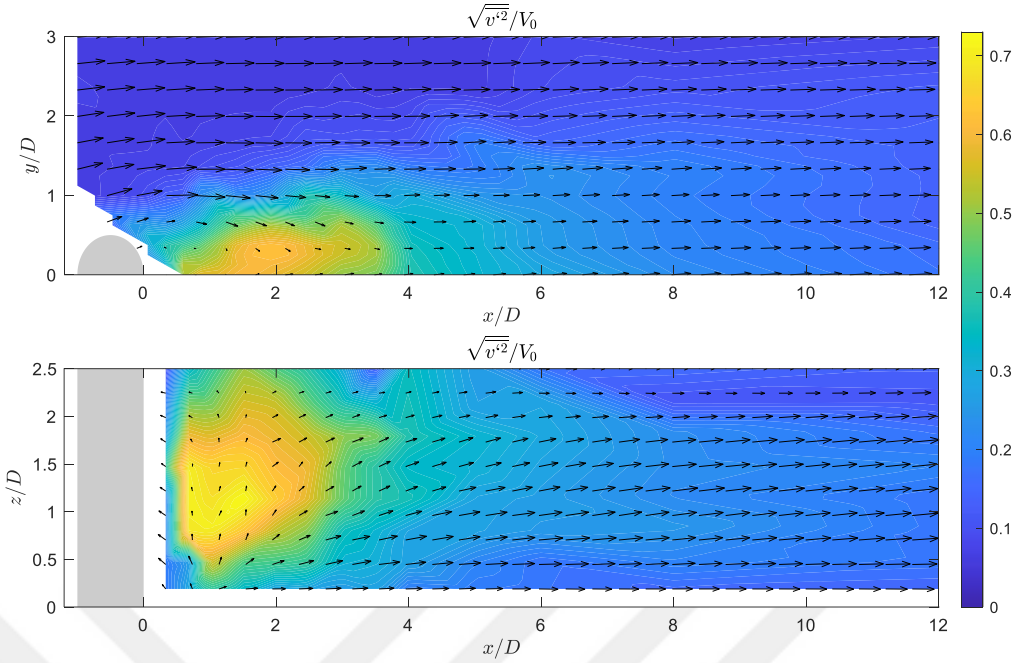

Figure 5.16 : Contour plot of $\sqrt{\overline{v'^2}}/V_0$ around the pile in steady flow case (case S) over the horizontal ($z/D = 1.83$) and vertical ($y/D = 0$) planes respectively. Grey area is pile.

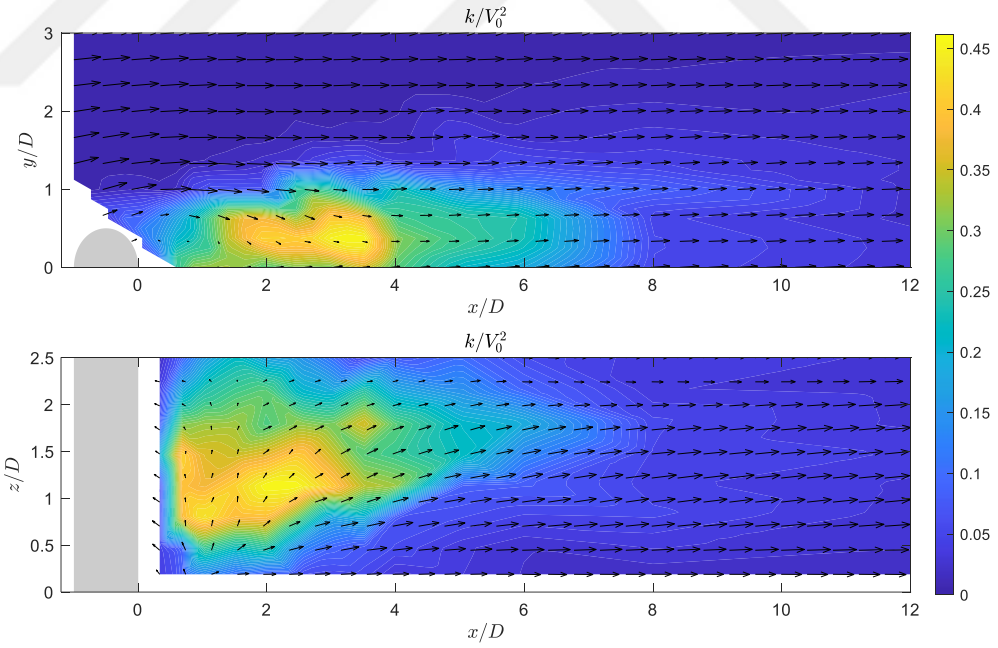

Figure 5.17 : Turbulence Kinetic energy variations (k/V^2) around the circular pile in steady case over the horizontal ($z/D = 1.83$) and vertical ($y/D = 0$) planes respectively. Grey area is pile.

5.3.2 Circular pile unsteady flow results

5.3.2.1 Spatial characteristics of unsteady flow interacting with circular pile

Three different flow unsteady cases were tested (U1, U2 and U3 in Table 4.3). These flows are arranged so that the base and peak velocities are the same for all the three cases, but only the base time is different. As such, these three unsteady flow cases have different unsteadiness coefficients. For the reasons of space organization, only results of U1 and U3 are presented in this section. A complete set of the results are displayed in the Appendix section.

In the case of unsteady flow, Reynolds-averaged velocity around the pile becomes a function of time. In order to compare the unsteady case with the steady flow, characteristics of flow around the pile at the peak time of the undisturbed unsteady flow are studied as representative values.

Figures 5.18 and 5.19 depict the contour plots of the $\bar{u}/V_{max}$ in the case of U1 and U3 at the instants labeled as C and E (corresponding points to peak times of the undisturbed hydrograph, see Figure 5.10 and 5.12).

As seen from the figures, the flow contractions at the sides of the pile are significantly weaker in the U1 case compared to that in steady flow. It is also clear that U3 case has a starker contraction of the streamlines around the pile in comparison with U1 case. Moreover, the recirculation region in the pile wake is broader compared to that in the steady flow case, although according to the figures, the flow characteristics in U3 (which has a smaller unsteadiness degree compared to U1) are closer to that in steady flow case. The recirculation region at instant C, however, is remarkably narrower compared to steady flow case, given that the flow at this time is not sufficiently developed.

Furthermore, in unsteady flow case the flow recovery is seen to be incomplete even in the 12D downstream of the pile, where in steady flow the flow recovers relatively faster.

Figures 5.20 to 5.23 display the spatial distribution of turbulent kinetic energy (k) and lateral turbulence fluctuations in U1 and U3 cases. It is clear that the pile generated turbulence in the case of unsteady flow compared to that in steady flow (Figure 5.17)

is reduced. Observations during the experiments also support this finding, such that vortex shedding in the pile wake was noticeably weaker during the unsteady flow cases. It is also interesting to report that turbulence generated in the pile wake for the case of U1 is somewhat higher than that of U3.

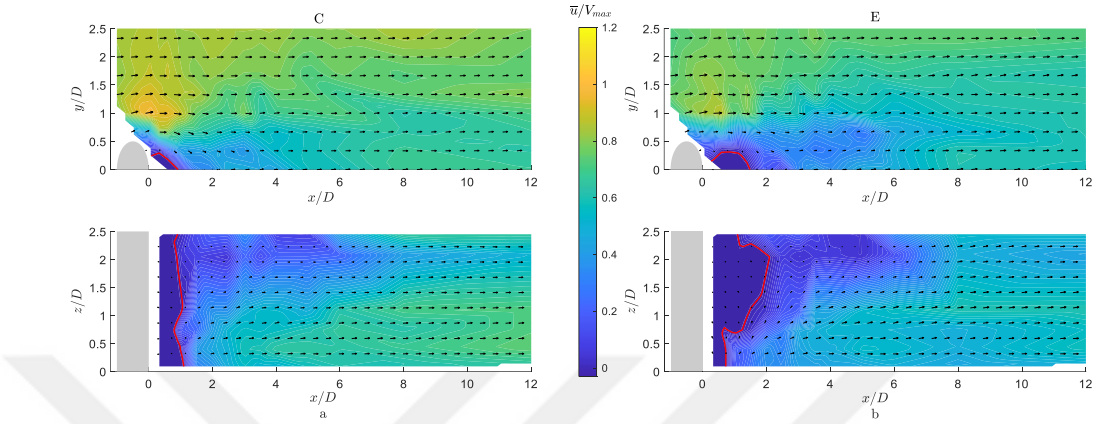

Figure 5.18 : Reynolds-averaged velocity vectors, and contour plot of $\bar{u}/V_{max}$ in unsteady flow case U1 over the horizontal and vertical planes. Left pane: the time labelled C. Right pane: the time labelled E. Grey area is the pile, and the red contour marks $\bar{u} = 0$.

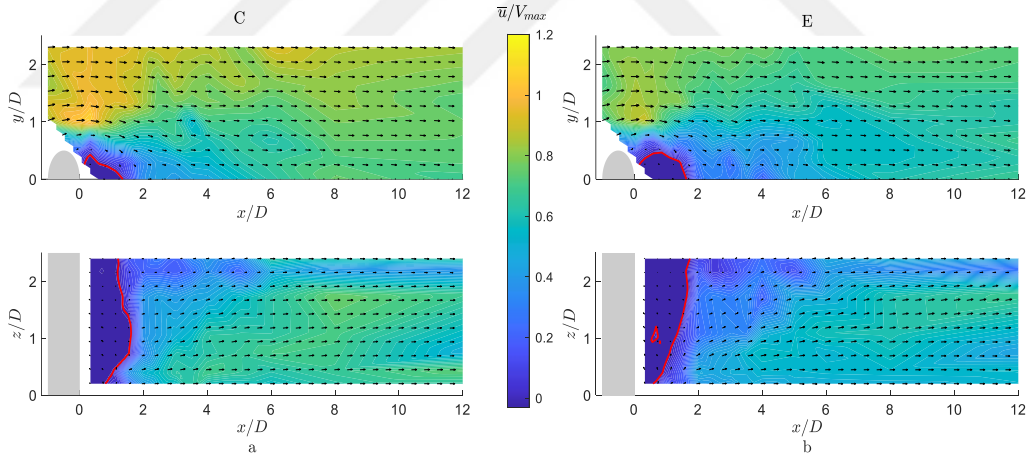

Figure 5.19 : Contour plot of $\bar{u}/V_{max}$ in unsteady flow case U3 over the horizontal and vertical planes. Left pane: the time labeled C. Right pane: the time labeled E. Grey area is the pile, and the red contour marks $\bar{u} = 0$.

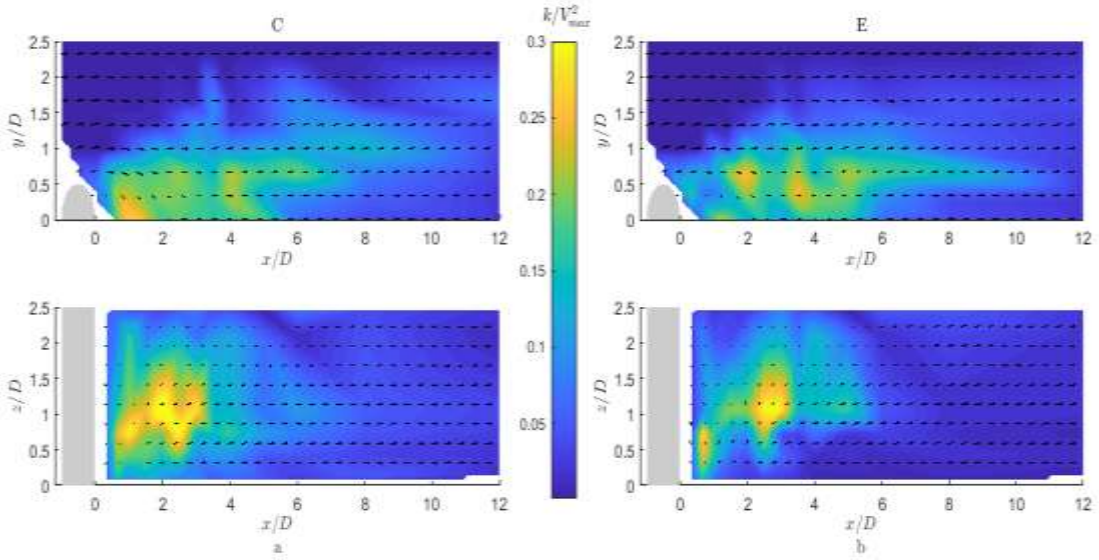

Figure 5.20 : Contour plot of $k/V^2{}_{max}$ in unsteady flow case U1 over the horizontal and vertical planes. Left pane: the time labeled C. Right pane: the time labeled E.

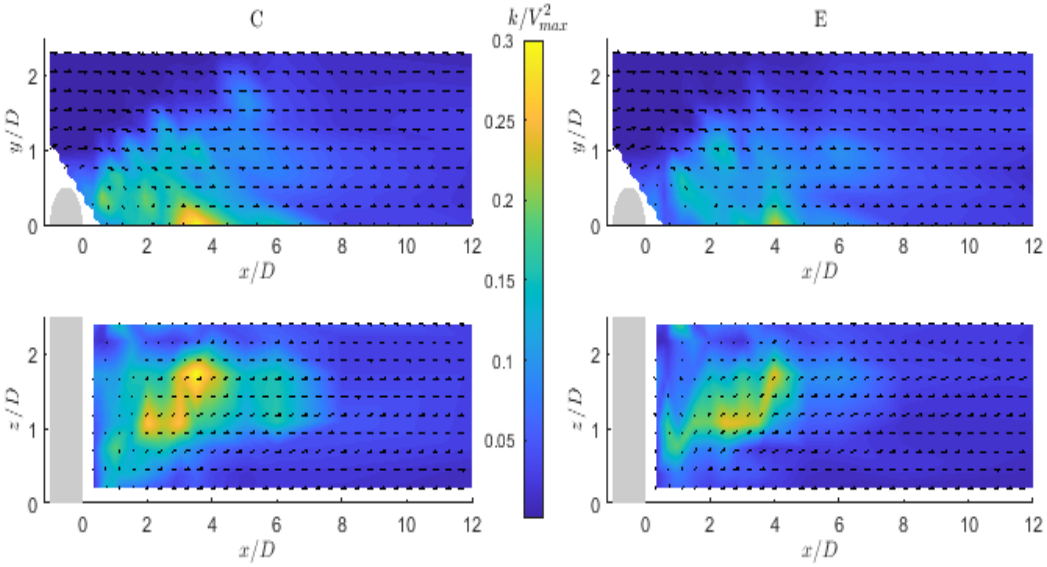

Figure 5.21 : Contour plot of $k/V^2{}_{max}$ in unsteady flow case U3 over the horizontal and vertical planes. Left pane: the time labeled C. Right pane: the time labeled E.

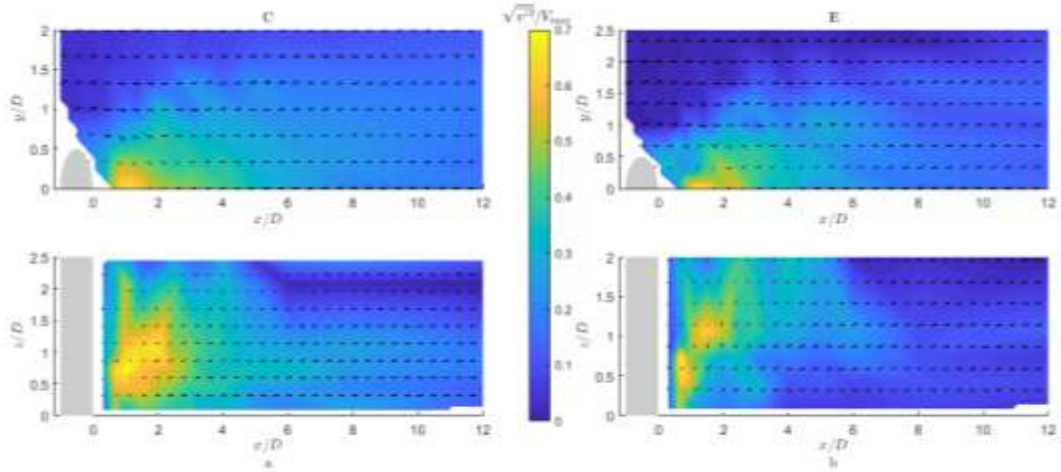

Figure 5.22 : Contour plot of $\sqrt{\overline{v'}^2}/V_{max}$ in unsteady flow case U1 over the horizontal and vertical planes. Left pane: the time labeled C. Right pane: the time labeled E.

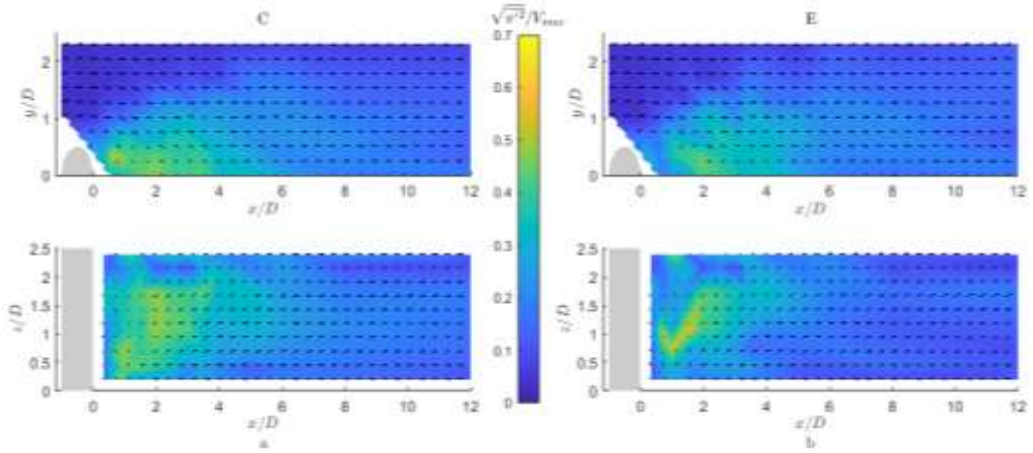

Figure 5.23 : Contour plot of $\sqrt{\overline{v'}^2}/V_{max}$ in unsteady flow case U3 over the horizontal and vertical planes. Left pane: the time labeled C. Right pane: the time labeled E. Grey area is the pile.

5.3.2.2 Turbulence and hysteresis in the wake of the circular pile

The variation of depth-averaged turbulence in the pile wake as a function of flow velocity is plotted for various distances downstream of the pile (x/D) along the centerline of the flume to understand how the hysteresis between flow velocity and turbulence inherent in the undisturbed gradually-varying flow changes with the presence of the pile. The results are shown in Figures 5.24a and 5.24b, respectively for U1 and U3 cases.

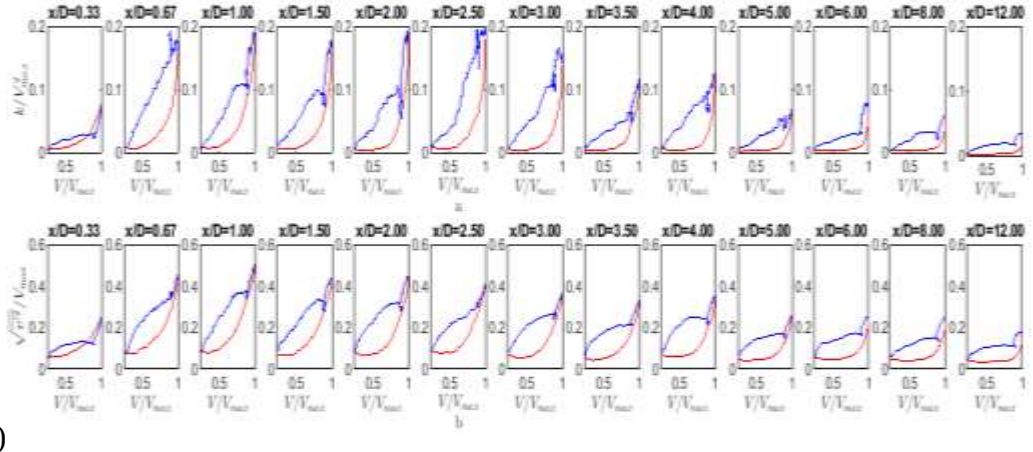

a)

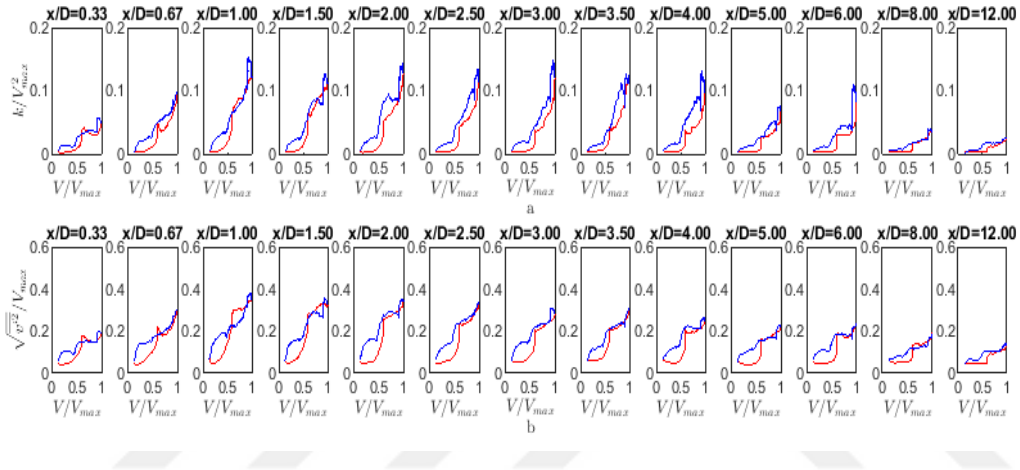

b)

Figure 5.24 : Variation of depth average turbulence as a function of undisturbed flow velocity,V/V_{max} for the a) U1 and b) U3 flow case, $\sqrt{\overline{v'}^2}/\mathrm{V}_{max}$ upper pane and $k/\mathrm{V}^2{}_{max}$ is in the lower pane.

Figure 5.24a shows that, while the presence of the pile reduces hysteresis, there is still a significant hysteresis in the pile wake, with turbulence being larger during the falling stage (blue curve) than during the rising stage (red curve). This was also the case in undisturbed flow. There is however one exception to this behavior. The hysteresis is reversed at the immediate downstream of the pile ($x/D = 0.33$), the first column of the plots given in Figure 5.24, meaning that turbulence is larger during the rising stage. This point incidentally falls in the recirculation region, where the Reynolds-averaged velocity is upstream directed ($\bar{u} \leq 0$). The reverse hysteresis at $x/D = 0.33$, shows that the turbulence generated due to the acceleration of the incident flow is larger than that generated by the fully-developed flow given that the lee-wake vortices do not develop in such close vicinity of the pile. In Figure 5.24, V vs k plots of $0.67 \leq$

$x/D \leq 2.5$ show a very similar variation during the rising stage (red curves), whereas the curves exhibit differences for the falling stage. It is also interesting to note that the peak of the $\sqrt{\overline{v'^2}}$ along the pile wake is attained just before (or almost at) the peak of V, but it is seen that this behavior starts to restore back to the undisturbed case at around $x/D = 12$ (Figure 5.24).

As presented in Figure 5.24b, the hysteresis behavior of the U3 flow case in the wake of the pile is qualitatively similar to that of the U1 case, but the hysteresis is generally less than that in the U1 case. Interestingly a local maximum in both $\sqrt{\overline{v'^2}}$ and k is seen before the peak flow at instant C is attained. This local maximum in turbulence is becoming very pronounced close to the pile ($x/D \leq 0.67$), and it corresponds to a time between instants A and B, at which the incident velocity also has a slight local maximum.

Figure 5.26 presents the comparison of depth-averaged turbulence kinetic energy and lateral turbulence fluctuations in the wake of the pile for steady and unsteady flow cases. For unsteady flow cases the maximum values of $< k >$ and $< \sqrt{\overline{v'}^2} >$, are used instead of the values measured at the peak instant of the incident flow. For both $\sqrt{\overline{v'}^2}/\mathrm{V}_{max}$ and $k/\mathrm{V}^2{}_{max}$ turbulence generated in steady flow case is generally higher than the unsteady cases for $1 \leq x/D \leq 2.5$, as one may expect. As seen in Figure 5.26a, U1 has larger depth-averaged lateral fluctuations compared to U3. A similar finding was reported for the spatial variation of turbulence in the unsteady flow cases around the pile. Further downstream along the pile wake in $x/D \geq 2.5$, the unsteady flow case U1 has larger $\sqrt{\overline{v'}^2}$ values than the steady case, also in this range U3 flow case has almost equal values with the steady flow case.

The depth-averaged turbulence kinetic energy variations given in Figure 5.25b, shows that steady flow has higher turbulence kinetic energy in the wake of the piles for points within the range $0.67 \leq x/D \leq 3.5$. Moving further downstream, this value decreases gradually for $x/D \geq 3.5$, so that the turbulence kinetic energy values in the U3 case attain to almost equal values with the steady flow case. The decrease in K values in the U3 case is not monotonic with the downstream distance, and includes fluctuations.

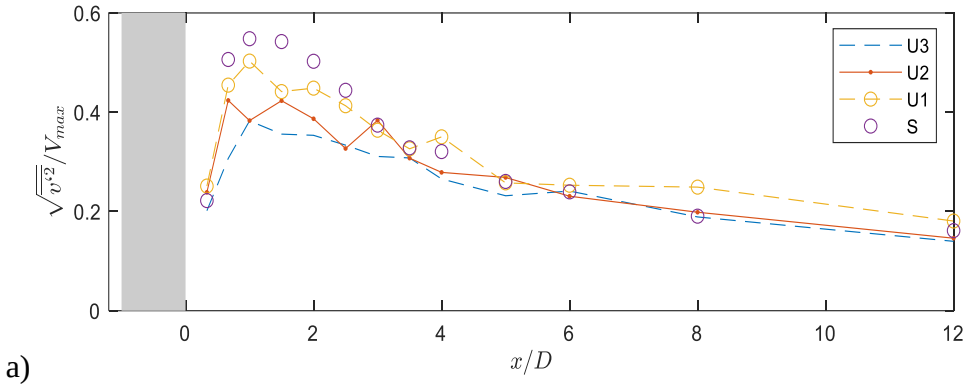

a)

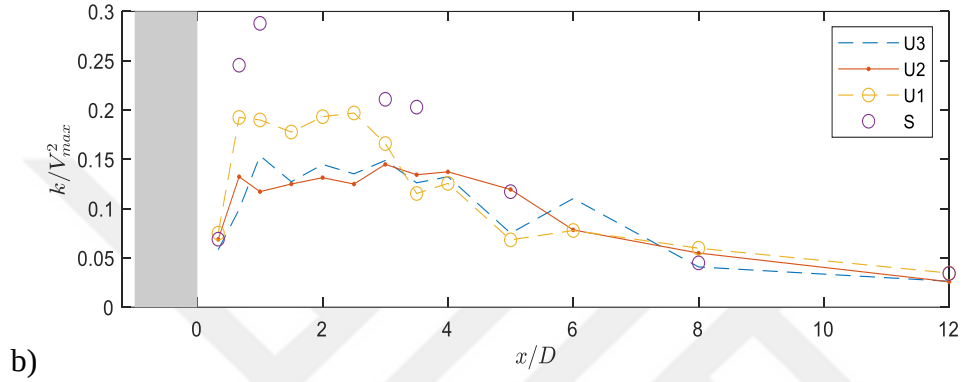

b)

Figure 5.25 : Depth-averaged turbulence quantities as a function of x/D in the wake of the pile a) $< \sqrt{\overline{v'}^2} > /\mathrm{V}_{max}$ and b) $< k > /\mathrm{V}^2{}_{max}$. Steady flow data is also presented for comparison.

5.3.2.3 Flow deficit in the wake of circular pile

The presence of pile in the flow domain causes a strong flow deficit (or velocity deficit) in the lateral direction, such that the velocity in the wake of the pile suddenly drops, whereas the contraction of streamlines at both sides of the pile causes a pronounced increase in the velocity. The flow deficit can be seen in Figure 5.26 for steady and unsteady flow cases. This velocity difference causes shear-induced lateral momentum transfer, which drives sudden variation and instability of flow quantities, including vortex shedding and turbulence production.

In order to quantify the flow deficit along the pile wake, a non-dimensional parameter is defined as $(U_c - U_w)/U_0$. Here U_c and U_w are contraction velocity and wake velocity, respectively, and defined as follows:

$$U_c = \frac{1}{(B/2-D/2)} \int_{D/2}^{B/2} \bar{u}(y)dy \qquad (5.11)$$

$$U_w = \frac{1}{D/2}\int_0^{D/2} \bar{u}(y)dy \tag{5.12}$$

In which D is the pile diameter, and B is the flume width. The measurements were conducted at a fixed distance from the bed, $z/D = 1.83$. Thus, the flow deficit parameter becomes only a function of streamwise coordinate x in the pile wake. For the unsteady flow cases, flow deficit parameter is calculated as $(U_c - U_w)/U_0$ which corresponds to the peak time of the undisturbed flow (time labelled C for U1 and U3). The results for flow deficit measurements are shown in the following Figure 5.26.

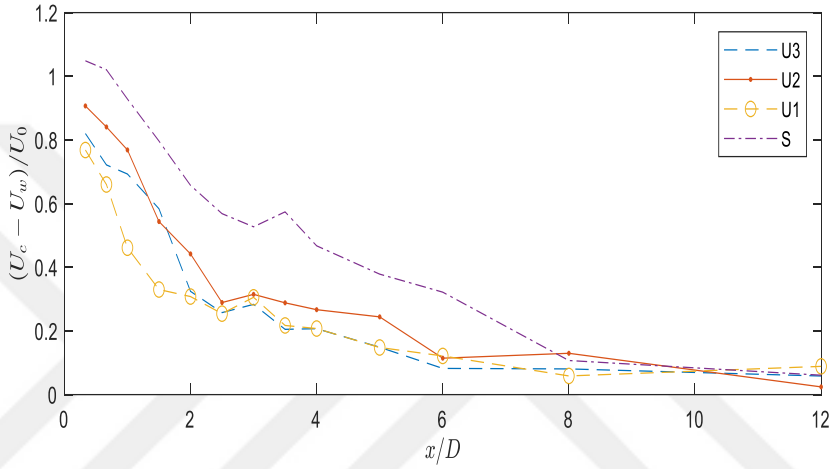

Figure 5.26 : Circular pile, flow deficit parameter corresponding to peak time of the undisturbed flow, $(U_c - U_w)/U_0$ as a function of x/D. Steady flow data is also presented for comparison.

Among the tested unsteady flow cases, the smallest flow deficit is caused by the U1 flow case, which is not surprising since U1 has the largest unsteadiness degree among the tested three unsteady flow cases. Although U2 shows larger flow deficit compared to U1 and U3, especially close to the pile, the difference between results of U2 and U3 flow cases are not much. The larger flow deficit of U2 flow case can be attributed to its dominant bi-modal character, which includes a local maximum (a minor peak) before the main peak of the flow is reached. Approximately 8D downstream of the pile, the flow deficit of steady and unsteady flow cases become practically the same, where flow deficit drops down to 10-15%.

5.4 Experimental Results for Piles with Elongated Cross Section

In this study in addition to circular cross section piles, piles with three different cross-sections were also tested in the experiments to analyze the influence of the pile shape on the flow structure and compare the results with those of the circular cross-section pile. The cross-sectional shape of the piles used here is elongated circles, which are more streamlined compared to a standard circular pile (Table 4.1). These cross-sections are identified with the length (L) to diameter (D) ratio as $L/D = 2$, $L/D = 3$, and $L/D = 4$, respectively. For all these cross-sections, both steady and unsteady flow conditions are tested. In the following sections, the results of the flow variations around these cross-sections are presented, section 5.4.1 presents the steady flow results and section 5.4.2 includes the unsteady flow results.

5.4.1 Elongated cross sections steady flow results

This section compares the results of flow structure in all four cross-sections tested under steady flow, in terms of Reynolds-averaged velocities and turbulence quantities around elongated cross-sections in steady flow. Figure 5.27 shows the Reynolds-averaged velocity variations in elongated cross-sections ($L/D = 2$, $L/D = 3$ and $L/D = 4$). The recirculation region in the immediate downstream part of the pile gets smaller as the pile shape gets longer and more streamlined, as shown in the figures. To put it in other words, the red-lined recirculation region in L/D=4 is smaller than those in the other two elongated cross-sections. Additionally, the velocity returns to its undisturbed velocity faster in this cross-section with the largest aspect ratio.

Figures 5.28 and 5.29 show the spatial variations of turbulence quantities downstream of the elongated cross-sections in the steady flow case. According to these figures the increased $\sqrt{\overline{v'^2}}/\mathrm{V}_{max}$ and $k/\mathrm{V}^2{}_{max}$ immediately downstream of the pile decreases as the pile gets longer and more streamlined.

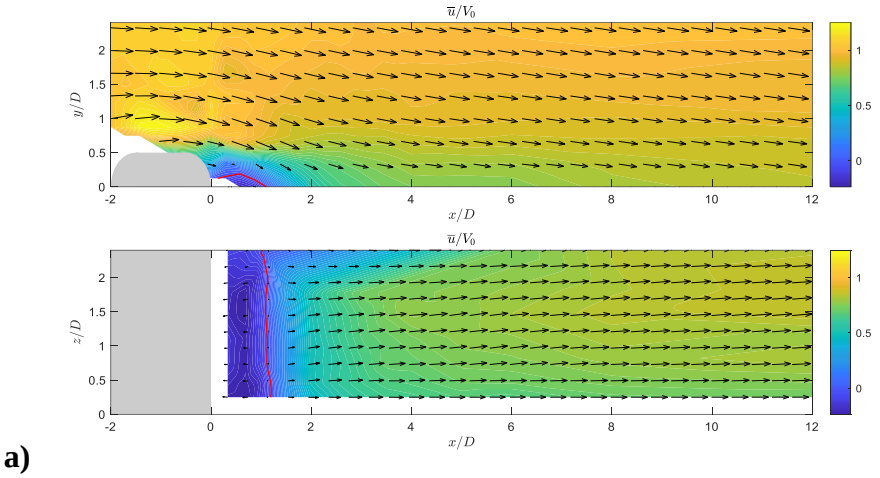

a)

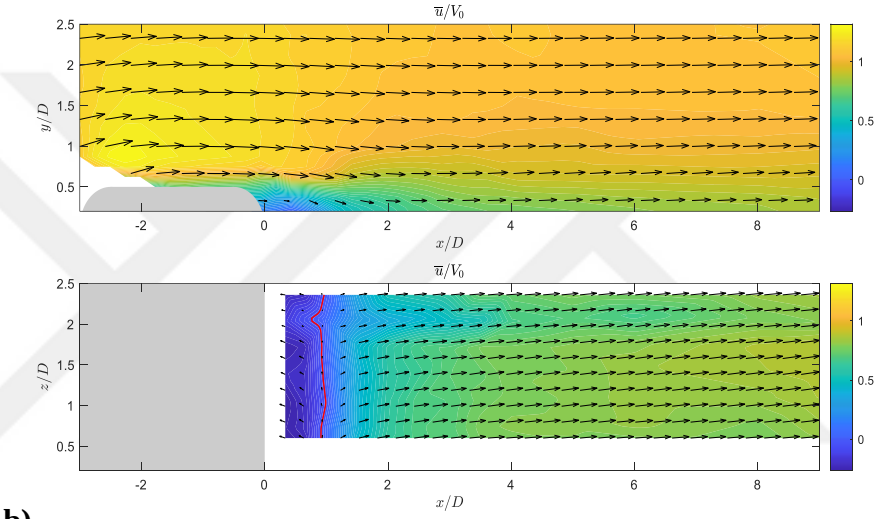

b)

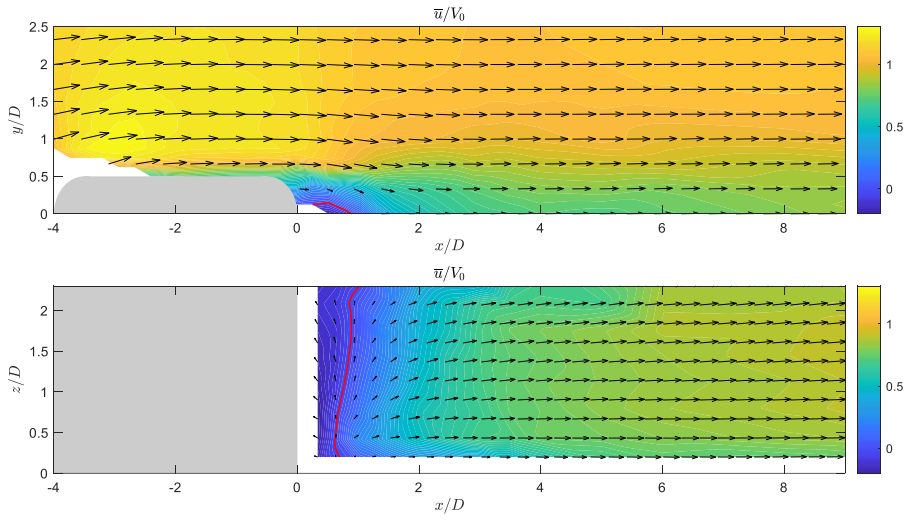

c)

Figure 5.27 : Reynolds-averaged velocity vectors and contour plot of $\overline{u}/V$ around the elongated piles a)$L/D = 2$, b)$L/D = 3$, c) $L/D = 4$.

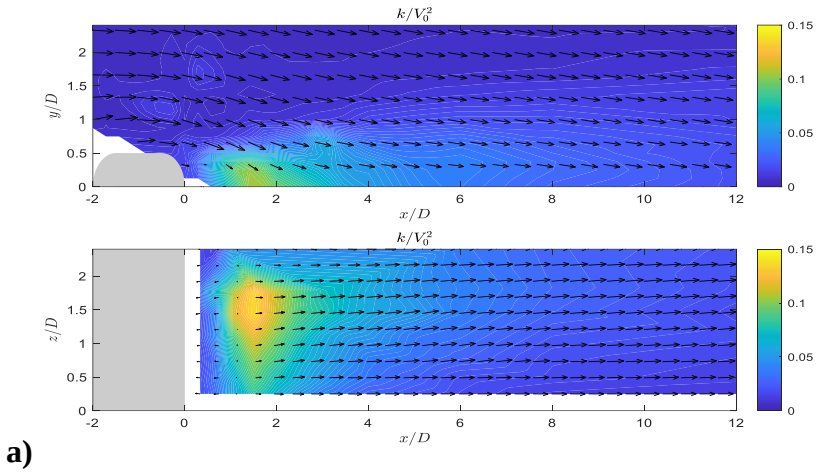

a)

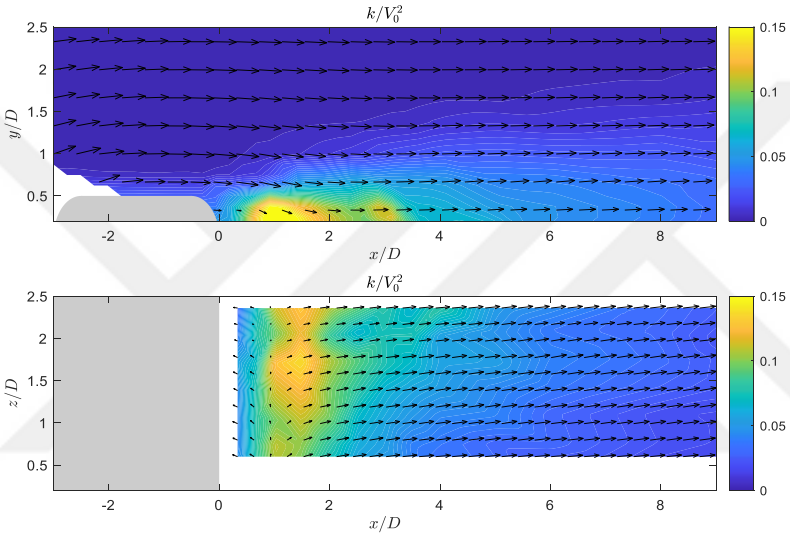

b)

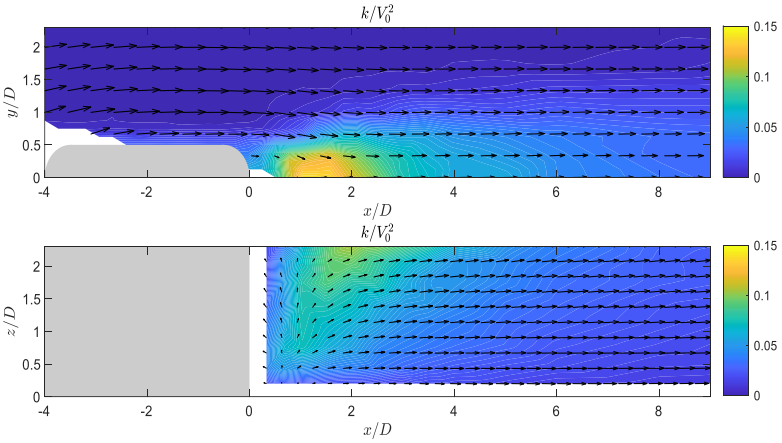

c)

Figure 5.28 : Turbulence kinetic energy k/V^2 variations around the elongated piles in steady flow case (case S), a) $L/D = 2$, b) $L/D = 3$, c) $L/D = 4$. Grey area is the pile.

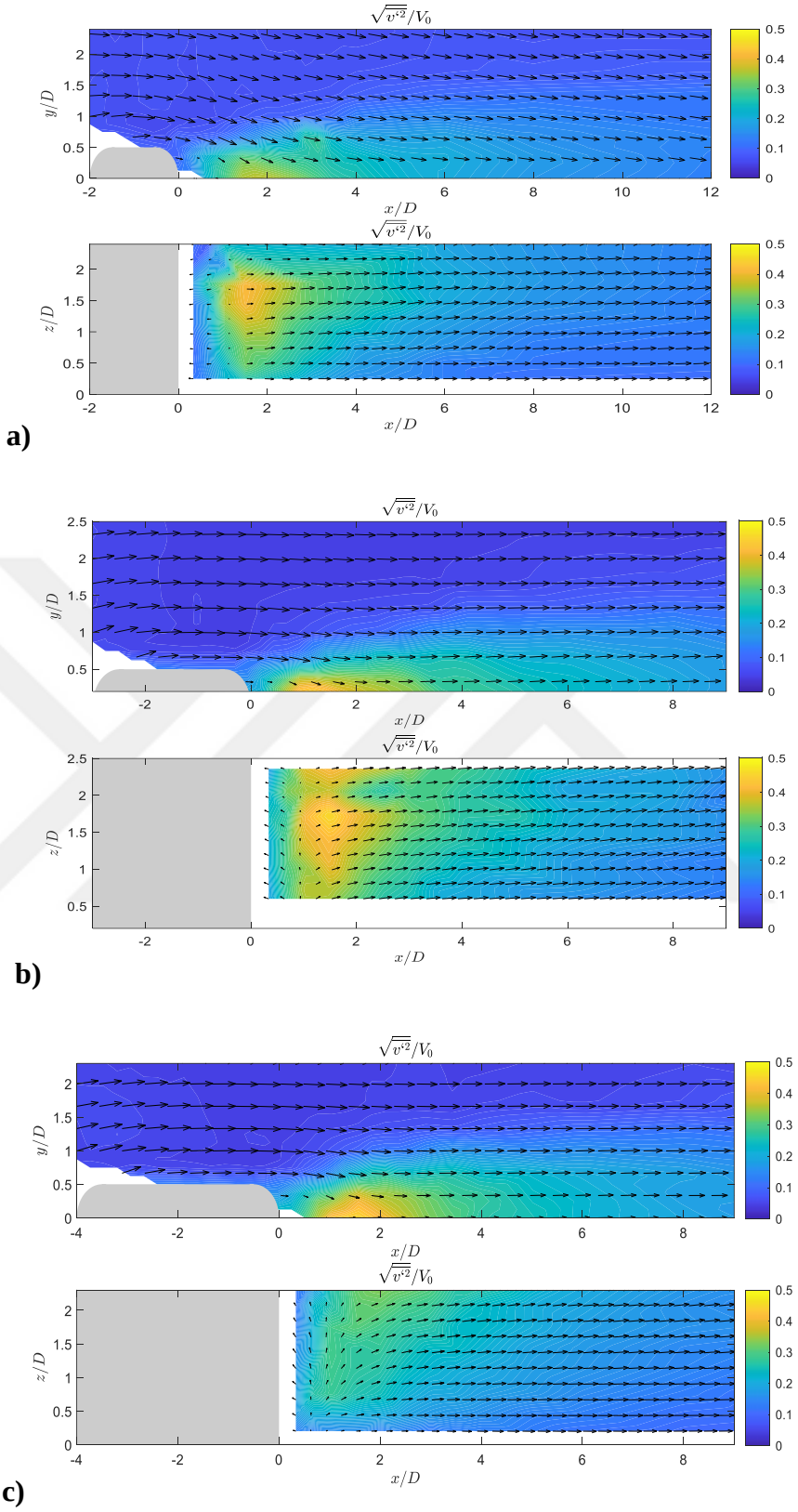

Figure 5.29 : Lateral fluctuating velocity $\sqrt{\overline{v'}^2}/V$ variations around the elongated piles in steady flow case (case S). a) L=2D, b) L=3D, c) L=4D.

The depth-averaged turbulence kinetic energy in the steady flow is calculated and its variations in the wake of all four cross-sections are shown in Figure 5.30 for comparison. As seen in this figure, k starts from a small value just behind the pile, where there is recirculation region, then attains to its peak, and eventually it decreases again with the downstream distance from the pile. At $x = 12D$, turbulence kinetic energy is seen to attain its minimum value. This trend occurs for all the cross-sections tested. In the circular pile, k is dominantly the highest among all the tested cross sections: While the cross section gets more streamlined, the intensity of wake turbulence decreases. As such, k has the lowest value in cross section $L = 4D$ among all the cross sections. Nevertheless, k in elongated cross sections ($L = 2D$, $L = 3D$ and $L=4D$) are close to each other.

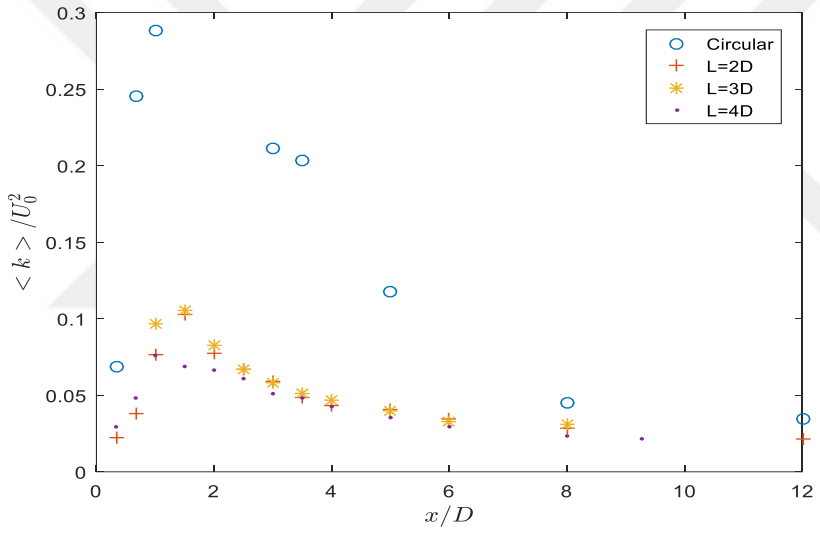

Figure 5.30 : Variation of depth-averaged turbulent kinetic energy <k> along the stream wise distance for different cross sections.

5.4.1.1 Flow deficit in the wake of the elongated cross sections in steady flow case

Across the horizontal plane (x-y plane), there is an increase in the flow velocity at the sides of the piles, where the streamlines are contracted. In order to compare the effect of the cross-sectional shape on the increase in velocity, the difference between the velocity in the contraction region and wake of the pile is calculated and the results are presented in Figure 5.32 for all the cross-sections (steady flow case), as done in Figure 5.26.

The flow deficit parameter was explained in section 5.3.2.3 above, and as illustrated before, it is defined as $(U_c - U_w)/U_0$. The equations related to velocity in the wake (U_w) and in the contracted region (U_c) are calculated as explained in Equations 5.11 and 5.12. Figure 5.33 presents the flow deficit parameter $(U_c - U_w)/U_0$ for all the cross sections tested in steady flow. In this figure the horizontal axis shows the non-dimensional distance from the pile (x/D) and the vertical axis shows $(U_c - U_w)/U_0$. According to Figure 5.33, there is a big difference between the wake and contracted region just behind the pile. The difference is maximum just behind the pile, and as one gets away from the pile, the difference between the wake and contraction region velocities gets smaller since the effect of the pile gradually disappears, and flow recovers. The decreasing trend of this difference is valid for all the cross sections. As shown in the figure the largest difference between these regions is in circular pile and as the pile gets larger the friction of the body of the pile also increases and the flow streamlines will be more contracted resulting in higher U_c, while on the other hand the velocity in the wake of the elongated cross sections will be lower due to the smooth transfer of the flow streamlines, moreover the recirculation region (as size and magnitude) is stronger in circular pile compared to the elongated piles.

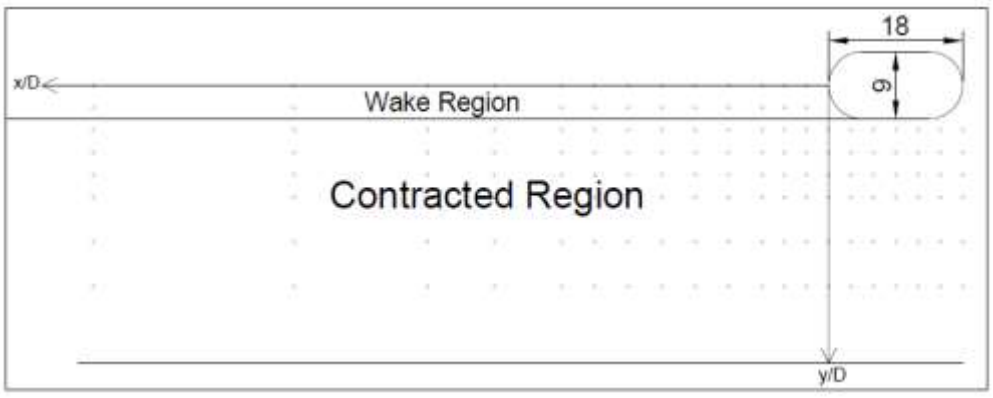

Figure 5.31 : Definitions of Contracted and Wake regions downstream of the piles.

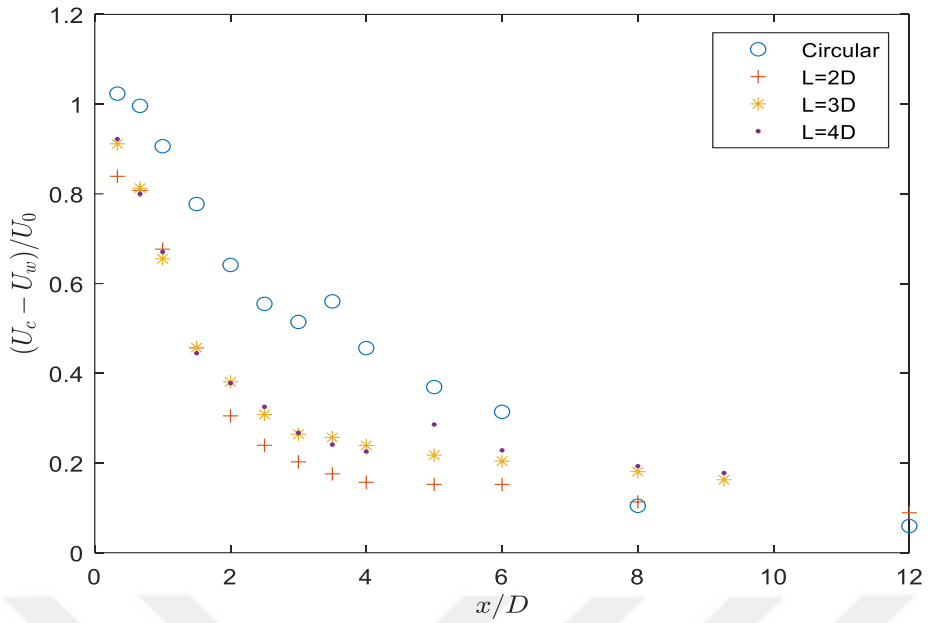

Figure 5.32 : Flow deficit parameter as a function of x/D in steady flow (case S) for circular and elongated cross sections.

5.4.2 Elongated cross sections unsteady flow results

Results for the unsteady experiments in elongated piles are presented in this section. For each cross section three different unsteady flows are tested, for reasons of space organization, the results of U1 and U3 are presented here, and the results of U2 and other detailed results are presented in the Appendix section of the thesis.

5.4.2.1 Unsteady flow results for elongated cross section L=2D

Figure 5.33 illustrates the Reynolds-averaged velocity ($\bar{u}/V_{max}$) around the elongated (L=2D) pile in U1 case at the peak time of the undisturbed unsteady flow velocity (points C and E). Figure 5.34 shows the spatial distribution of turbulence quantities for this pile in U1 case. For comparison, unsteady U3 case results of Reynolds-averaged velocity and turbulence quantities are also presented in Figures 5.35 and 5.36, respectively. As seen the flow contraction is very week in both U1 and U3 cases, compared to the circular pile case, which look very similar qualitatively and quantitatively (Figs. 5.33 and 5.35). Although the turbulence quantities in the wake of the elongated pile (L/D=2) are similar, U3 case exhibits slightly higher turbulence in the pile wake.

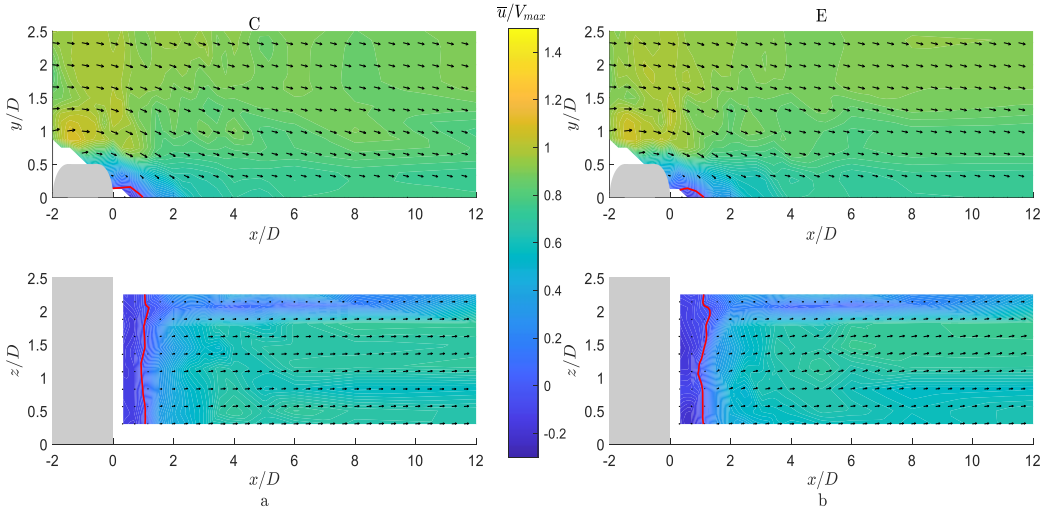

Figure 5.33 : Reynolds-averaged velocity vectors, and contour plot of $\bar{u}/V_{max}$ in elongated pile (L=2D) for unsteady U1 flow case, The red contour marks $\bar{u} = 0$.

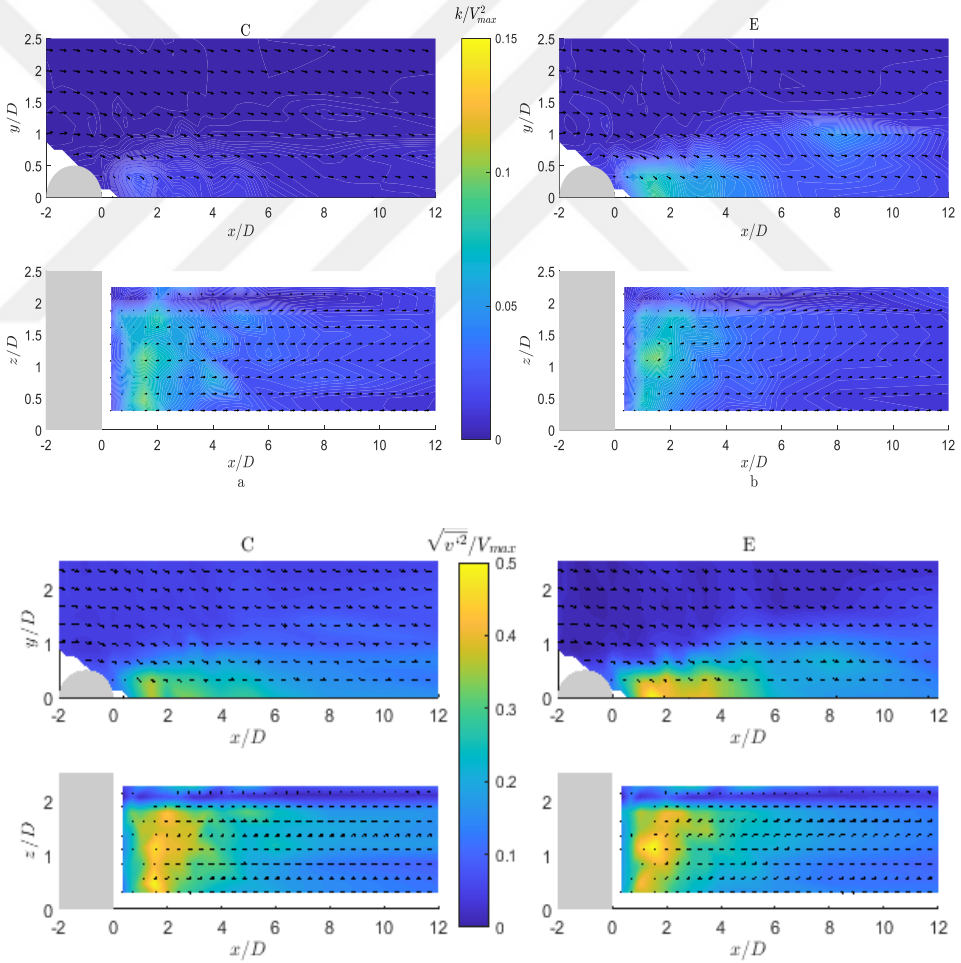

Figure 5.34 : Contour plot and variations of k/V_{max} and $\sqrt{\overline{v'^2}}/V_{max}$ in elongated pile ($L = 2D$) for unsteady U1 flow case.

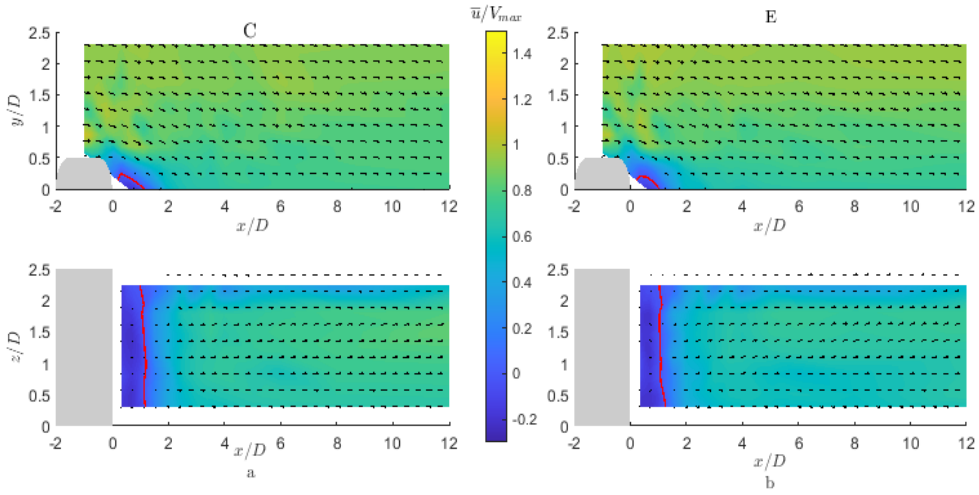

Figure 5.35 : Reynolds-averaged velocity vectors, and contour plot of $\bar{u}/V_{max}$ in elongated pile (L=2D) for unsteady U3 flow case, The red contour marks $\bar{u} = 0$.

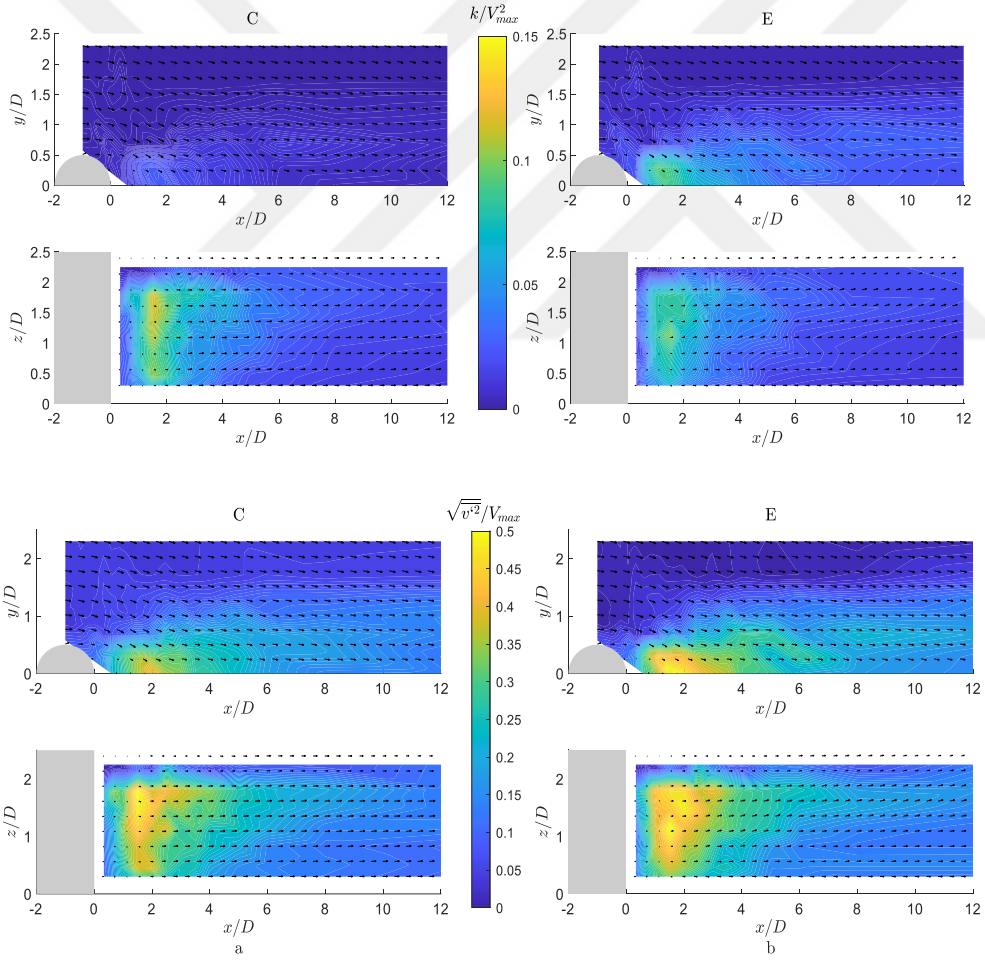

Figure 5.36 : Contour plot and variations of k/V_{max} and $\sqrt{\overline{v'^2}}/V_{max}$ in elongated pile (L=2D) for unsteady U3 flow case.

Turbulence and hysteresis in the wake of the elongated pile (L=2D)

According to Figure 5.37, it is seen that in U3 case the hysteresis is much smaller in comparison with the U1 flow case. Also, in both cases (U1 and U3) the turbulence during falling stage (blue curves) is larger than that during rising stage (red curves).

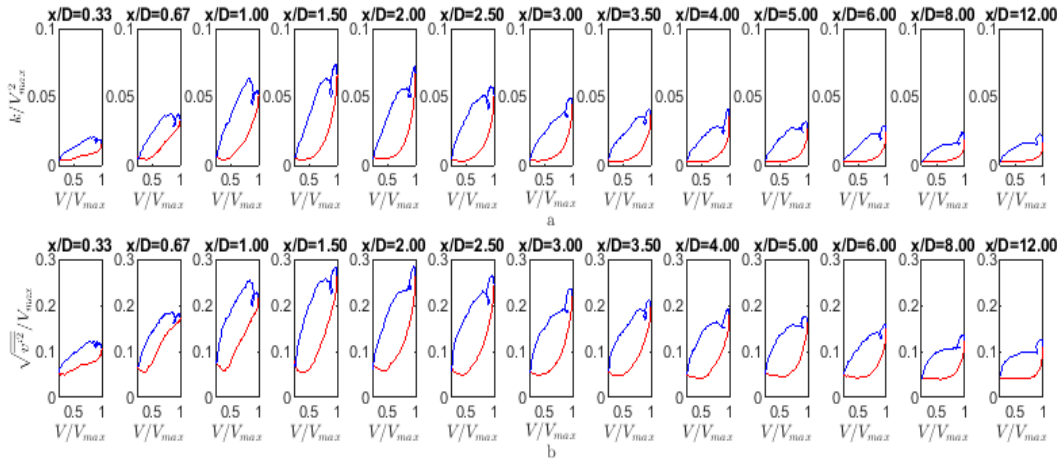

a)

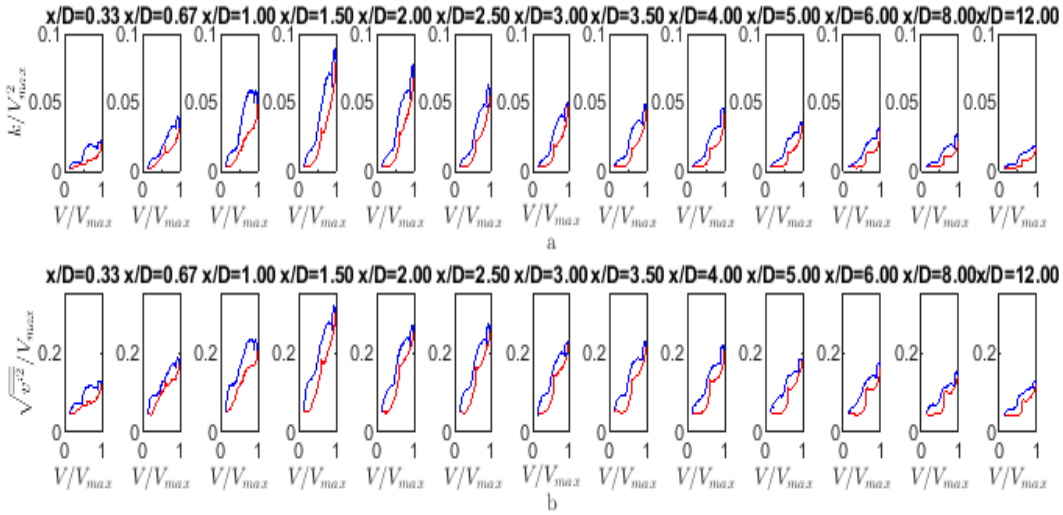

b)

Figure 5.37 : Variation of depth-averaged turbulence as a function of undisturbed flow velocity, V/V_{max} for the a) U1 and b) U3 flow cases in elongated pile ($L = 2D$), k/V_{max} and $\sqrt{\overline{v'^2}}/V_{max}$ variations are shown. Red curves are before the peak and blue curves are after the peak.

Figure 5.38 displays the variations of depth-averaged turbulence quantities as a function of streamwise distance downstream of the elongated pile (L/D=2) in S, U1, U2, and U3. Different than the circular pile case, the difference between steady and unsteady flow cases are very small. The turbulence kinetic energy in steady flow case

is still the highest, but quite close to are close to unsteady flow cases U2 and U3. By moving downstream to $x/D > 2.5$, the turbulence in the case of steady flow becomes practically the same with the unsteady flow cases (Figure 5.39a). The steady flow results for lateral turbulence fluctuations (figure 5.40b) has higher values than the unsteady flow cases for $1 \leq x/D \leq 2.5$, where pile generated turbulence reaches its largest values in the pile wake. Among the three unsteady flow cases U3 has the highest depth averaged turbulence kinetic energy and depth-averaged lateral turbulence fluctuations generated in this region. Further downstream the pile in $x/D > 2.5$, the unsteady flow case U2 has the smallest $\sqrt{\overline{v'^2}}$ values among the other flow cases.

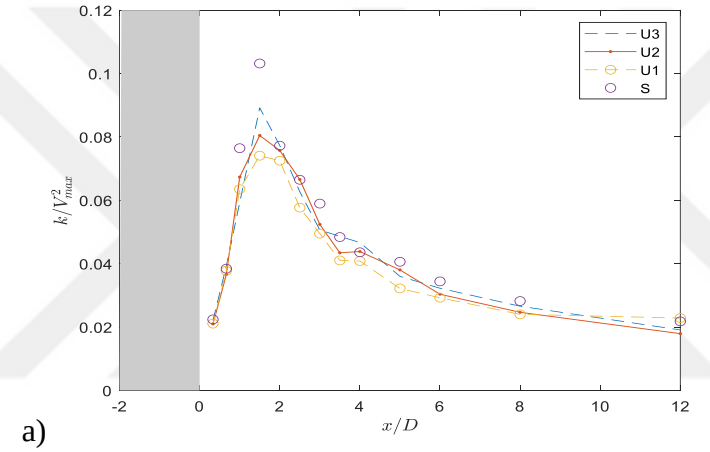

a)

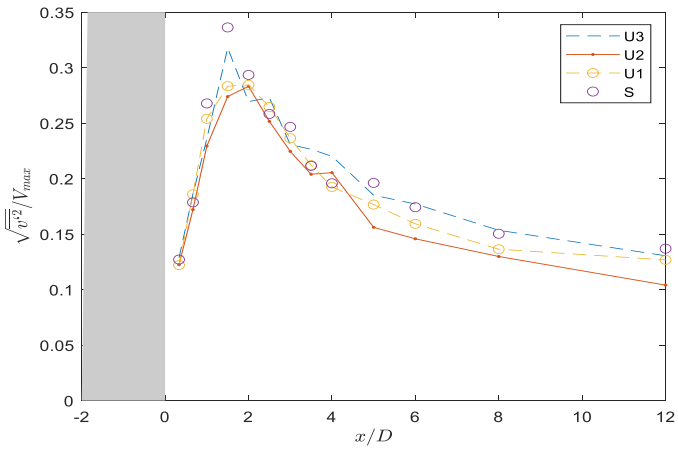

b)

Figure 5.38 : Depth averaged turbulence quantities measured as a function of x/D in the wake of the pile elongated pile ($L = 2D$) a) k/V_{max}^2 , b) $\sqrt{\overline{v'^2}}/V_{max}$.

Flow deficit in the elongated (L=2D) pile wake

Figure 5.39 shows the flow deficit in the wake of the pile with L=2D cross-section. As can be seen in the figure, steady flow has the highest flow deficit, but much smaller than the circular pile case (Figure 5.26) implying that vortex shedding is weaker in unsteady flow situations (same as undisturbed flow and circular pile). It is also seen from the figure that although the flow deficit in all four flow cases are very close, the U2 has highest flow deficit among the all the unsteady flow cases, which can be explained by its bi-modal character. Although the flow deficit in the U1 case is the smallest, as one moves further downstream the pile, it becomes practically equal to the flow deficit in the U3 case.

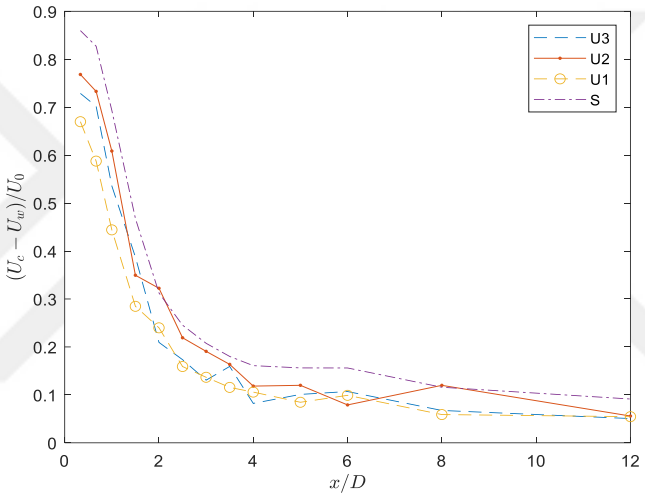

Figure 5.39 : Flow deficit parameter corresponding to peak time of the undisturbed flow $(U_c - U_w)/U_0$, as a function of x/D. For elongated pile (L=2D). Steady flow data is also presented for comparison.

5.4.2.2 Unsteady results for elongated cross section L=3D

Reynolds-averaged velocity around the L=3D cross-section is presented in the Figure 5.40. When we compare the results to the steady flow case, we can see that the contraction velocity at the pile's sides is much lower in the unsteady flow case than in the steady flow case, and that the recirculation region in the U1 case is smaller than in the steady flow case. The contour plots of k/V_{max}^2 and $\sqrt{\overline{v'^2}}/V_{max}$ are shown in figure 5.41. Comparing the results with the steady flow we can see that lateral fluctuations and turbulence downstream the pile is reduced in unsteady flow case. Figures 5.42 and 5.43 present the results of the U3 flow case. Here we can see that contraction velocity

is also smaller than the steady flow case and that turbulence variations are also smaller than the steady case.

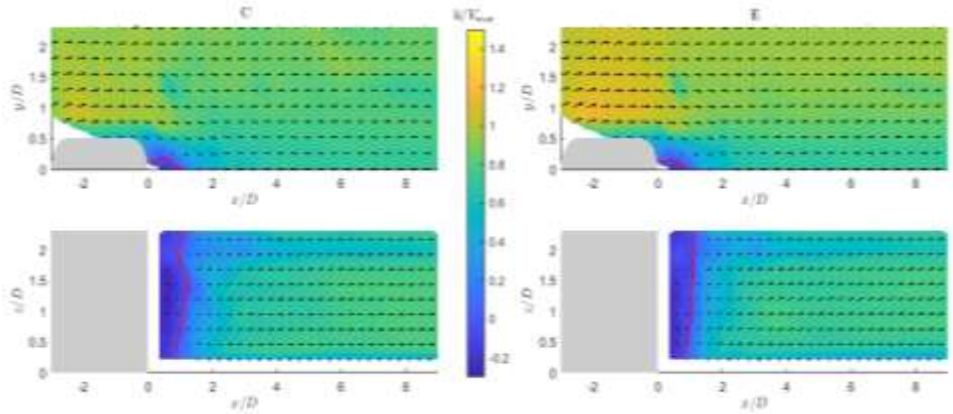

Figure 5.40 : Reynolds-averaged velocity vectors, and contour plot of $\bar{u}/V_{max}$ in elongated pile (L=3D) for unsteady U1 flow case, The red contour marks $\bar{u} = 0$.

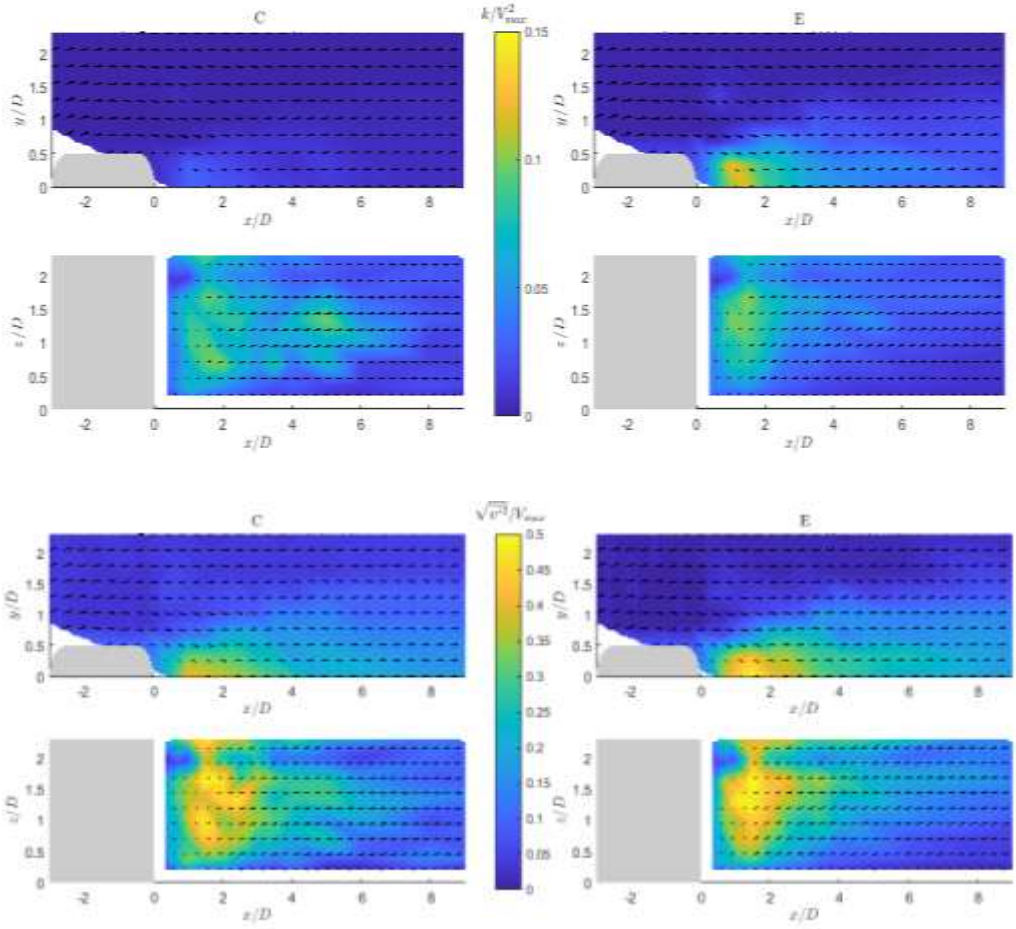

Figure 5.41 : Contour plot and variations of k/V_{max} and $\sqrt{\overline{v'^2}}/V_{max}$ in elongated pile (L=3D) for unsteady U1 flow case.

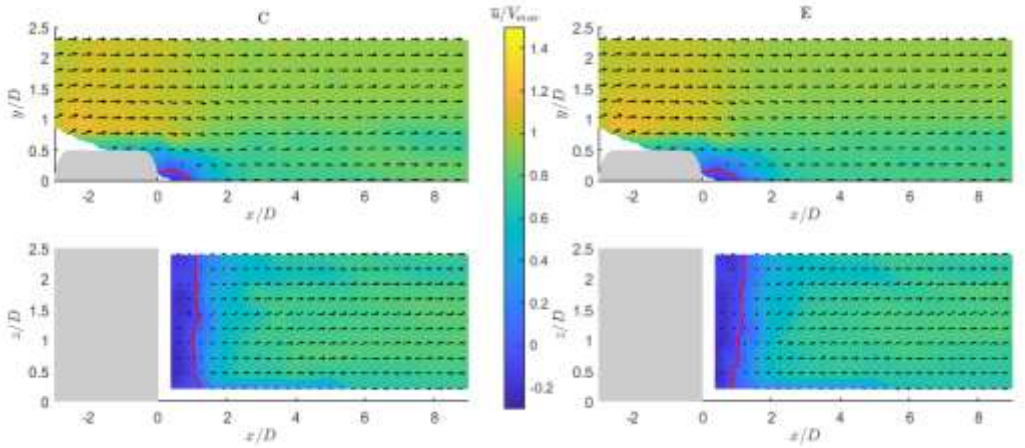

Figure 5.42 : Reynolds-averaged velocity vectors, and contour plot of $\bar{u}/V_{max}$ in elongated pile (L=3D) for unsteady U3 flow case, The red contour marks $\bar{u} = 0$.

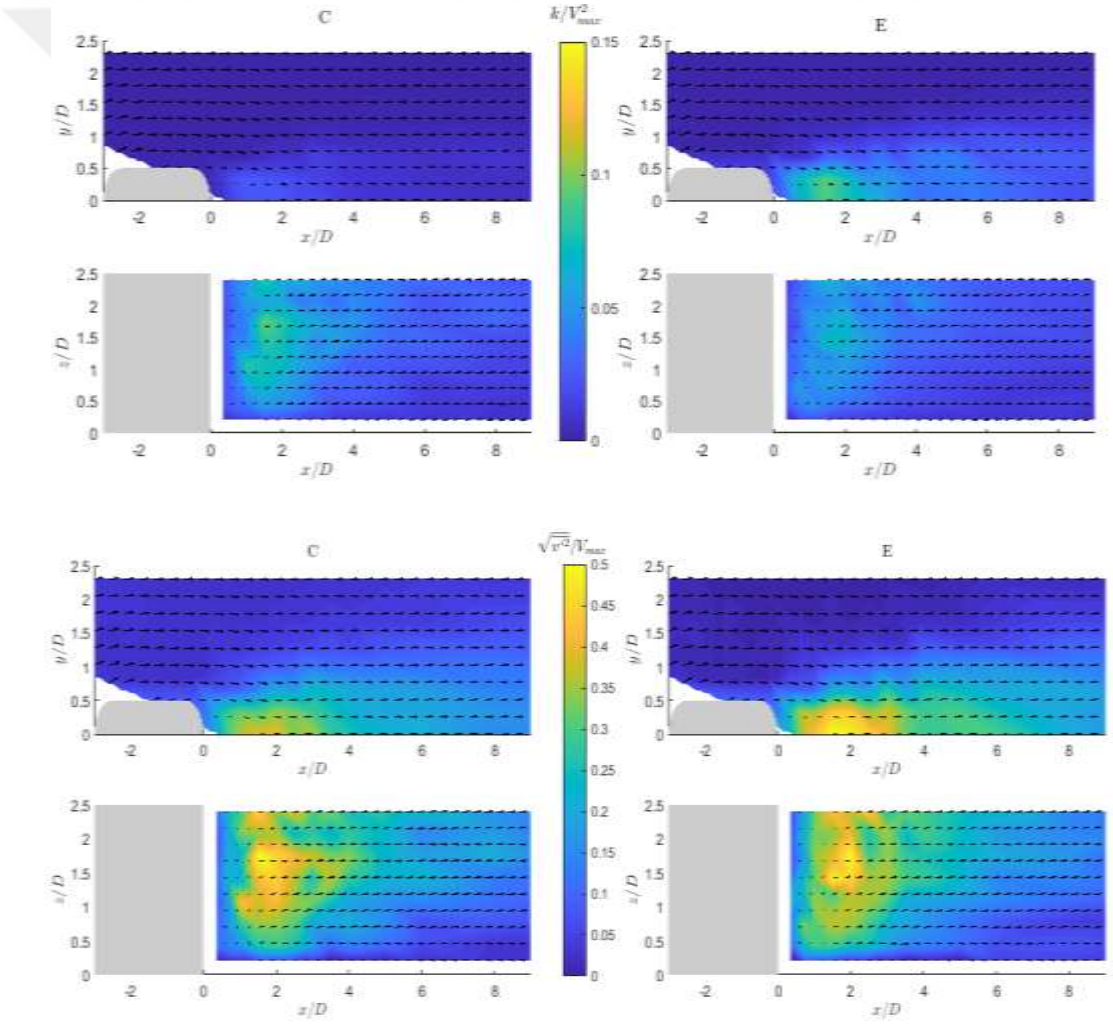

Figure 5.43 : Contour plot and variations of k/V_{max} and $\sqrt{\overline{v'^2}}/V_{max}$ in elongated pile (L=3D) for unsteady U3 flow case.

Turbulence and hysteresis in the wake of the elongated pile (L=3D)

Figure 5.44 shows the hysteresis between the flow velocity and turbulence inherent in the L=3D pile and both U1 and U3 flow cases. As seen from the figures the hysteresis in the U1 case (Figure 5.44a) is much larger since in the U1 case the unsteadiness is larger according to the U3 case.

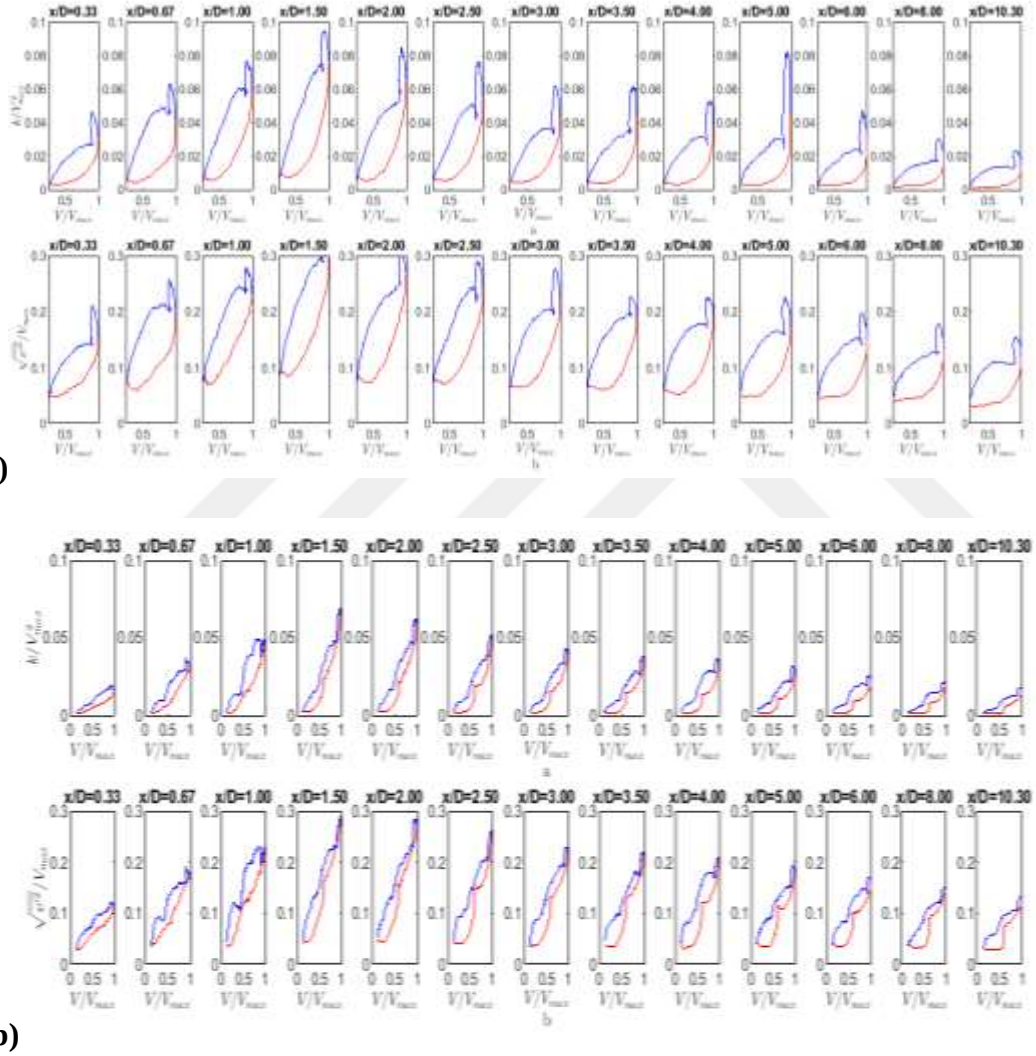

a)

b)

Figure 5.44 : Variation of depth-averaged turbulence as a function of undisturbed flow velocity, V/V_{max} for the a) U1 and b) U3 flow cases in elongated pile ($L = 3D$), a) $k/V_{max}^2$and b) $\sqrt{\overline{v'^2}}/V_{max}$. Red curves are before the peak and blue curves are after the peak.

The following figure (Figure 5.45) represents the depth-averaged turbulence variations for all the flow types (steady and unsteady) downstream the L=3D cross-section. In

Figure 5.45a, we can see that turbulence variations are higher in steady flow according to other unsteady flow types, among the unsteady flows U3 flow has the lowest turbulence kinetic energy values, as we move downstream and away from the pile, the steady flow values get closer to the unsteady (U2) flow.

Figure 5.45b shows the lateral fluctuations of the flow, which shows that steady flow has the highest value and U3 unsteady flow owns the lowest value. This is different from the L=2D cross-section results.

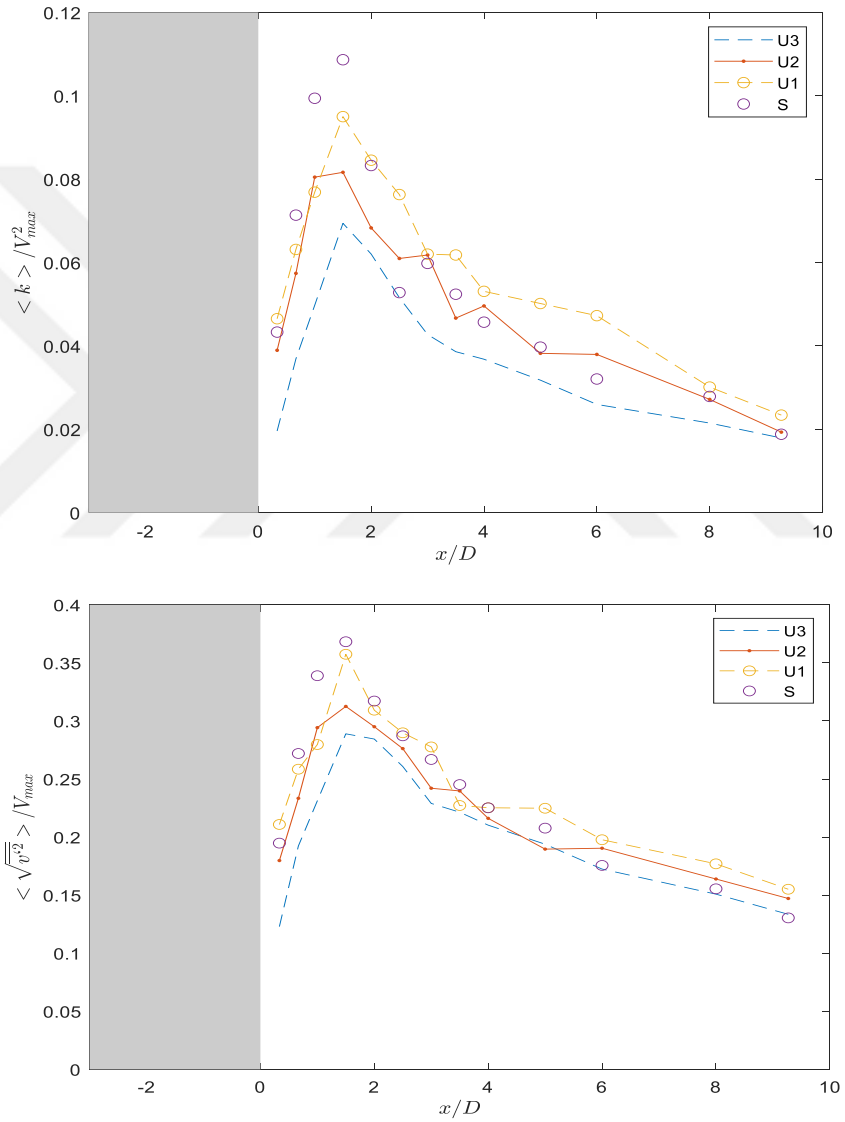

Figure 5.45 : Depth averaged turbulence quantities measured as a function of x/D in the wake of the pile a)k/V_{max}^2 , b)$\sqrt{\overline{v'^2}}/V_{max}$. For elongated pile (L=3D). Steady flow case is also presented for comparison.

Flow deficit in the elongated (L=3D) pile wake

Figure 5.46 shows the flow deficit in the L=3D cross-section, which shows that the steady flow has the highest flow deficit and U2 has the highest value among the unsteady flows, while U1 and U3 are slightly different. U3 is somewhat higher than U1 close to the pile, and as you move downstream, it becomes clear that U1 and U3 have a flow deficit close to each other.

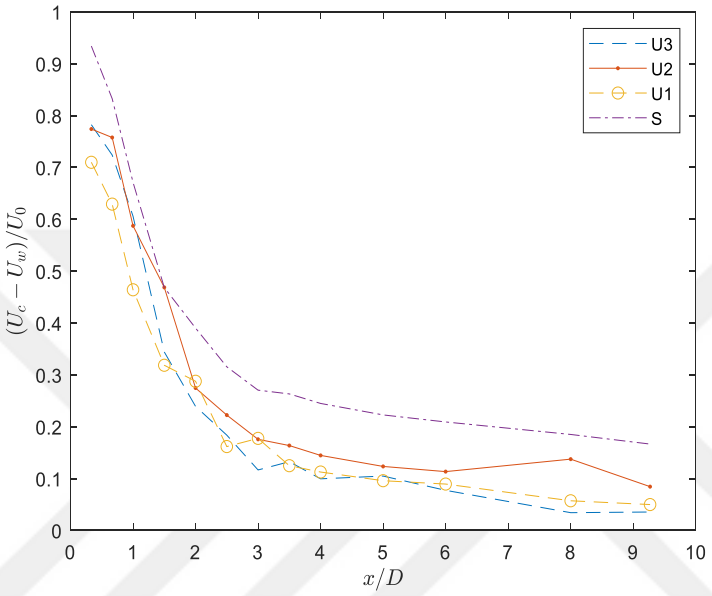

Figure 5.46 : Flow deficit parameter corresponding to peak time of the undisturbed flow $(U_c - U_w)/U_0$, as a function of x/D. For elongated pile (L=3D). Steady flow data is also presented for comparison.

5.4.2.3 Unsteady results for elongated cross section L=4D

Reynolds-averaged velocity variations and contour plots around the L=4D cross-section at the instants labelled as C and E are shown in figure 5.47. As seen from this figure recirculation region (the region marked with red line) is very small according to other cross sections and also in compare with steady flow. Moreover, it is clear from the figure 5.47 that velocity in the contraction region is weaker according to steady flow case.

The contour plots of $< k > / V_{max}^2$ and $< \sqrt{\overline{v'^2}} > / V_{max}$ at times of C and E for L=4D cross-section are presented in figures 5.48. When compared with steady flow case it is seen that the turbulence and lateral fluctuations are higher in unsteady (U1) case.

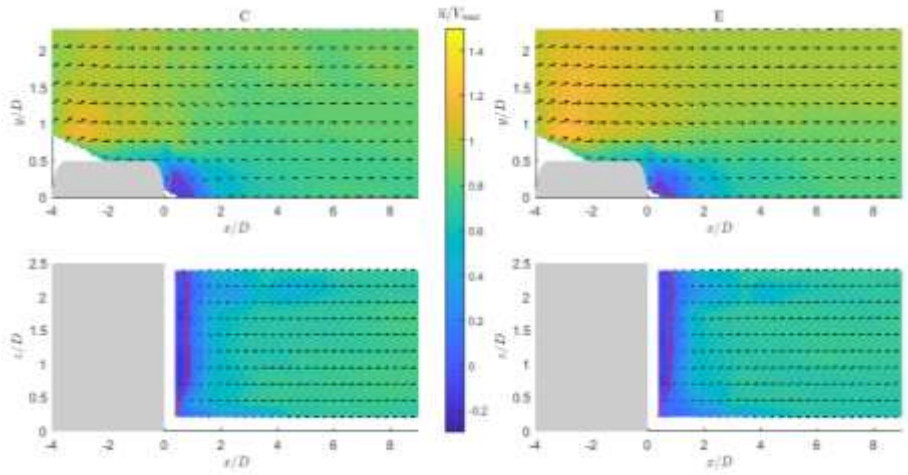

Figure 5.47 : Reynolds-averaged velocity vectors, and contour plot of $\bar{u}/V_{max}$ in elongated pile (L=4D) for unsteady U1 flow case, The red contour marks $\bar{u} = 0$.

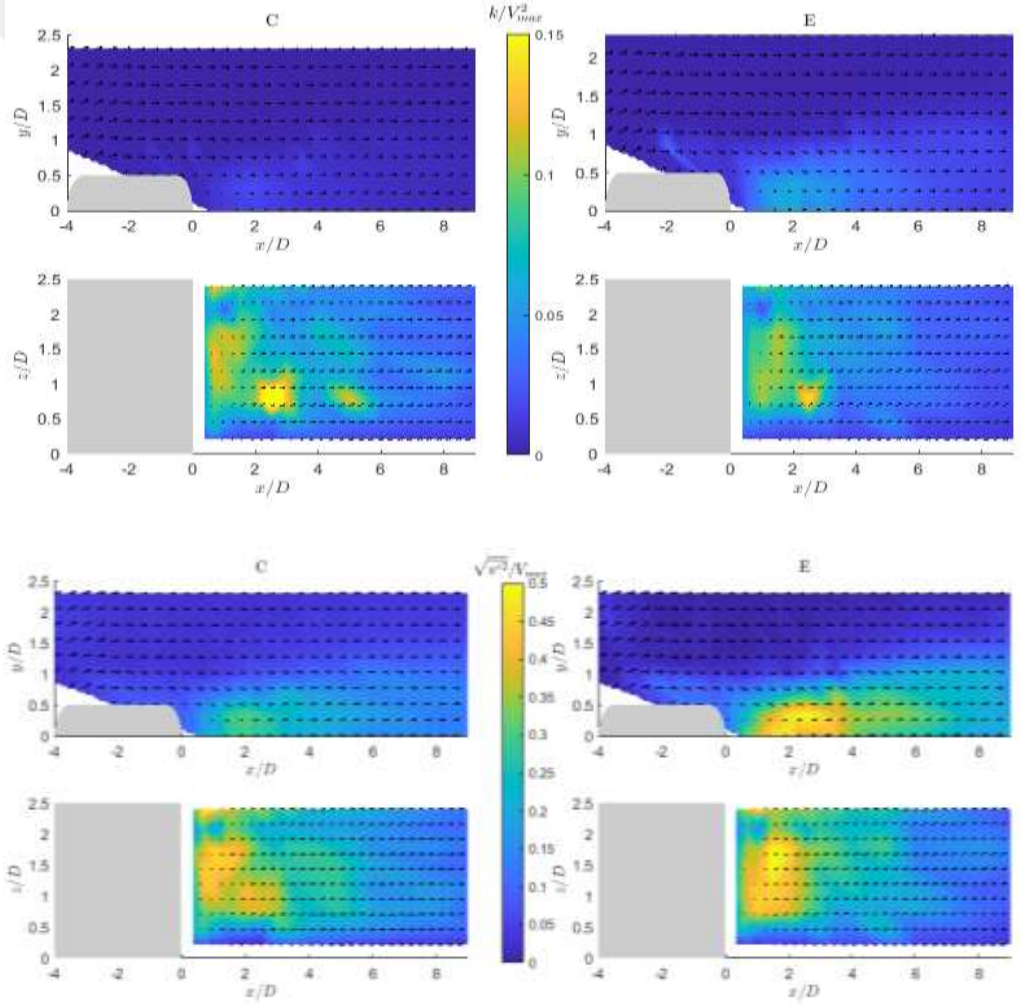

Figure 5.48 : Contour plot and variations of k/V_{max} and $\sqrt{\overline{v'^2}}/V_{max}$ in elongated pile (L=4D) for unsteady U1 flow case.

The results of the U3 flow variations around the L=4D cross-sections are presented in figures 5.49 and 5.50. Reynolds-averaged velocity variations ($\bar{u}/V_{max}$) in this case shows that the recirculation region involves a larger area in comparison with steady flow case and also we can see that in the contraction region between the pile and the wall velocity is smaller according to the steady flow case (Figure 5.29c).

Turbulence kinetic energy variations downstream the L=4D pile (Figure 5.50) in times C and E shows that in time E $< k > / V_{max}^2$ has alsmost close values to steady flow case. Also lateral fluctuation variations in U3 case shows much higher values in compare with the steady flow in L=4D pile. This shows that in elongated piles the presence of the pile in unsteady flows increases the fluctuations in the downstream the pile.

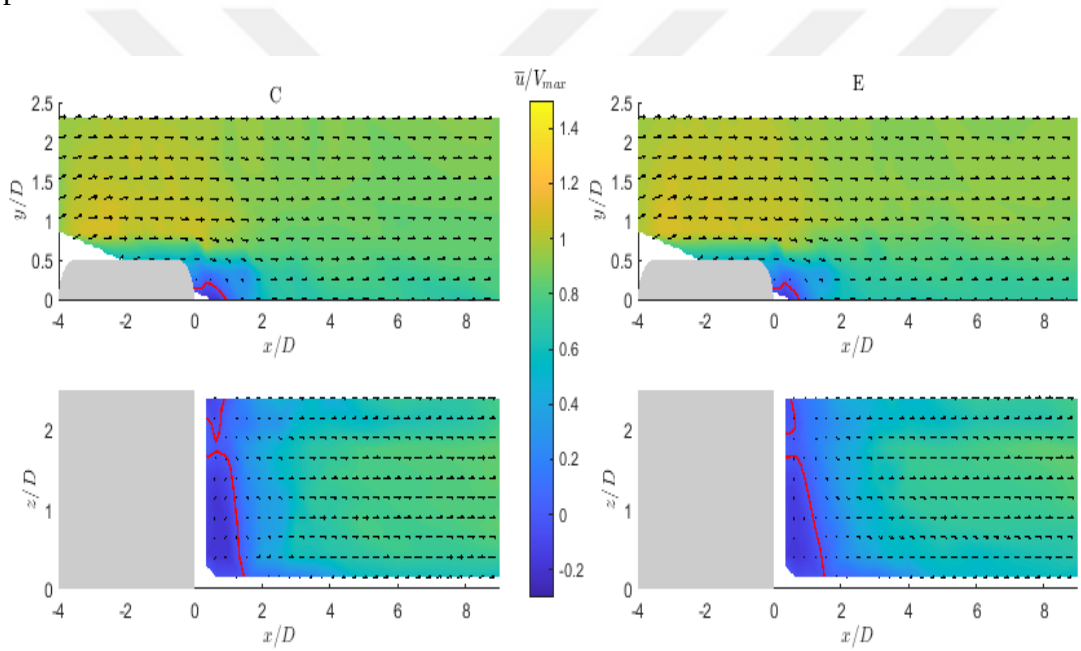

Figure 5.49 : Reynolds-averaged velocity vectors, and contour plot of $\bar{u}/V_{max}$ in elongated pile (L=4D) for unsteady U3 flow case, The red contour marks $\bar{u} = 0$.

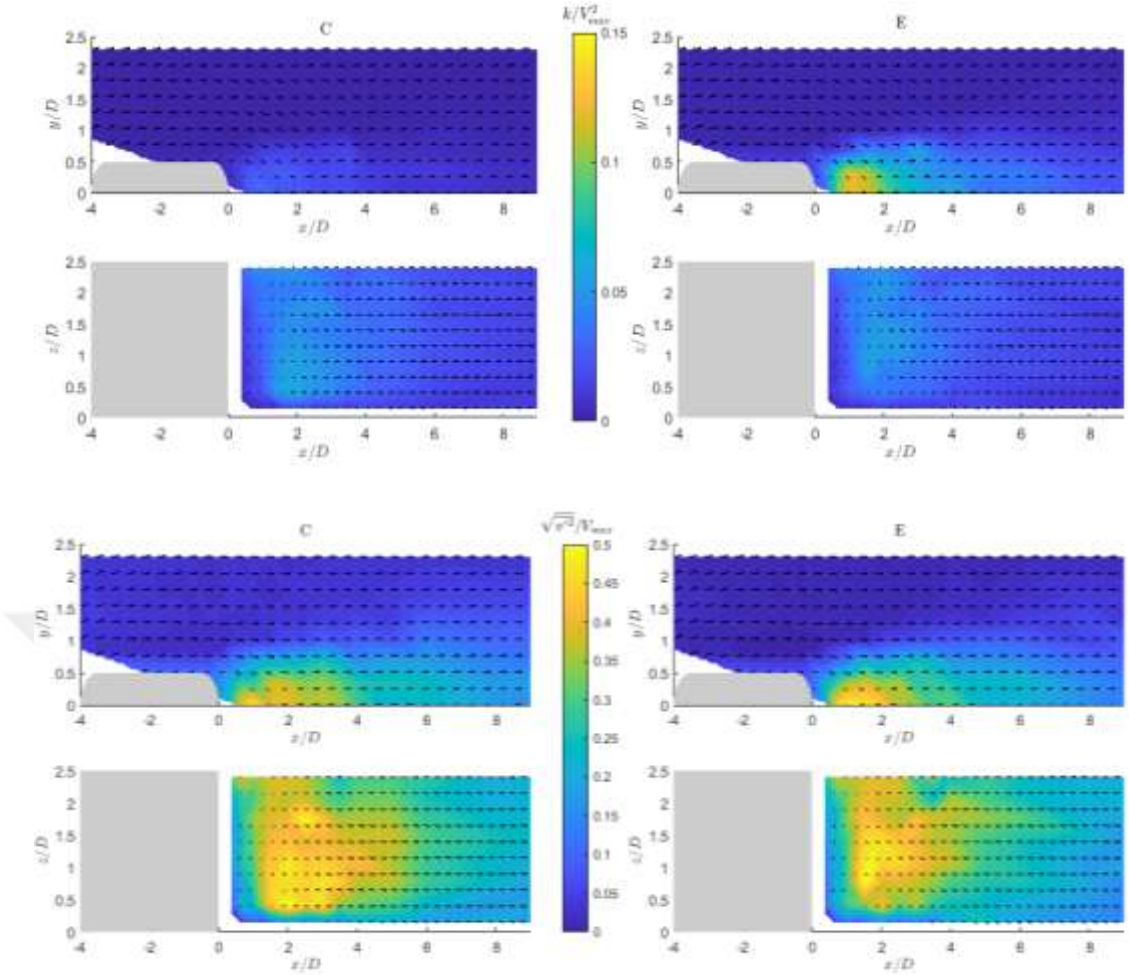

Figure 5.50 : Contour plot and variations of $< k >/V_{max}$ and $< \sqrt{\overline{v'^2}} >/V_{max}$ in elongated pile (L=4D) for unsteady U1 flow case.

Turbulence and hysteresis in the wake of the elongated pile (L=4D)

Comparing the hysteresis in U1 (Figure 5.51a) and U3 (Figure 5.51b) cases it is clear that the U1 case has higher hysteresis which is expected knowing that U1 case has higher unsteadiness degree. In both U1 and U3 case we can see that in the rising stage the turbulence quantity is smaller than the falling stage of the hydrograph. Only in some point close the pile in U3 case we can see that the turbulence values in the rising and falling stages of the hydrograph are close and the hysteresis effect disappears and also in $x/D = 1.5$, we can see that turbulence values in the rising and falling parts of the hydrograph gets opposite.

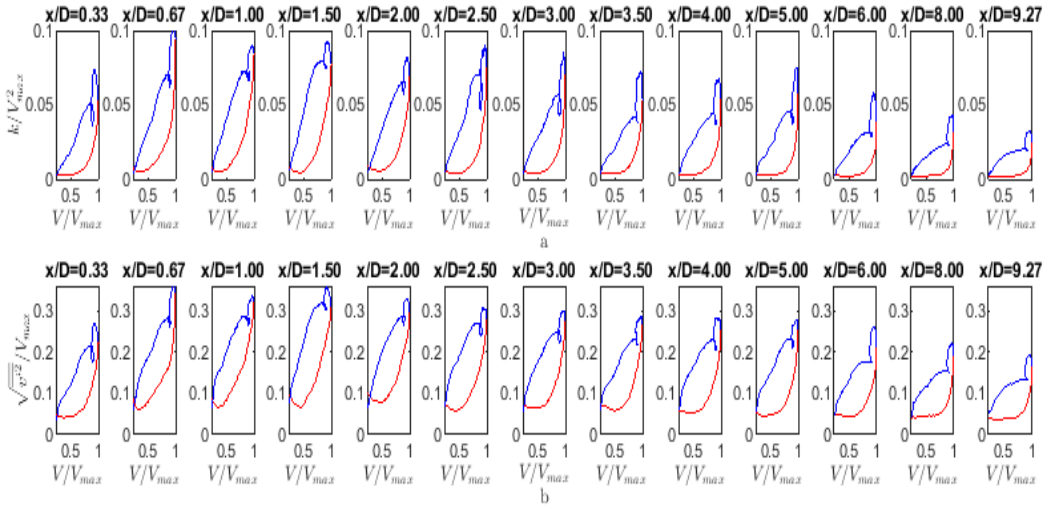

a)

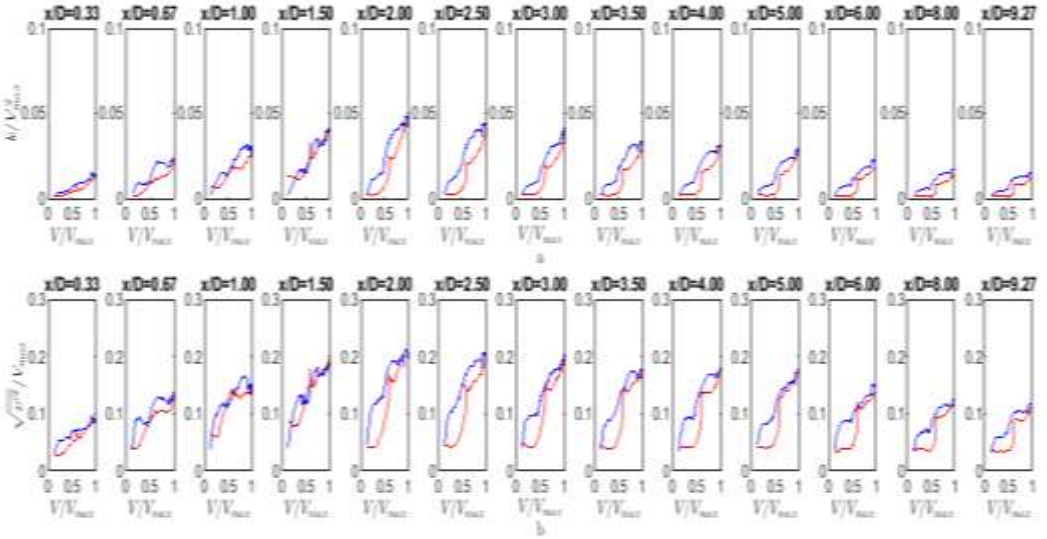

b)

Figure 5.51 : Variation of depth-averaged turbulence as a function of undisturbed flow velocity, V/V_{max} for the a) U1 and b) U3 flow cases in elongated pile $(L = 4D)$.

Depth averaged turbulence variations downstream the pile shows that U2 case has the highest value among the other flow cases. Also we can see that U3 case has the smallest variations of turbulence kinetic energy (Figure 5.52a) and lateral fluctuations (Figure 5.52b). The results here are different according to the other cross-sections, where turbulence was highest for the steady flow case.

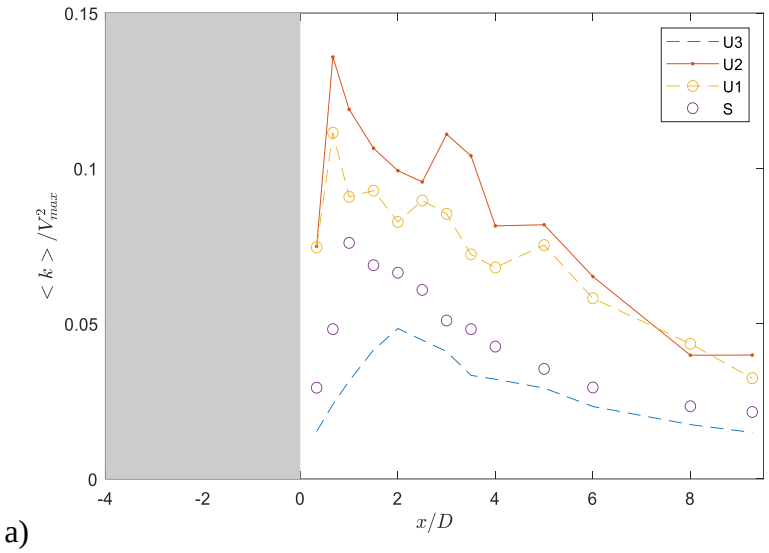

a)

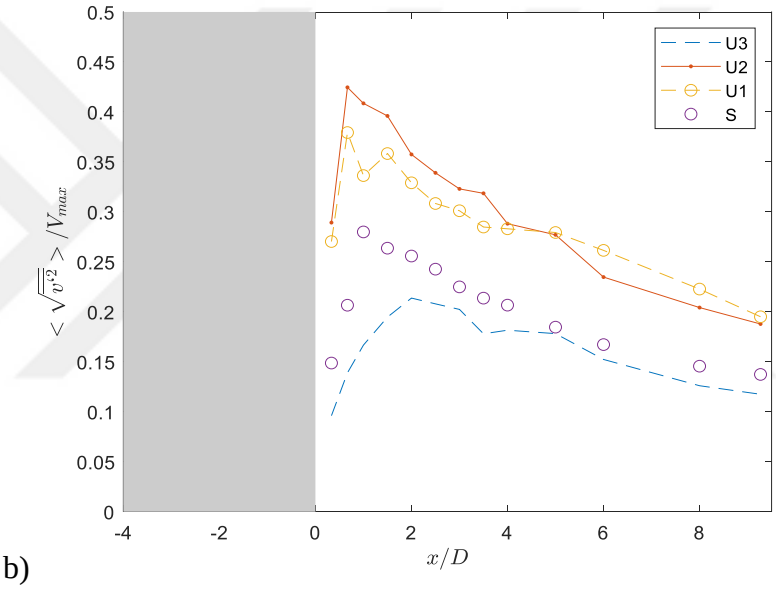

b)

Figure 5.52 : Depth averaged turbulence quantities measured as a function of x/D in the wake of the pile a) $<k>/V_{max}$, b) $<\sqrt{\overline{v'^2}}>/V_{max}$. For elongated pile (L=4D). Steady flow case is also presented for comparison.

Flow deficit in the elongated (L=4D) pile wake

Flow deficit in steady flow case has the highest value in compare with other flow cases. Among the unsteady flows just behind the pile the three cases have the almost close values to each other, moving further downstream the U2 gets higher values according to the other two unsteady cases (U1 and U3) which have almost close values to each other.

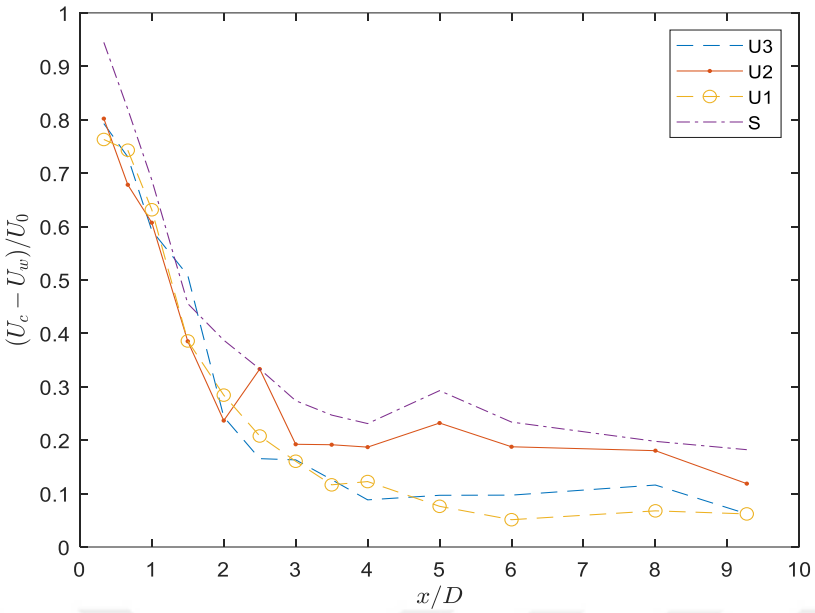

Figure 5.53 : Flow deficit parameter corresponding to peak time of the undisturbed flow $(U_c - U_w)/U_0$, as a function of x/D. For elongated pile (L=4D). Steady flow data is also presented for comparison.

6. CONCLUSION

In this thesis study, interaction of bridge piers with the gradually-varying unsteady flow during the passage of a hydrograph was investigated experimentally. Four different types of bridge piers, one with circular cross-section and three with elongated circular cross-section, whose length to width ratio is L/D=2, 3 and 4, respectively, were investigated. Laboratory experiments were used to investigate the interaction of these four types of bridge piers with unsteady flows (i.e. hydrographs) with three different degrees of unsteadiness. Moreover, the steady and unsteady flow conditions in the absence of the pier (undisturbed cases) were included in the study for reference purposes. The water depth was kept constant during the experiments. Reynolds averaged velocity and turbulence characteristics of the flow in different conditions were measured and determined by means of using densely conducted point velocity measurements. Additionally, water level and hydraulic slope measurements were also performed precisely throughout the experiments.

The analysis lead to the following conclusions:

1. In the no-pile tests performed with unsteady flow, the flow (especially during the rising curve of the hydrograph) cannot be considered to be fully developed. It has been observed that the velocity profiles in the flume for all the three types of unsteady flow cases attained to logarithmic profile when it is approximately 45% of duration of the hydrograph. During these experiments, the flow close to the bed of the channel adapts to the varying pressure gradient much faster than the upper part of the flow, resulting in relatively higher turbulence and shear stress near the bottom during the rising curve of the hydrograph, while this balance is reversed during the falling wing of the hydrograph. The resulting hysteresis between turbulence and the mean flow was seen to be comparable in all three tested unsteady flow cases.
2. When the bridge piers with different cross-sectional shapes tested under steady flow are evaluated together, there are significant differences among the resulting flow

fields depending on the cross-sectional shape, both in the contraction region (at the sides of the bridge pier) and in the wake. For the circular pile, the highest Reynolds averaged velocity occurs slightly downstream of the side of the cylinder, while this point is located exactly next to the cylinder for the elongated piles. This point is important considering the issue of local scouring. However, while the highest turbulence values at the downstream of the circular cross-section bridge pier are maximized at approximately 2D distance, this distance decreases as the bridge pier gets more elongated. Also, the recirculation region in downstream of the elongated bridge piers are narrower and more uniform throughout the depth. Generally speaking, the structure becomes more streamlined as the aspect ratio increases. However, as the cross-section gets longer, the lateral surface of the bridge pier subjected to friction also increases. Resulting flow behavior was observed to be a combination of these two effects.

3. In the experiments carried out under unsteady flow, it has been observed that the turbulence occurring downstream of the bridge piers with elongated cross-section is significantly less than the steady flow situation. However, such a difference was not observed for the cylinders with circular cross-section. This behavior is reversed for the bridge pier with the longest cross section (L/D=4), such that some of the unsteady flow cases resulted with higher wake turbulence than the steady flow case. It is understood that more shear stress and turbulence occur along the rising curve of the hydrograph compared to the falling curve. While this difference is very high for the circular cylinder, it somewhat decreases as the cross-section gets elongated.

4. According to the results it is understood that hysteresis effect occurring along the rising and falling curves of the unsteady flow increases as the degree of unsteadiness increases. In addition, as the cross-section gets more elongated, the form of the bridge pier becomes more hydrodynamic, and the hysteresis effect is reduced in the downstream due to the decrease in form resistance and increase in the friction resistance. Accordingly, it can be concluded that bridge piers with elongated cross-section will be less affected by unsteady flow conditions than bridge piers with circular cross-section.

5. Although it has been observed that under steady and unsteady flow types less resistance, shear stress and turbulence is created in the cases of elongated cross-sections, these effects are seen to spread to a wider region downstream, especially under unsteady flow. Although it is expected that the cylinders with elongated cross-section will reveal a lower scour depth than their circular cross-section counterpart, it is considered that the scour hole (especially towards the downstream) is likely to spread over a wider area. It is recommended to consider this point in the design of scour protection for extended cross-section bridge piers.

REFERENCES

Afzalimehr, H., & Anctil, F. (1999). Velocity distribution and shear velocity behaviour of decelerating flows over a gravel bed. *Canadian Journal of Civil Engineering*, *26*(4), 468-475.

Amini, A., Melville, B. W., Ali, T. M., & Ghazali, A. H. (2012). Clear-Water Local Scour around Pile Groups in Shallow-Water Flow. *Journal of Hydraulic Engineering*, *138*(2), 177-185.

Amini Baghbadorani, D., Ataie-Ashtiani, B., Beheshti, A., Hadjzaman, M., & Jamali, M. (2018). Prediction of current-induced local scour around complex piers: Review, revisit, and integration. *Coastal Engineering*, *133*, 43-58.

Ataie-Ashtiani, B., & Aslani-Kordkandi, A. (2012). Flow field around side-by-side piers with and without a scour hole. *European Journal of Mechanics - B/Fluids*, *36*, 152-166.

Ataie-Ashtiani, B., & Aslani-Kordkandi, A. (2012). Flow Field Around Single and Tandem Piers. *Flow, Turbulence and Combustion*, *90*(3), 471-490.

Baker, C. (1979). The laminar horseshoe vortex. *Journal of Fluid Mechanics*, *95*(2), 347-367.

Baykal, C., Sumer, B. M., Fuhrman, D. R., Jacobsen, N. G., & Fredsoe, J. (2015). Numerical investigation of flow and scour around a vertical circular cylinder. *Philos Trans A Math Phys Eng Sci*, *373*(2033).

Bloor, M. S. (1964). The transition to turbulence in the wake of a circular cylinder. *Journal of Fluid Mechanics*, *19*(2), 290-304.

Bombar, G. (2016). The Hysteresis and Shear Velocity in Unsteady Flows. *Journal of Applied Fluid Mechanics*, *9*(2), 839-853.

Chang, W.-Y., Lai, J.-S., & Yen, C.-L. (2004). Evolution of scour depth at circular bridge piers. *Journal of Hydraulic Engineering*, *130*(9), 905-913.

Chaudhry, M. H. (2007). *Open-channel flow*. Springer Science & Business Media.

Dargahi, B. (1989). The turbulent flow field around a circular cylinder. *Experiments in Fluids*, *8*(1), 1-12.

Fredsoe, J., & Sumer, B. M. (2002). *The mechanics of scour in the marine environment* (Vol. 17). World Scientific Publishing Company.

Gargari, M. K., Kirca, V. O., & Yagci, O. (2021). Experimental investigation of gradually-varied unsteady flow passed a circular pile. *Coastal Engineering*, 103926.

Gazi, A. H., & Afzal, M. S. (2020). A review on hydrodynamics of horseshoe vortex at a vertical cylinder mounted on a flat bed and its implication to scour at a cylinder. *Acta Geophysica*, *68*(3), 861-875.

Ghorbani, B. (2008). A field study of scour at bridge piers in flood plain rivers. *Turkish Journal of Engineering and Environmental Sciences*, *32*(4), 189-199.

Goring, D. G., & Nikora, V. I. (2002). Despiking acoustic Doppler velocimeter data. *Journal of Hydraulic Engineering*, *128*(1), 117-126.

Graf, W., & Istiarto, I. (2002). Flow pattern in the scour hole around a cylinder. *Journal of Hydraulic Research*, *40*(1), 13-20.

Graf, W., & Song, T.-C. (1995). Bed-shear stress in non-uniform and unsteady open-channel flows. *Journal of Hydraulic Research*, *33*(5), 699-704.

Guan, D., Chiew, Y.-M., Wei, M., & Hsieh, S.-C. (2019). Characterization of horseshoe vortex in a developing scour hole at a cylindrical bridge pier. *International Journal of Sediment Research*, *34*(2), 118-124.

Honji, H., & Taneda, S. (1969). Unsteady flow past a circular cylinder. *Journal of the physical society of Japan*, *27*(6), 1668-1677.

Islam, T., Rakibul Hassan, S. M., & Ali, M. (2013). Flow Separation Phenomena for Steady Flow over a Circular Cylinder at Low Reynolds Number. *International Journal of Automotive and Mechanical Engineering*, *8*, 1406-1415.

Jensen, B., Sumer, B., & Fredsøe, J. (1989). Turbulent oscillatory boundary layers at high Reynolds numbers. *Journal of Fluid Mechanics*, *206*, 265-297.

Kim, M.-S., & Sengupta, A. (2005). Unsteady viscous flow over elliptic cylinders at various thickness with different Reynolds numbers. *Journal of mechanical science and technology*, *19*(3), 877-886.

Kirkil, G., Constantinescu, S., & Ettema, R. (2005). The horseshoe vortex system around a circular bridge pier on a flat bed. XXXIst International Association Hydraulic Research Congress, Seoul, Korea,

Kitsikoudis, V., Kirca, V. S. O., Yagci, O., & Celik, M. F. (2017). Clear-water scour and flow field alteration around an inclined pile. *Coastal Engineering*, *129*, 59-73.

Kouchakzadeh, S., & Townsend, R. (1997). Maximum scour depth at bridge abutments terminating in the floodplain zone. *Canadian Journal of Civil Engineering*, *24*(6), 996.

Kumar, V., Singh, M., Thangadurai, M., & Chatterjee, P. K. (2018). Effect of Free Stream Turbulence on Flow Past a Circular Cylinder at Low Reynolds Numbers. *Journal of The Institution of Engineers (India): Series C*, *100*(1), 43-58.

Kw An, R. T., & Melville, B. W. (1994). Local scour and flow measurements at bridge abutments. *Journal of Hydraulic Research*, *32*(5), 661-673.

Lai, J.-S., Chang, W.-Y., & Yen, C.-L. (2009). Maximum local scour depth at bridge piers under unsteady flow. *Journal of Hydraulic Engineering*, *135*(7), 609-614.

Larsen, B. E., Fuhrman, D. R., Baykal, C., & Sumer, B. M. (2017). Tsunami-induced scour around monopile foundations. *Coastal Engineering*, *129*, 36-49.

Melville, B. W., & Coleman, S. E. (2000). *Bridge scour*. Water Resources Publication.

Mohamed, Y. A., Nasr-Allah, T. H., Abdel-Aal, G. M., & Awad, A. S. (2015). Investigating the effect of curved shape of bridge abutment provided with collar on local scour, experimentally and numerically. *Ain Shams Engineering Journal*, *6*(2), 403-411.

Monin, A. S., & ÎAglom, A. (1971). *Statistical fluid mechanics: mechanics of turbulence* (Vol. 2).

Mori, N., Suzuki, T., & Kakuno, S. (2007). Noise of acoustic Doppler velocimeter data in bubbly flows. *Journal of engineering mechanics*, *133*(1), 122-125.

Mrokowska, M. M., Rowiński, P. M., & Kalinowska, M. B. (2015). Evaluation of friction velocity in unsteady flow experiments. *Journal of Hydraulic Research*, *53*(5), 659-669.

Nezu, I., Kadota, A., & Nakagawa, H. (1997). Turbulent structure in unsteady depth-varying open-channel flows. *Journal of Hydraulic Engineering*, *123*(9), 752-763.

Nezu, I., & Nakagawa, H. (1995). Turbulence measurements in unsteady free-surface flows. *Flow measurement and instrumentation*, *6*(1), 49-59.

Nicolle, A., & Eames, I. (2011). Numerical study of flow through and around a circular array of cylinders. *Journal of Fluid Mechanics*, *679*, 1-31.

Oliveto, G., & Hager, W. H. (2005). Further Results to Time-Dependent Local Scour at Bridge Elements. *Journal of Hydraulic Engineering*, *131*(2), 97-105.

Qu, Z. (2002). Unsteady open-channel flow over a mobile bed. *Ecole Polytechnique Federale de Lausanne, Lausanne, Switzerland*.

Rahman, M. M., Karim, M. M., & Alim, M. A. (2007). Numerical investigation of unsteady flow past a circular cylinder using 2-D finite volume method. *Journal of Naval Architecture and Marine Engineering*, *4*(1), 27-42.

Rao, S. K., Sumner, D., & Balachandar, R. (2004). A visualization study of fluid-structure interaction between a circular cylinder and a channel bed. *Journal of Visualization*, *7*(3), 187-199.

Rasooliyanfar, P., & Afzalimehr, H. (2007). The effect of components of turbulent flow on incipient motion of sediment. the Seventh International Seminar on River Engineering. Khuzestan Water and Power Authority, Shahid Chamran University of Ahvaz, Ahvaz (In Persian),

Roshko, A. (1961). Experiments on the flow past a circular cylinder at very high Reynolds number. *Journal of Fluid Mechanics*, *10*(3), 345-356.

Roulund, A., Sumer, B. M., FredsØE, J., & Michelsen, J. (2005). Numerical and experimental investigation of flow and scour around a circular pile. *Journal of Fluid Mechanics*, *534*, 351-401.

Savitzky, A., & Golay, M. J. (1964). Smoothing and differentiation of data by simplified least squares procedures. *Analytical chemistry*, *36*(8), 1627-1639.

Schafer, R. W. (2011). What is a Savitzky-Golay filter?[lecture notes]. *IEEE Signal processing magazine*, *28*(4), 111-117.

Schewe, G. (1983). On the force fluctuations acting on a circular cylinder in crossflow from subcritical up to transcritical Reynolds numbers. *Journal of Fluid Mechanics*, *133*, 265-285.

Smith, D. (1976). Bridge failures. *Proceedings of the institution of civil engineers*, *60*(3), 367-382.

Song, T.-c., & Graf, W. (1996). Velocity and turbulence distribution in unsteady open-channel flows. *Journal of Hydraulic Engineering*, *122*(3), 141-154.

Stevens, M. A., Gasser, M. M., & Saad, M. B. (1991). Wake vortex scour at bridge piers. *Journal of Hydraulic Engineering*, *117*(7), 891-904.

Stringer, R. M., Zang, J., & Hillis, A. J. (2014). Unsteady RANS computations of flow around a circular cylinder for a wide range of Reynolds numbers. *Ocean Engineering*, *87*, 1-9.

Sumer, B. M. (2006). *Hydrodynamics around cylindrical strucures* (Vol. 26). World scientific.

Sumer, B. M. (2014). Flow–structure–seabed interactions in coastal and marine environments. *Journal of Hydraulic Research*, *52*(1), 1-13.

Sumer, B. M., Christiansen, N., & Fredsøe, J. (1997). The horseshoe vortex and vortex shedding around a vertical wall-mounted cylinder exposed to waves. *Journal of Fluid Mechanics*, *332*, 41-70.

Sumer, B. M., Fredsøe, J., & Christiansen, N. (1992). Scour around vertical pile in waves. *Journal of Waterway, Port, Coastal, and Ocean Engineering*, *118*(1), 15-31.

Sumer, B. M., Jensen, P. M., Sørensen, L. B., Fredsøe, J., Liu, P. L.-F., & Carstensen, S. (2010). Coherent structures in wave boundary layers. Part 2. Solitary motion. *Journal of Fluid Mechanics*, *646*, 207-231.

Tafarojnoruz, A., Gaudio, R., & Calomino, F. (2012). Bridge pier scour mitigation under steady and unsteady flow conditions. *Acta Geophysica*, *60*(4), 1076-1097.

Unger, J., & Hager, W. H. (2006). Down-flow and horseshoe vortex characteristics of sediment embedded bridge piers. *Experiments in Fluids*, *42*(1), 1-19.

Wahl, T. L. (2003). Discussion of "Despiking acoustic doppler velocimeter data" by Derek G. Goring and Vladimir I. Nikora. *Journal of Hydraulic Engineering*, *129*(6), 484-487.

Wardhana, K., & Hadipriono, F. C. (2003). Analysis of recent bridge failures in the United States. *Journal of performance of constructed facilities*, *17*(3), 144-150.

Wei, Z., Dalrymple, R. A., Hérault, A., Bilotta, G., Rustico, E., & Yeh, H. (2015). SPH modeling of dynamic impact of tsunami bore on bridge piers. *Coastal Engineering*, *104*, 26-42.

Whitehouse, R. (1998). *Scour at marine structures: A manual for practical applications*. Thomas Telford.

Whitehouse, R. J., Harris, J. M., Sutherland, J., & Rees, J. (2011). The nature of scour development and scour protection at offshore windfarm foundations. *Marine Pollution Bulletin*, *62*(1), 73-88.

Williams, J. J., Bell, P. S., & Thorne, P. D. (2003). Field measurements of flow fields and sediment transport above mobile bed forms. *Journal of Geophysical Research: Oceans*, *108*(C4).

Williamson, C. (1989). *Oblique and parallel modes of vortex shedding in the wake of a circular cylinder at low Reynolds numbers*.

Wu, W. (2004). Depth-Averaged Two-Dimensional Numerical Modeling of Unsteady Flow and Nonuniform Sediment Transport in Open Channels. *Journal of Hydraulic Engineering*, *130*(10), 1013-1024.

Wu, W., Vieira, D. A., & Wang, S. S. (2004). One-dimensional numerical model for nonuniform sediment transport under unsteady flows in channel networks. *Journal of Hydraulic Engineering*, *130*(9), 914-923.

Yagci, O., Yildirim, I., Celik, M. F., Kitsikoudis, V., Duran, Z., & Kirca, V. S. O. (2017). Clear water scour around a finite array of cylinders. *Applied Ocean Research*, *68*, 114-129.

Zhao, M., Cheng, L., & Zhou, T. (2009). Direct numerical simulation of three-dimensional flow past a yawed circular cylinder of infinite length. *Journal of Fluids and Structures*, *25*(5), 831-847.

APPENDICES

APPENDIX A : Flow and turbulence results for unsteady U2 flow case, in circular pile

APPENDIX B : Flow and turbulence results for unsteady U2 flow case, in elongated pile (L=2D)

APPENDIX C : Flow and turbulence results for unsteady U2 flow case, in elongated pile (L=3D)

APPENDIX D : Flow and turbulence results for unsteady U2 flow case, in elongated pile (L=4D)

APPENDIX A:

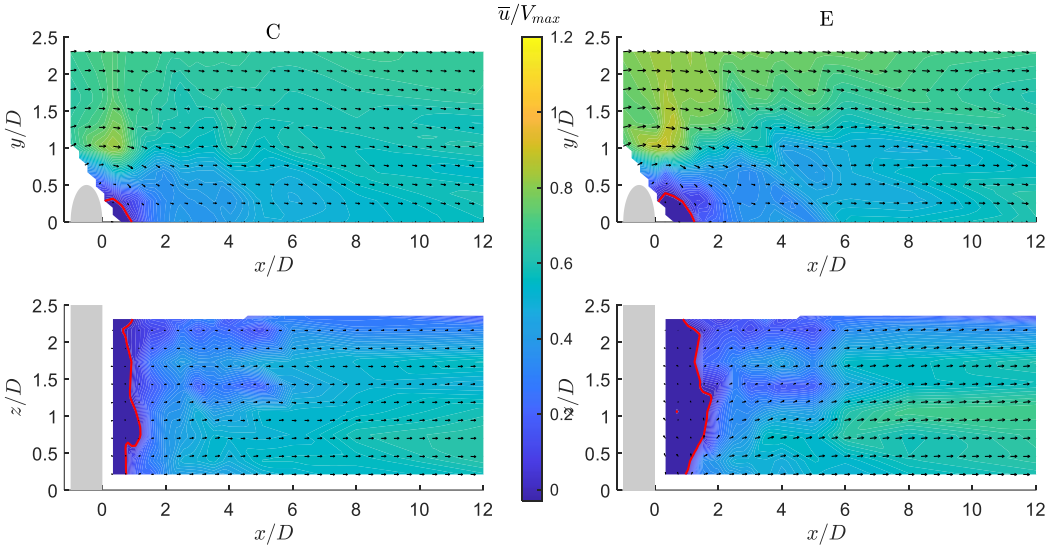

Figure A.1 : Contour plot of $\bar{u}/V_{max}$ in unsteady flow case U2 over the horizontal and vertical planes. Left pane: the time labeled C. Right pane: the time labeled E. Grey area is the pile, and the red contour marks $\bar{u} = 0$.

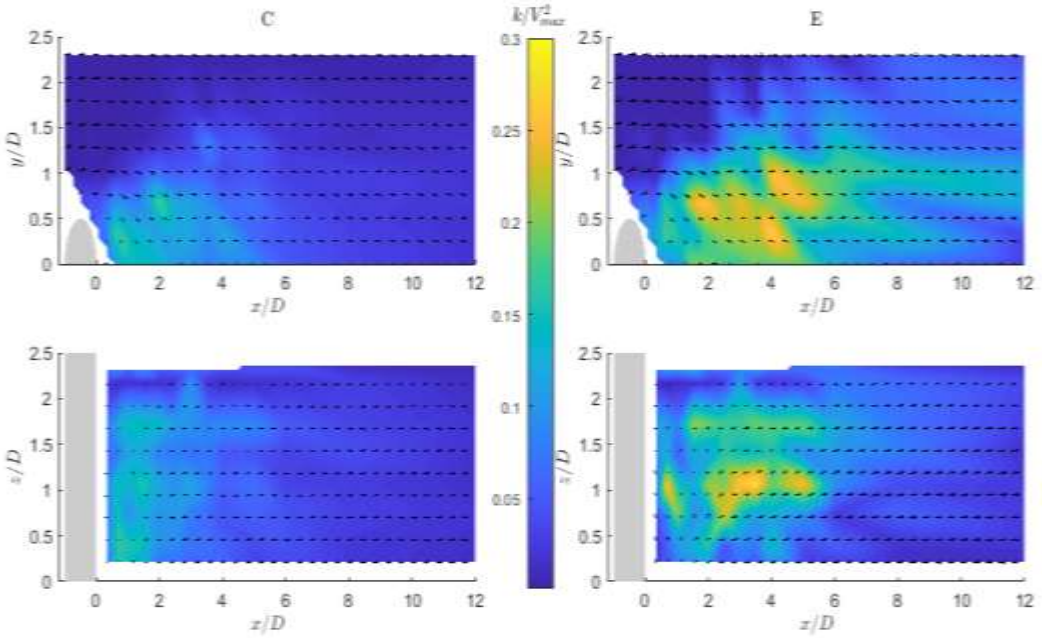

Figure A.2 : Contour plot and variations of k/V_{max} circular pile for unsteady U2 flow case.

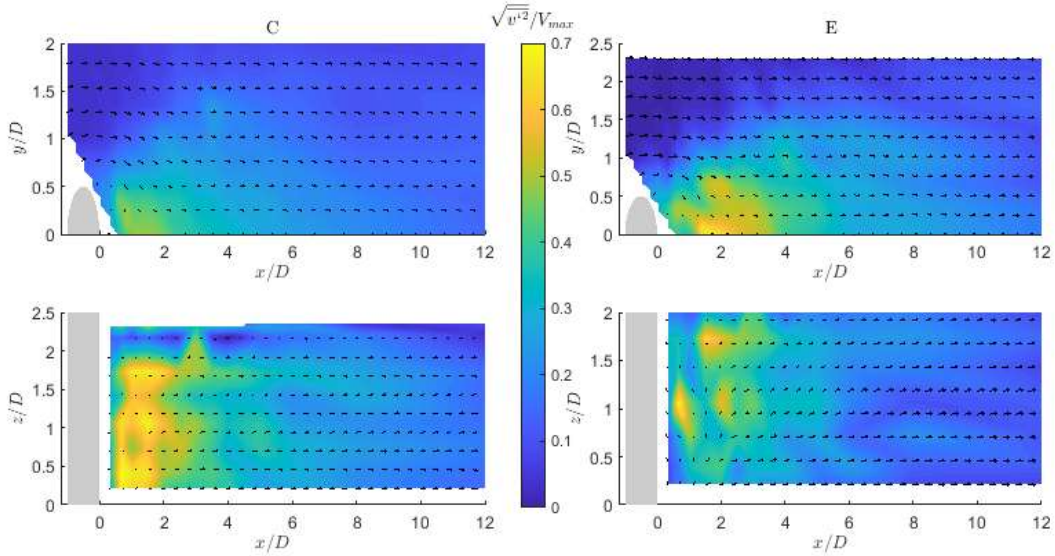

Figure A.3 : Contour plot and variations of $\sqrt{\overline{v'^2}}/V_{max}$ in circular pile for unsteady U2 flow case.

APPENDIX B:

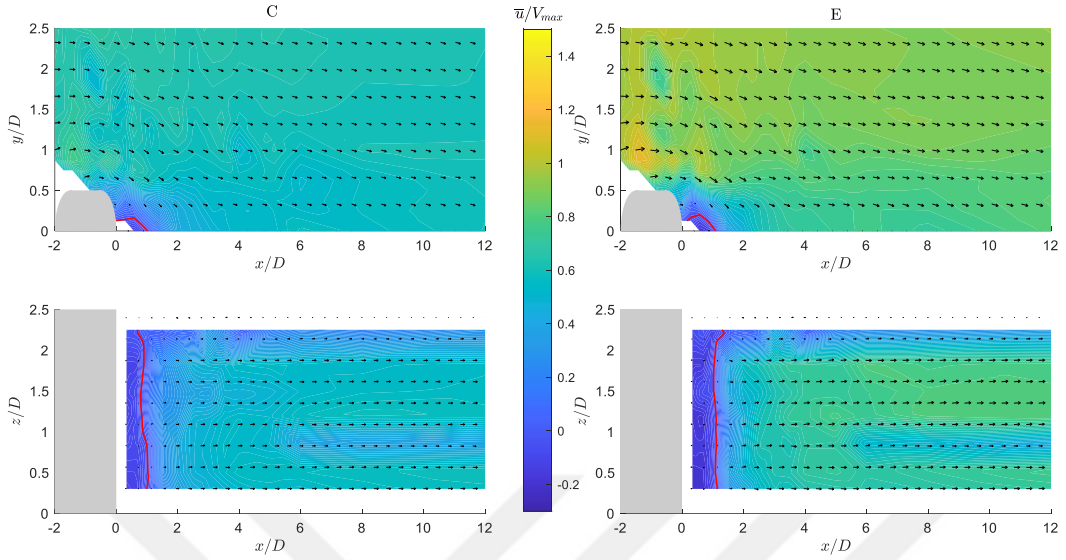

Figure B.1 : Reynolds-averaged velocity vectors, and contour plot of $\bar{u}/V_{max}$ in elongated pile (L=2D) for unsteady U2 flow case, The red contour marks $\bar{u} = 0$.

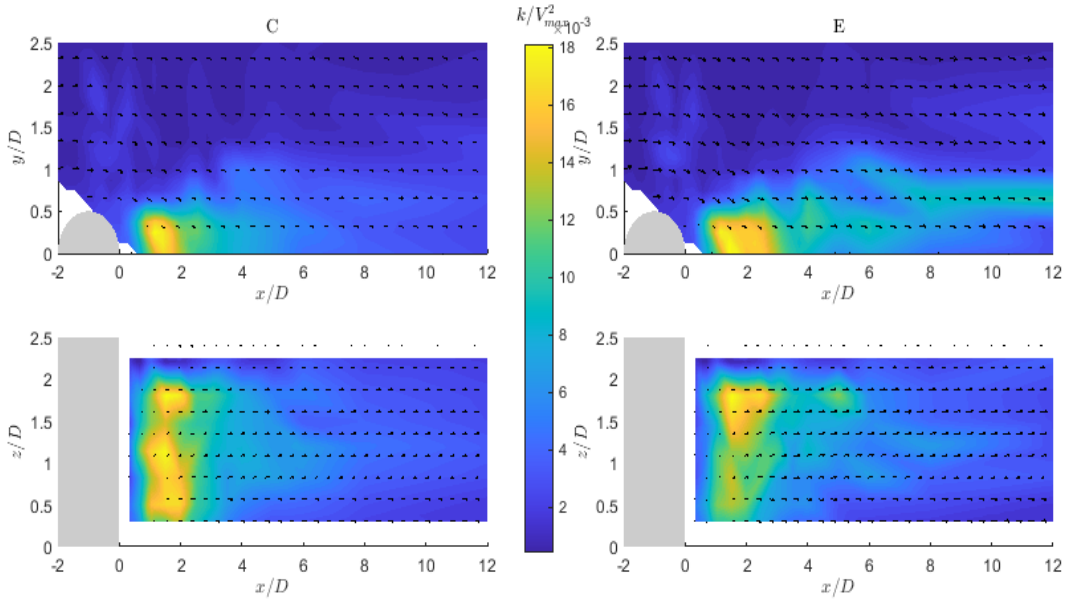

Figure B.2 : Contour plot and variations of k/V_{max} in elongated pile ($L = 2D$) for unsteady U2 flow case.

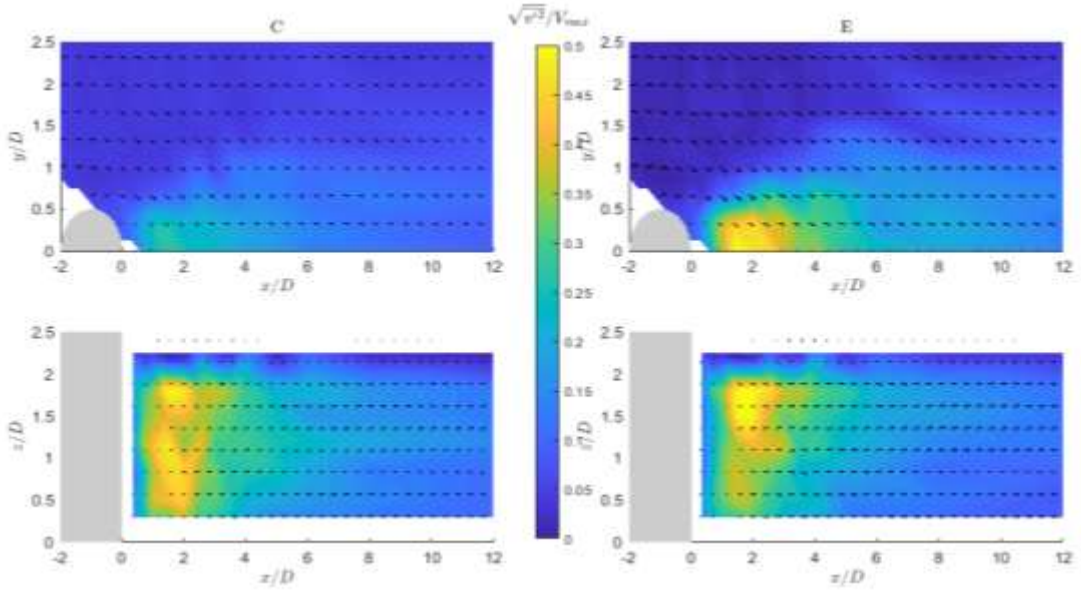

Figure B.3 : Contour plot and variations of $\sqrt{\overline{v'^2}}/V_{max}$ in elongated pile ($L = 2D$) for unsteady U2 flow case.

APPENDIX C:

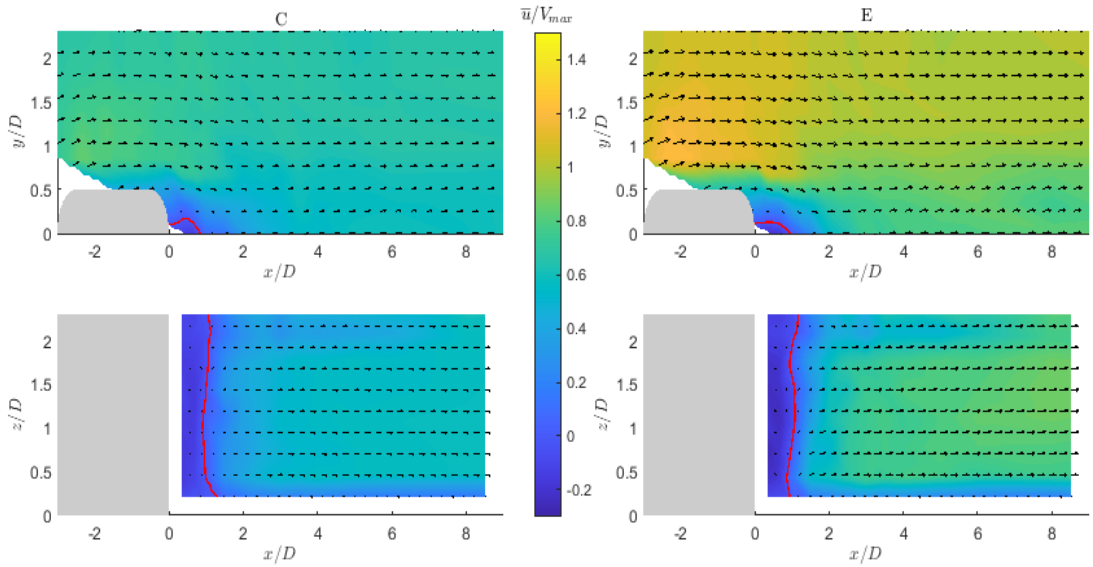

Figure C.1 : Reynolds-averaged velocity vectors, and contour plot of $\bar{u}/V_{max}$ in elongated pile (L=3D) for unsteady U2 flow case, The red contour marks $\bar{u} = 0$.

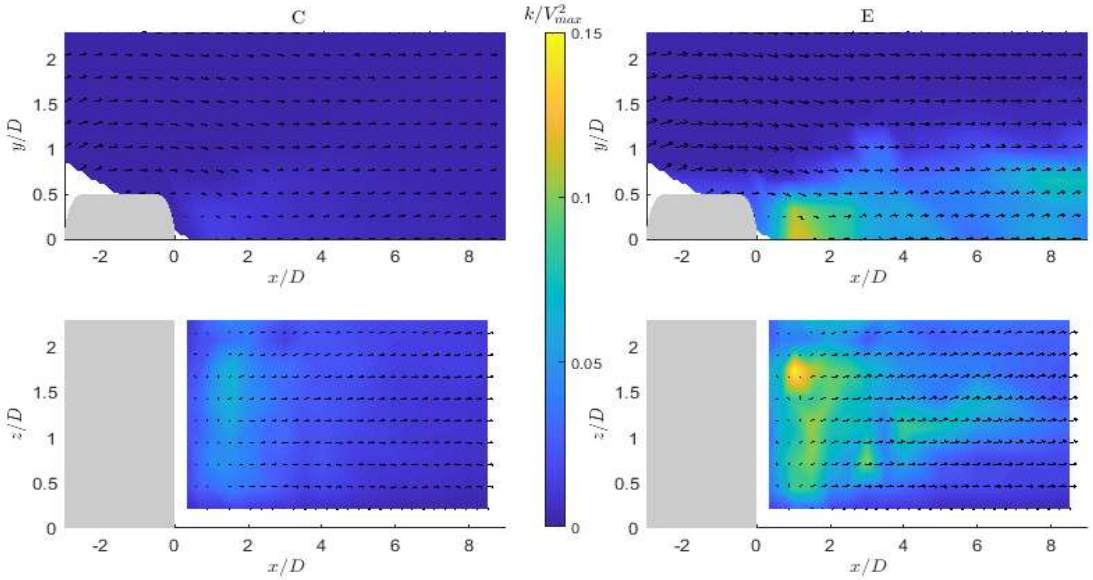

Figure C.2 : Contour plot and variations of k/V_{max} in elongated pile ($L = 3D$) for unsteady U2 flow case.

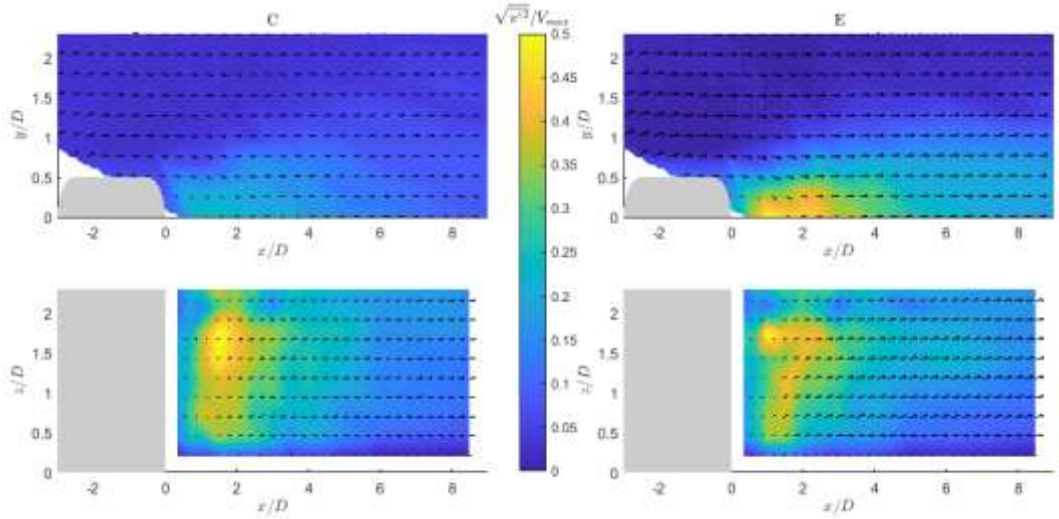

Figure C.3 : Contour plot and variations of $\sqrt{\overline{v'^2}}/V_{max}$ in elongated pile ($L = 3D$) for unsteady U2 flow case.

APPENDIX D:

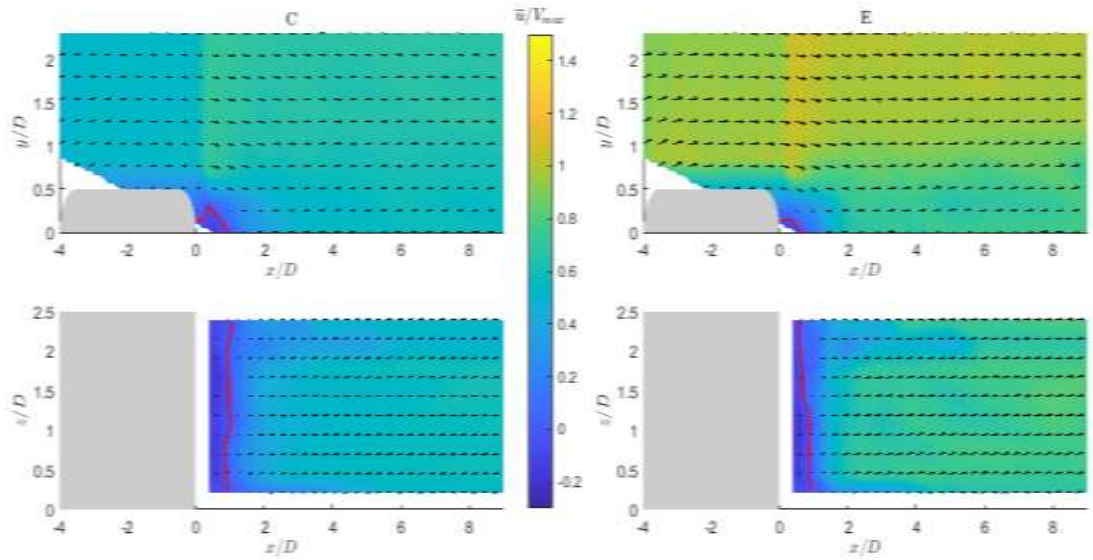

Figure D.1 : Reynolds-averaged velocity vectors, and contour plot of $\bar{u}/V_{max}$ in elongated pile (L=4D) for unsteady U2 flow case, The red contour marks $\bar{u} = 0$

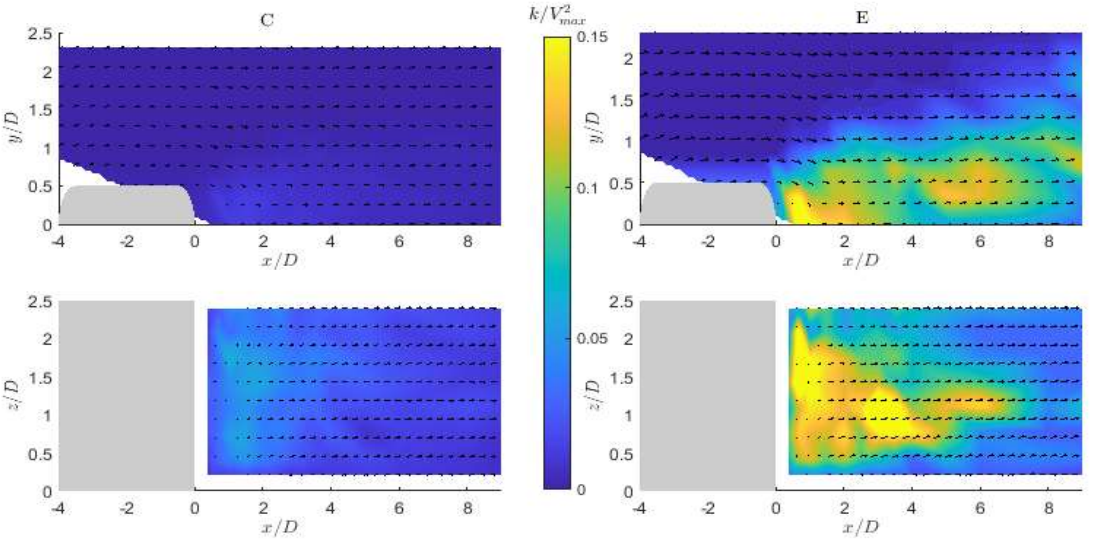

Figure D.2 : Contour plot and variations of k/V_{max} in elongated pile ($L = 4D$) for unsteady U2 flow case.

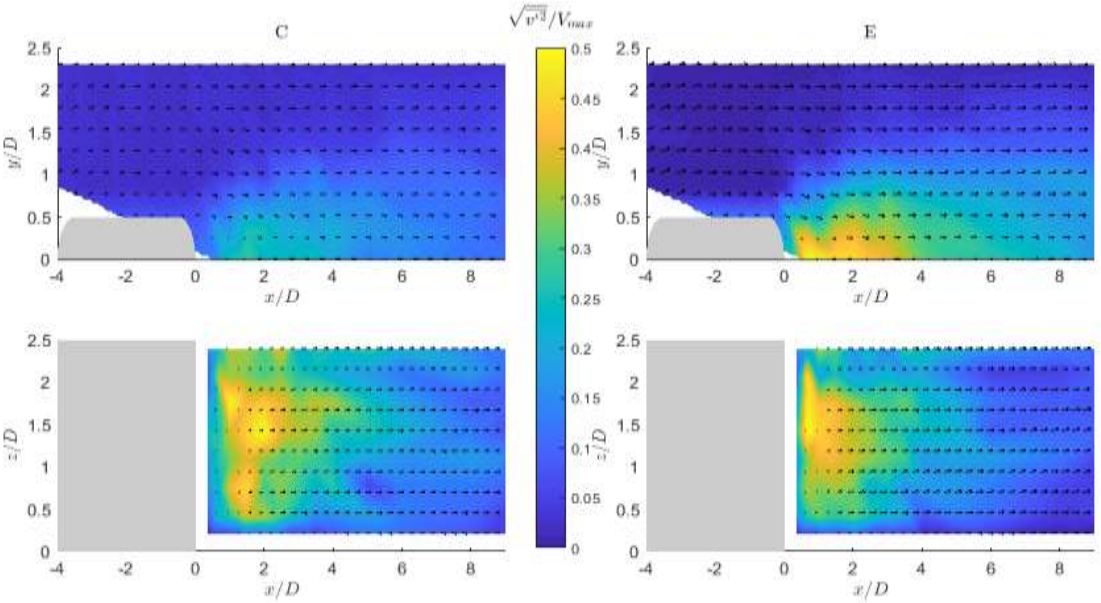

Figure D.3 : Contour plot and variations of $\sqrt{v'^2}/V_{max}$ in elongated pile ($L = 3D$) for unsteady U2 flow case.

CURRICULUM VITAE

Name Surname **:** Mehrnoush Kohandel Gargari

EDUCATION **:**

- **B.Sc.** **:** 2009, Tabriz University, Agricultural Faculty, Water Enginering Departmnt
- **M.Sc.** **:** 2013, Urmia University, Agricultural Faculty, Hydraulic Structures Engineering Departmnt

PUBLICATIONS, PRESENTATIONS AND PATENTS ON THE THESIS:

- **Kohandel Gargari, M.** , Kirca, V. S. O., & Yagci, O. (2021). Experimental investigation of gradually-varied unsteady flow passed a circular pile. *Coastal Engineering*,168, 103926.
- V. Ş. Ö. Kırca, **M. Kohandel Gargari,** U. Dolaman & O. Yağcı (2019). Değişken Akım Hidrografı Altında Dairesel Kesitli Bir Köprü Ayağı Etrafındaki Akımın İncelenmesi, 10. Ulusal Hidroloji Kongresi, Muğla, Ekim 2019.
- **M. Kohandel Gargari,** V. Ş. Ö. Kırca, U. Dolaman & O. Yağcı (2019). Effect of Unsteadiness on the Flow around a Circular Pile. *Coastal Structures, 2019*, Braunschweig, 30 Sept.-2 Oct., 2019